A MULTISCALE COMPUTATIONAL FRAMEWORK TO PREDICT DEFORMATION AND FAILURE IN POLYMER MATRIX COMPOSITES

by
Amin Aramoon

A dissertation submitted to Johns Hopkins University in conformity with the requirements for the degree of Doctor of Philosophy

Baltimore, MD
Oct 2016

Abstract

Composite materials are made by combining different materials with distinct properties to create a more unique and superior material. Nowadays, composites such as polymer matrix composites (PMCs) are extensively used in aerospace applications due to their excellent thermal stability, high strength, and light weight. Perhaps, the greatest advantage of using composite materials over metals is the ability to tailor the properties of the material by properly choosing the resin, and reinforcement materials. Epoxy polymers are often used as the matrix of advanced PMCs. The failure in PMCs occur mainly in the matrix. Therefore, manipulating the properties of PMCs requires a deep understanding of properties of the matrix. However, despite the excellent service record of PMCs, especially in aerospace applications, in many cases there remains a considerable lack of basic understanding of the microstructure and mechanisms that control their properties. Thus, there is a strong need to develop a better understanding of the role of the microstructure and the dominant deformation mechanisms to improve upon the properties of PMCs for more advanced applications.

In this thesis, a coarse-grained molecular dynamics model for modeling a highly cross-linked bisphenol a diglycidyl ether (DGEBA) system are developed to study the effects of microstructural variations on the behavior of PMCs. First, a coarse-grained molecular dynamics model is developed to simulate the thermomechanical properties of large scale epoxy systems. The interactions between particles in the coarse-grained structure are formulated by the inversion of the Boltzmann distribu-

tion of the coordinates associated with each interaction. The Boltzmann distributions are calculated from a large set of random walk simulations of the conformation of the atomic structure of the polymers using quantum mechanics simulations. In addition, a new algorithm is developed for simulating the curing process of highly cross-linked polymers. This algorithm is used to created a uniformly cross-linked epoxy system with a very high degree of cross-linkings not attainable by other algorithms in the literature. These new algorithms are available for public use as an open-source code for LAMMPS. Furthermore, a new algorithm is developed to characterize the free-volume hole distributions inside the network of epoxies. A free-volume hole is defined here as the volume between polymer chains in the network of the system. The distributions calculated from coarse-grained simulations are compared with the free-volume distribution measured from positron annihilation lifetime spectroscopy (PALS) at different temperatures, pressures, and during deformation. The predicted free-volume holes are in excellent agreement with those measured experimentally. The algorithms developed here are publicly available as an open-source software.

To investigate the effect of structural features on predicted properties of epoxy systems, several cross-linked epoxy systems are created by varying the length of cross-linking, and the degree of cross-linking of the system. It is shown that there are strong correlations between the free-volume hole average radius size and the strength and glass transition temperature of these epoxies. Based on these simulations, a new model is developed to predict the glass transition temperature of a polymeric system based on the experimentally or computational measured initial distribution of free-volume holes.

Finally, to investigate the effect of structural variation of the matrix on strength and damage evolution of PMCs, a highly cross-linked epoxy is created in the presence of two fibers. The free-volume hole distribution along the direction normal to the fibers shows a variation of matrix structure as a function of distance from the

fibers. A multi-scale finite element model has been developed to better investigate the effects of localized matrix properties on the PMCs.

Thesis Readers: Prof. Jaafar A. El-Awady (advisor), Prof. Thao D. Nguyen and Prof. Mark O. Robbins

Acknowledgements

This work was funded by grant No. FA9550-12-1-0445 to the Center of Excellence on Integrated Materials Modeling (CEIMM) at Johns Hopkins University (partners; JHU, UIUC, UCSB). The grant was awarded by the AFOSR (Program Officer, Dr. Ali Sayir) and AFRL/RX (Monitors, Dr. Christopher Woodward and Dr. Craig Przybyla).

Also I would like to acknowledge the help and support I received from several people, without which this dissertation would not have been possible. First, I would like to express my sincere gratitude to my advisor, Professor Jaafar El-Awady, for offering me guidance, keeping me motivated, helping shape my research skills, offering honest advice whenever I needed it during the times of confusion, and dealing with my way too often mistakes over the past four years, more as a friend rather than a boss. I would also like to thank Professor Mark Robbins and Prof. Vicky Thao Nguyen for reading my thesis and serving on my thesis committee.

For this work, I collaborated closely with scientists from the Air Force Research Lab. Through the long discussions I had with them I learned a lot, and they gave me a deeper appreciation of the value of my work. I would like to acknowledge specifically the help from Dr. Christopher Woodward, Dr. Tim Breitzmann, and especially Dr. Stephen Barr who helped me with my DFT simulations.

The Johns Hopkins community has provided a stimulating environment for learning and growing. I learned a lot through the interactions with many faculty members,

postdoctoral fellows and graduate students. I would also like to thank the Mechanical Engineering Department administrative staff members for their prompt and professional assistance whenever I needed it.

I would like to thank all my lab mates for the interesting discussions, necessary distractions, especially Steve Levenstein for help in editing some of the figures in this dissertation. I would also like to acknowledge the help from my dear friend Dr. Sina Moallemi who helped me in the time of need with some of my FEM simulations. During my stay in Baltimore, I was lucky to get to know a number of friends who made my life richer and much more enjoyable. I am grateful for all the great times spent with Ahmad Shahba, Ahmed Hussein, Ismail Hameddudin, Parastou Eslami, Ana Maria Carmo, Ines Godet, Aditi Gupta and Abhiram Satyadev. I am particularly grateful for the friendship of my dearest friends David H. Belton, Ololade Ajilore, Alyssa Perkinson, and Tania Perestrelo.

I cannot put into words the endless support of my family and how it brought me to where I am now. Dad, thanks for being the greatest support that one could imagine in all the past years. Mom, thanks for your love, care and tolerating my long leave. I could not have gotten through the ups and downs of this road if not for the sincerity of your prayers. Ehsan thanks for being the best companions in life, for your physical presence and mental support at the times of need. Omid, thanks for taking care of mom and dad, physically and emotionally, during my absence.

Contents

List of Tables

List of Figures

Chapter 1

Introduction

Composite materials are made by combining different materials with distinct properties to create a more unique and superior material. The history of composites starts from ancient times where straws and mud were used to make bricks for construction applications. The mud acts as a binder, which holds the integrity of the material, while straws give it strength [7]. In modern days, composite materials, such as polymer matrix composites (PMCs) and ceramic matrix composites (CMCs), have a wide variety of applications and are replacing conventional materials in a wide range of industrial applications, due to their unique properties such as high strength, low weight, and fatigue endurance. Perhaps, the most important advantage of using composite materials is the ability to tailor the properties of the material by properly choosing the resin and reinforcement materials.

1.1 Polymer Matrix Composites

Polymer matrix composites are comprised of a variety of short or continuous fibers bound together by an organic polymer matrix. In PMCs, the primary purpose for reinforcement is to improve strength, and stiffness of the material, unlike CMCs where the reinforcement is used primarily to improve the fracture toughness. A PMC

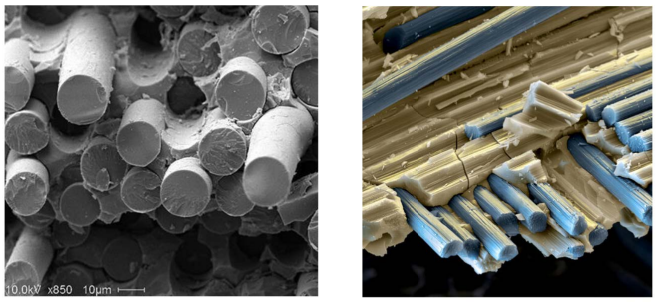

Figure 1.1: SEM micrograph of (a) CMC [1], (b) PMC [2].

is designed such that the load that the material is subjected to is supported by the reinforcement. The matrix in PMCs function as a binder between fibers and holds the integrity of the material while transferring load from matrix to the fibers [8]. Examples of scanning electron microscopy (SEM) micrographs of the matrix and fibers of a representative CMC and PMC are shown in Figure 1.1

Often, PMCs are classified into two categories: reinforced plastics, and advanced composites. The distinction is usually a function of the level of strength and stiffness; however, there is no clear line separating the two. Reinforced plastics are relatively inexpensive materials used in applications in which high strength is not required. On the other hand, expensive advanced composites have been used for only a couple of decades primarily in the aerospace industry due to their light weight, excellent thermal stability, and high strength [8–10].

1.2 Application of Polymer Matrix Composites

Several examples of applicators of PMCs are shown in Figure 1.2. Today, aerospace-related applications cover upto half the market share of advanced composites. These composites are used extensively in small military aircrafts, military and commercial rotorcrafts, and prototype business aircrafts. The next major aircraft market oppor-

tunity for advanced composites is in large military and commercial transport aircrafts [8, 11]. The primary resin materials used in aerospace applications are epoxies, such as bisphenol a diglycidyl ether (DGEBA), and the most common reinforcements are carbon nanotubes (CNT) and high-stiffness glass fibers [8]. Another 25 percent of the market share of advanced composites with an estimated annual growth rate of 3 percent is the sporting goods industry, such as in golf clubs and tennis rackets. The remaining share of the market for PMCs is covered by automotive applications and industrial equipment [8].

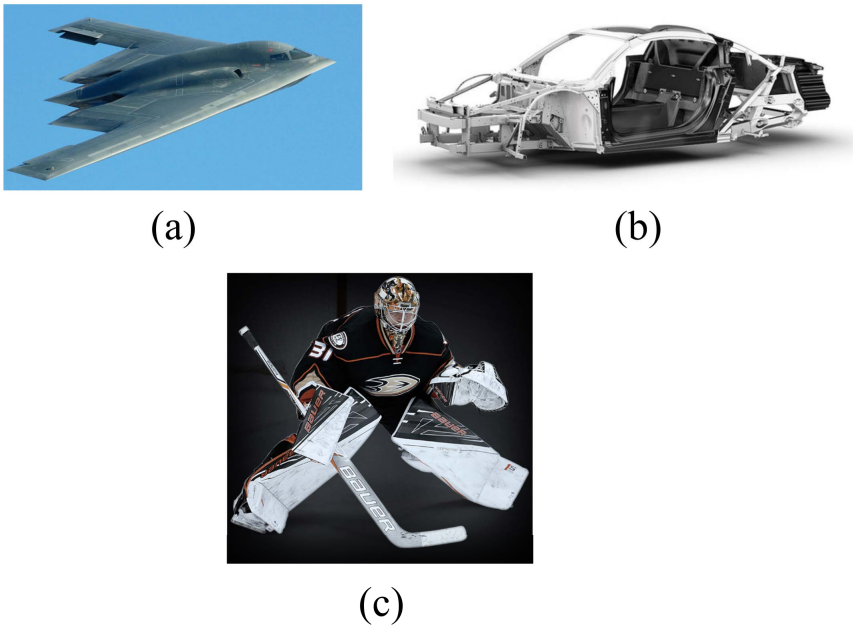

Figure 1.2: Application of PMCs in (a) aerospace [2] , (b) automotive [3], and (c) sporting goods materials [4].

Despite the excellent service record and reliability of PMCs, especially in aerospace applications, there remains a considerable lack of basic understanding of the microstrucutre and mechanisms that control their properties. As such, developing a better understanding is needed to improve upon the properties of PMCs for more advanced applications. Fundamental studies focused on the properties and controlling

mechanisms of PMCs can be categorized into three main thrusts:

- **Processing and Curing Science**: focusing on fabricating low-cost composites, and resins having uniform and advanced properties.
- **Interphase Property**: focusing on the poorly understood interfacial region between the fiber and matrix, which can critically influence the PMC behavior.
- **Impact Resistant**: which is crucial for the reliability of PMCs, especially those used in military grade structures.

1.3 Properties of Polymer Matrix Composites

The properties of PMCs are strongly correlated to their individual constituents. These constituents can be characterized as follows:

• **Reinforcement:** The high strength and stiffness of advanced composites can be attributed primarily to the continuous reinforcing fibers. The most important and commonly used fibers are carbon nanotubes and high-strength glass. PMCs contain about 60 % percent fiber by volume fraction [8]. This high volume fraction of fibers indicates the important role they play in controlling the stiffness of PMCs.

• **Matrix:** Given that the matrix is typically the weakest-link in the PMC structure, its properties determine the failure of the PMC as most of the mechanical damage that eventually leads to failure of the structure initiates in the matrix.

The matrix phase of PMCs is commonly classified as either being thermoset or thermoplastic. Thermoplastic resins, such as polyesters, poly-etherimide, and polyphenylene sulfide are polymer networks with an amorphous, semicrystalline, or crystalline structure that is formed by cooling a heated melt of long, discrete chains [9]. This process, unlike the curing process of epoxies, is reversible by reheating the

system to from a thermoplastic with a different shape. However, this also indicates that thermoplastics have a low thermal stability and strength as compared to epoxies. Therefore, the primary applications of these material are in engineering PMCs, and not advanced PMCs. Thermosetting resins such as polyesters, vinylesters, epoxies, bismaleimides, and polyamides are commonly used in fiber-reinforced plastics, and as advanced composite resins [8]. Epoxies make up the largest share of resins for advanced composite materials. Epoxies have a very low initial viscosity. In these resins, prepolymers form chemical reactions with the aid of reactive agents, called curing agents, and generate a crosslinked network of chains that connects the entire matrix together in a three-dimensional stable network. This process is called curing. These materials, because of their unique network, have a very high dimensional stability, high-temperature resistance, and good resistance to solvents.

Because the matrix largely controls the durability and toughness of PMCs, the critical enhancements in these properties can be achieved by improving the properties of the matrix rather than improving the properties of the fibers. However, because of the heterogeneity of the matrix, characterization of strength and failure of these materials is very complex. This heterogeneity often causes failure modes that have no counterpart in homogeneous materials. On the other hand, due to the complexity of the structure of epoxies, it is very difficult to design a systematic way to describe the underlying mechanism associated with the unique properties of these materials. Therefore, perhaps the most significant opportunities lie in the area of molecular characterization and design to create epoxies that exhibit the desired flexibility, strength, and high-temperature stability.

The high strength and adhesion of highly cross-linked polymer networks to a solid surface are the most important properties of these materials. The plastic behavior and failure of various polymer systems under active deformation have been studied for decades with numerous experimental and modeling techniques [12–18]. The elasto-

plastic properties of polymers and epoxies are dependent on the structural features of the polymer network, such as flexibility of the epoxy resins [10], functionality of curing agents [19], average length of epoxy segments between curing agents [20], degree of cross-linking of the epoxy [21], and arrangement of polymer chains in the cross-linked network [22].

1.3.1 Material properties of epoxies

An epoxy resin denotes a low molecular weight pre-polymer, or a highly cross-linked polymer system that normally has a very high molecular weight [9]. In general, an uncured epoxy system has a poor mechanical and thermal stability. However, these systems can obtain very high thermomechanical stability by forming a three-dimensional cross-linked network by reacting the linear epoxy prepolymers with suitable curing agents in a process commonly referred to as curing or cross-linking.

Curing may be achieved by homopolymerisation when an epoxy resin reacts with another epoxy resin, or by forming a copolymer by adding curing agents or hardeners such as polyfunctional amines or acids [9]. In principle, any molecule containing a reactive hydrogen may react with the epoxide groups of the epoxy resin. Although some blends of prepolymers/curing agents will cure at ambient temperature, the curing processes of most polymer blends require a high heat, with a temperature range of 450 K to 550 K [10]. Insufficient heat during the curing process results in an incomplete polymerisation of the network that leads to a weakened mechanical chemical and heat stability [10].

One of the most important properties of any epoxy is the glass transition temperature, T_g, which is the temperature at which the polymer transitions from a hard, glassy material to a soft, rubbery one. This temperature for highly cross-linked epoxies is higher than that for their uncured counterparts. This is mostly due to the fact

that the movements of large segments of epoxies are severely restricted due to the highly cross-linked and stable 3D network of the epoxy. However, it has been shown that cross-linking does not alter the glass transition temperature if the average length of segments between curing agents in the network is longer than the length required for the rotation of chains around their backbone structure [9].

One way to measure T_g is using Differential Scanning Calorimetry (DSC), which captures the changes in the heat capacity of a sample as a step in the baseline of the recorded DSC signal [23]. This is quantified as the temperature where a kink is observed on the specific volume versus temperature curve of the system subjected to rapid cooling from a heated melt. In reality, the glass transition is not a discrete thermodynamic transition, but rather a temperature range over which the mobility of the polymer chains increases significantly than a discrete thermodynamic transition. However, typically a single value for T_g is defined as the mean temperature bounded by tangent lines to the two straight regions of the high and low-temperature parts of the specific volume versus temperature curve. It should be noted that the the glass transition temperature is controlled by several factors such the chemical structure of the epoxy resin, the type of curing agents, and the degree of cross-linking of the system [9].

The high strength and adhesion of highly cross-linked polymer networks to the surface of fibers is an important property of these materials that are used extensively as resins in the advanced composites. The molecular origins of the deformation of epoxy polymers has been a subject of debate for years, and despite all the experimental and modeling advances reported in the literature [12–14], the molecular origins of these properties are not well understood.

An important aspect in characterizing properties of epoxy polymers is correlating the microstructural features of their network to the properties of the material. Various methods have been used to deduce the effects of structural properties such as the

degree of cross-linking [13, 21], curing agent functionality [19], the flexibility of polymer chains[12, 13], chain configurations [22, 24], and average length of cross-linking [19, 20, 24, 25].

One way to investigate the effects of the structural features of polymer networks on their predicted properties is characterizing free-volume holes in their microstructures. Experimental investigations of the evolution of free-volume holes with temperature and pressure have shown a very strong correlation between free-volume hole distribution and the glass transition temperature of the epoxy. On the other hand, despite a few experiments showing a good correlation between free-volume hole evolution with the stress-strain relationship of polymers during deformation, there has been a lack of investigations on studying a meaningful correlation between free-volume hole evolution with the strength and the plastic deformation of polymer systems.

1.3.2 The free-volume distribution in epoxies

Positron annihilation lifetime spectroscopy (PALS) is a sophisticated technique for characterizing the effects of the temperature, pressure, and deformation of epoxies on free-volume holes in epoxy networks. Thorough this technique it was shown that there exists a strong correlation between the evolution of free-volume holes and the thermomechanical properties of epoxies [26–28]. It should be noted that, as defined here, the free-volume holes discussed in this thesis are different then the phenomenological definition of free-volume in the free-volume theory. The PALS experiments measure a distribution of free-volume holes between the polymer chains in the system [26–29] while in the free-volume theory the definition of free-volumes was defined as the region accessible to a molecule through a drifting motion that does not require interaction with its neighbors [15, 30].

1.4 Computational Simulations of PMCs at Different Length Scales

The finite element method (FEM) has become a standard approach for simulating the behaviors of any systems subjected to thermomechanical loads [31–38]. At the heart of any FEM simulation lies the constitutive model, which is a mathematical representation of the material's behavior. The precision of FEM results is determined by the robustness of this model. On the other hand, identifying a mathematical model to mimic the physical properties of the matter accurately is an incredibly difficult task. For instance, the failure of PMCs is an intrinsically multi-scale phenomena, where the distribution of fibers, local properties of the matrix, temperature, strain rate, and the fiber-matrix interface properties dictate the mode and location of failure initiation [39, 40]. Furthermore, it should be noted that most typical constitutive models are phenomenological in nature, and they are only based on empirical fits of a mathematical model to the response that the material of interest shows under laboratory controlled conditions. While this approach in constitutive model development is suitable for simulating large-scale heterogeneous systems with multiple interacting components, it does not provide an insight into the physics of deformation or failure. Therefore, these models can be used to simulate the dynamics of complex engineering systems only for engineering design purposes, and substantial knowledge from lower length scale models is needed to develop a better understanding of the controlling mechanisms of the material properties.

At a lower length scale, coarse-grained molecular dynamics simulations provide an avenue to explore the thermomechanical response of PMCs in the range from about 20 nm to 5 µm in length and up to a few µs in time [41–43]. This range is suitable for resolving the motion and interactions of individual polymer chains as independent entities. The length scale probed by these models is suitable for modeling the

behavior of matrix around the fibers in a composite structure. The coarse-grained models are usually made by lumping different groups of atoms into coarser particles called beads. In the literature, there are a large number of coarse-grained models, and each is unique in terms of how it deals with the interaction between beads in the system [21, 41–47]. The interaction between coarse-grained beads is usually the statistical representation of the behavior of different groups of atoms that are calculated from a lower scale model. It should be noted that coarsening of a polymer system comes with the cost of losing precision in capturing the accurate conformation of the polymer chains. Therefore, if the interaction between atoms is the interest of the simulation, knowledge of a lower length scale such as all atom molecular dynamics (MD) is required.

Molecular dynamics simulations [48] can model systems ranging in size from few nanometers to hundreds of nanometers over time intervals up to a few microseconds. MD simulations are sophisticated n-body simulations that can trace the motion of every single molecule or atom in the simulation and extract useful system information such as temperature, pressure, and energy based on this data. The scale of MD simulations separates the scales where classical mechanics are valid from those that cannot be treated without resorting to quantum mechanics. One of the main assumptions made in MD simulations is ithe interaction forces between different atoms, which are defined by parametrized interatomic potentials, or force fields, in order to properly capture the atomic interactions and the system's energy. These interatomic interactions are usually developed and fit using lower scale simulation methods.

At the very bottom of the length and time scales lies the most basic, first principles, simulation method, the Density Functional Theory (DFT) [49]. DFT simulations are direct solutions to Schrodinger's equation that yield the electronic structure of matter. The Born-Oppenheimer [49] approximation is used to separate the slow motion of the heavier atomic nuclei from the faster and almost instantaneous motion of the

lighter electrons. Then, the Hohenberg-Kohn theory [50] provides the justification for approximating the electronic configuration by a spatially varying electron density. The main outcome of DFT simulations is the systems ground state and energy. DFT calculations are used to develop interatomic potentials suitable for different kinds of elements to be used in MD simulations [51]. The length scale of DFT calculations is typically that of a few atoms (i.e. a few Angstroms).

The methods briefly discussed here cover all the relevant length and time scales employed in computational mechanics of PMCs. Figure 1.3 summarizes the various length and time scales discussed above along with the appropriate simulation methods for each scale. These scales are usually connected together in a hierarchical manner where information from one scale, usually the lower scale, is used to enrich the higher length scales with the parameters they need.

In this thesis, DFT and MD simulations are coupled to develop a coarse-grained model for simulating the thermomechanical properties of highly crosslinked epoxy systems. The coarse-grained simulations are used to predict a correlation between the distribution of free-volume holes in the epoxy system and its glass transition temperature, and elastoplastic behavior. Then, the distribution of holes in these coarse-grained networks is used to bridge the coarse-grained length scale to continuum length scale simulations.

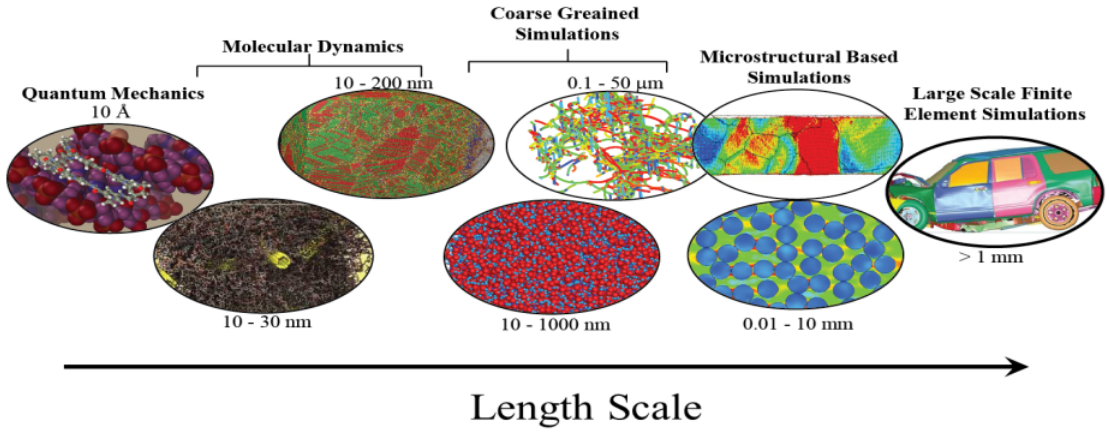

Figure 1.3: Different computational methods and their appropriate length and time scales for modeling the behavior of polymeric/metallic systems.

1.5 Thesis Objectives and Organization

The objective of this thesis is to develop an extensible coarse-grained MD model for investigating the effect of the structural variation of polymer networks on their predicted properties. In particular, the following research efforts have been undertaken:

- Development of a coarse-grained MD technique for modeling thermomechanical properties of highly crosslinked epoxy systems.
- Development of a curing algorithm for modeling the curing process of highly cross-linked epoxy systems.
- Developing a algorithm for quantifying free-volume hole distributions and their evolution in molecular systems.
- Investigating the effects of the free-volume hole distribution and the glass-transition temperature of epoxies.
- Investigating the correlation between the free-volume hole distribution on strength

of the epoxy matrix.

- Incorporating the structural variation of the matrix in PMCs as a function of distance from the fibers into a FEM model by correlating material properties to free-volume hole distributions.

The thesis is organized as follows. In Chapter 2, the development of the coarse-grained model from qunatum mechanics simulations is discussed, and the results for coarse-grained potentials at different temperatures are presented. In Chapter 3, the details of the curing algorithm are presented, and results of the curing process, as well as predictions about the dynamic properties of curing, are presented. In Chapter 4, the implementation of a new algorithm for characterizing free-volume holes from MD and coarse-grained MD simulations inside the polymer network are discussed. In Chapter 5, the effects of free-volume hole distribution on the glass transition temperature of the polymeric network are investigated. Also, the free-volume hole distributions calculated from the simulations are compared to those measured from experiments at different temperatures and pressures. In Chapter 6, the effect of free-volume holes on strength of epoxies in investigated. Then, the variation of the structural features of the resin of a PMC between two fibers are investigated, and a localized damage model is presented to account of these variations in modeling for the damage of PMCs.

Chapter 2

Coarse-Graining of Inter-Particle Interactions of Epoxy Polymers

2.1 Introduction

The industrial applications of polymers require a deep understanding of their material properties and the molecular origins of their dominant deformation mechanisms. Despite all recent experimental advances in microstructural characterization of polymeric materials, experimental investigations of the dominant molecular mechanisms still suffer from complications and difficulties associated with collecting conformation-specific data especially during deformation [21, 52, 53]. These limitations have made computer simulations a standard tool to study the connection between microscopic, chemical detail, and macroscopic properties of these materials.

One of the most commonly used methods is molecular dynamics (MD) simulations, which have been recently utilized to deduce the molecular details of the plastic flow, glassy response, pressure, and temperature dependence of polymeric systems [12, 13]. However, MD simulations typically suffer from severe limitations in the spatial and temporal scales. In MD simulations it is computationally impractical to solve the

newton equations of motion for each particle. These limitations are also more pronounced in simulations of polymeric materials, especially when comparatively large simulation cells are needed to simulate statistically independent material properties. Therefore, the trajectories of each atom are calculated by solving the equations of motion on a very short interval of time. As a result, a chemically detailed simulation of materials are limited to several tens of thousands of particles over a very short period of time. This is a very prohibitive limitation given that a larger number of particles, as well as longer times of simulations are required to successfully model phenomena such as plastic flow, temperature, and pressure dependence of polymers. In order to simulate such phenomena, the chemical details of these atomic systems, which are believed to have a negligible effect on these properties, can be eliminated from the simulations. This will lead to a substantial reduction in the number of degrees of freedom in the simulations, which will allow modeling systems having larger sizes, and to longer times. For instance, to study the behavior of a polymer chain in solution, the motion of the solvent atoms is not of primary importance, so it can be incorporated as external forces on the polymer solvent to have an effective friction and a modified polymer interaction [54, 55].

Another way to overcome these limitations is to reduce the number of degrees of freedom in the atomic simulations by mapping the atomic structure to a group of coarser particles, called "Super-Atoms" [21, 41, 42, 47, 56]. This process leads to a lower number of degrees of freedom and softer inter-particle potentials, as compared to MD potentials, which can dramatically decrease the effective cost of the simulation. One approach to coarse-graining is to use longer time steps, by freezing fast motions of atoms that are not coupled to the properties of interest, by uniting their relative motion to their neighboring atoms in the backbone of the molecule. This technique is called the method of "united atoms". However, due to its very low scale of coarse-graining, the speed up gained from this technique is comparatively lower

than other coarse-graining techniques [57–60].

Other coarse-graining approaches can be typically grouped into two techniques. In the first technique, coarse-graining is achieved by optimizing the inter-particle potentials to match certain macroscopic physical properties. Examples of this include coarse-graining the force fields by optimizing the potential fields for partitioning of free energy between polar and apolar phases of lipid and surfactant [41, 47], or optimizing them for density and surface tension of surfactant/water systems [42]. In this technique, the exact one-to-one mapping of atomic groups to super-atoms introduces a large number of parameters to be optimized. Thus, for systems with different monomers, the optimization becomes impractical. Instead, simplified potential fields are often used [21, 56], which poorly simulate the conformation of chains in the network. In the second technique, the focus is on matching the structural aspects of the material, such as centroid, mass, and angular momentum, through adjusting the mean forces derived from the Boltzmann inversion [43–46, 61, 62] or the inverse Monte Carlo methods [63]. The coarse-grained potential fields developed in this technique are only guaranteed to be accurate for simulations having identical thermodynamic conditions to those they were fitted to [21] .

It should be noted that one limiting factor in most coarse-grained simulations is that the approach does not account for the dihedral coarse-grained coordinates formed during the curing process [21, 45, 56]. However, the dihedral degrees of freedom are known to have a significant role in the conformational changes of polymer chains, especially in deformation of rubbery polymers [10].

In this chapter a brief overview of MD simulation is given. The material system chosen for all the simulations in this thesis is then introduced, and finally, a new coarse-grained model is developed for the epoxy system. In this model, all the conformationally relevant coarse-grained degrees of freedom, including angles and dihedral angles formed during the curing process, are accounted for by Boltzmann inversion

technique over all the coarse-grained coordinates via quantum mechanics (QM) simulations. The pair potential is also optimized to predict the experimentally reported density of the system at different temperatures.

2.2 Molecular Dynamics Simulation

In the following a short description of MD simulations is given for completeness. Full details of MD simulations, as well as further details about different implementation of this method can be found elsewhere [48, 64–66].

2.2.1 Degrees of freedom

The Hamiltonian of a molecular system has the following form [48]:

$$H(p^N, r^N) = K(p^N) + V(r^N) \tag{2.1}$$

where K is the kinetic energy, and V is the potential energy of a system composed of N molecules having the geometrical coordinates of r and momenta of p. The kinetic energy is described as:

$$K(p^N) = \sum_{n=1}^{N} \frac{p_i}{2m_i} = \sum_{n=1}^{N} \frac{1}{2} m v_i^2 \tag{2.2}$$

and is independent of particle coordinates in the absence of constraints on particle locations. If a constraint is imposed in geometrical coordinates of particles, the velocity in the constraint direction is zero. Here, the potential energy, V, describes the interaction energy of the system as a function of the particle coordinates. Generally, the potential energy is a function of the location of particles, and the corresponding set of interactions, s. The potential energy is the sum of all different types of interactions between particles in the system, such that:

$$V(\mathbf{r},\mathbf{s}) = V(\mathbf{r}_1, \mathbf{r}_2, ..., \mathbf{r}_N; s_1, s_2, ..., s_M) \tag{2.3}$$

Here $\mathbf{r}$ is the $3 \times N$ dimensional vector of the coordinate of atoms in the system, and M is the number of different interactions in the system. The potential energy is usually divided into non-bonded, and covalent interactions.

$$V(\mathbf{r},\mathbf{s}) = V^{cov}(\mathbf{r},\mathbf{s}) + V^{nbd}(\mathbf{r},\mathbf{s}) \tag{2.4}$$

The covalent interactions are further divided into bond stretching, angle bending, proper and improper dihedral angle torsional interactions. Also, the non-bonded potentials are composed of of van der Waals and electrostatic interactions. The force f_i applied on each particle due to all these interactions is calculated by the following relation [48]:

$$\mathbf{f}_i = \frac{\partial}{\partial \mathbf{r}_i} V(\mathbf{r}_1, \mathbf{r}_2, ..., \mathbf{r}_N, \mathbf{s}) \tag{2.5}$$

2.2.2 Covalent interactions

The covalent interaction potentials are a group of molecular potentials that involve sharing electron pairs between paired molecules. These potentials are partitioned as a sum of contributions from bond stretching, V^{bnd}, bond-angle bending, V^{ang}, improper dihedral-angle bending, V^{imp}, and proper dihedral-angle torsion, V^{dih}, interactions, such that [48]:

$$V^{cov}(\mathbf{r},\mathbf{s}) = V^{bnd}(\mathbf{r},\mathbf{s}) + V^{ang}(\mathbf{r},\mathbf{s}) + V^{dih}(\mathbf{r},\mathbf{s}) + V^{imp}(\mathbf{r},\mathbf{s}) \tag{2.6}$$

In the following, different types of covalent potential interactions are discussed.

Bond stretching force-field

The potential energy term associated with bond-stretching is formulated as follows [48]

$$V^{bnd}(\mathbf{r},\mathbf{s}) = \sum_{i=1}^{N_b} V^b(\mathbf{r},\mathbf{s},d_0^i) \tag{2.7}$$

where V^b is the bond potential energy for an individual bond in the system composed of N_b bonds, and d^i is the equilibrium length of the i^{th} bond. Two of the more common types of bonded interactions are quartic and harmonic potentials [48]. The quartic bond potential is defined as:

$$V^b_{quart}(\mathbf{r},\mathbf{s}) = \frac{1}{4}K_{bq}\left(|\mathbf{r}_j-\mathbf{r}_i|^2 - d_0^2\right)^2 \tag{2.8}$$

while the harmonic bond potential is formulated as:

$$V^b_{harm}(\mathbf{r},\mathbf{s}) = \frac{1}{2}K_{bh}\left(|\mathbf{r}_j-\mathbf{r}_i| - d_0\right)^2 \tag{2.9}$$

The forces applied on the molecules due to these interactions are the derivatives of these potentials, and are formulated as follows:

$$f^b_{quart} = -K_{bq}\left(|\mathbf{r}_j-\mathbf{r}_i|^2 - d_0^2\right)(\mathbf{r}_j-\mathbf{r}_i), \tag{2.10a}$$

$$f^b_{harm} = -K_{bh}\left(|\mathbf{r}_j-\mathbf{r}_i| - d_0\right)\frac{(\mathbf{r}_j-\mathbf{r}_i)}{|\mathbf{r}_j-\mathbf{r}_i|} \tag{2.10b}$$

Angle bending force-field

The potential energy term associated with bond angle-bending interactions is defined as follows [48]:

$$V^{ang}(\mathbf{r}, \mathbf{s}) = \sum_{i=1}^{N_a} V^a(\mathbf{r}, \mathbf{s}, \theta_0^i) \tag{2.11}$$

where V^a is the angle potential energy for an individual angle in the system composed of N_a angles, and θ_0^i is the equilibrium angle of the i^{th} angle between i^{th}, j^{th}, and k^{th} atoms in the system. Two of the more common types of angular interactions are cosine-harmonic and angle-harmonic potentials [48]. The cosine-harmonic bond angle bending potential is defined as [48]:

$$V_{cos}^a(\mathbf{r}, \mathbf{s}) = \frac{1}{2} K_{ac} \left(\cos\theta - \cos\theta_0\right)^2 \tag{2.12}$$

while the angle-harmonic bond potential is formulated as [48]:

$$V_{ang}^a(\mathbf{r}, \mathbf{s}) = \frac{1}{2} K_{aa} \left(\theta - \theta_0\right)^2 \tag{2.13}$$

The forces applied on the atoms due to these interactions are the derivatives of these potentials, and are formulated as follows:

$$f_{cos}^a = -K_{ac}[\cos\theta - \cos\theta_0](\frac{\mathbf{r_{ij}}}{r_{ij}} - \frac{\mathbf{r_{jk}}}{r_{jk}}\cos\theta), \tag{2.14a}$$

$$f_{cos}^a = -K_{aa}\frac{\theta - \theta_0}{\sin\theta}(\frac{\mathbf{r_{ij}}}{r_{ij}} - \frac{\mathbf{r_{jk}}}{r_{jk}}\cos\theta) \tag{2.14b}$$

where $\mathbf{r}_{ij} = \mathbf{r}_i - \mathbf{r}_j$ and $\mathbf{r}_{jk} = \mathbf{r}_j - \mathbf{r}_k$.

Proper dihedral-angle bending force-field

The potential energy associated with the in-plane torsion angles of the system is accounted for by a proper dihedral-angle bending potential term, which is formulated as follows [48]:

$$V^{\eta}(\mathbf{r},\mathbf{s}) = \sum_{i=1}^{N_{\eta}} V^{\eta}(\mathbf{r},\mathbf{s},\eta_0^i) \tag{2.15}$$

where $V^{\eta}(\mathbf{r},\mathbf{s},\eta_0^i)$ is the proper dihedral angle potential energy term for an individual in-plane dihedral angle between four consecutively bonded moelcules in a system composed of N_{η} dihedral angles, with the equilibrium angle of the i^{th} angle equal to η_0^i. The quantity of the dihedral angle formed by four connected atoms $i, j, k,\ l$ is defined as:

$$\eta = sign(\mathbf{r_{ij}} \,.\, (\mathbf{r_{ij}} \times \mathbf{r_{kl}})) \arccos \frac{(\mathbf{r_{ia}} \,.\, \mathbf{r_{lb}})}{r_{ia} r_{lb}} \tag{2.16}$$

where $\mathbf{r}_{ij} = \mathbf{r}_i - \mathbf{r}_j$. Knowing the magnitude of dihedral angle, the symmetric proper dihedral-angle torsion interaction is defined as [48]:

$$V^{\eta}_{sym}(\mathbf{r},\mathbf{s}) = K_{pro} \left(1 + \cos\eta^0 \times \cos\left(s\,\eta\right)\right)^2 \tag{2.17}$$

The force applied on the atoms due to these interactions is the derivative of the potential.

Improper dihedral-angle bending force-field

The potential energy associated with out-of-plane torsion dihedral-angles interactions is accounted for by an improper dihedral-angle bending potential in the form of [48]:

$$V^{\xi}(\mathbf{r},\mathbf{s}) = \sum_{i=1}^{N_{\xi}} V^{\xi}(\mathbf{r},\mathbf{s},\xi_0^i) \tag{2.18}$$

where $V^{\xi}(\mathbf{r}, \mathbf{s}, \xi_0^i)$ is the improper dihedral-angle torsion potential energy between four consecutively bonded atoms i, j, k and l forming an out-of-plane angle in a system consist of N_ξ improper dihedral-angles, with ξ_0^i being the equilibrium angle of the i^{th} angle. Knowing the magnitude of the dihedral-angle, ξ, the harmonic interaction potential can be defined as [48]:

$$V^{\xi}(\mathbf{r}, \mathbf{s}, \xi_0^i) = \frac{1}{2} k^{\xi} (\xi - \xi_0^i)^2 \tag{2.19}$$

2.2.3 Van der Waals interaction

The van der Waals interaction potential term, $V^{(vdw)}(\mathbf{r}^N, \mathbf{s})$ is defined by a Lennard-Jones potential function, which is divided into two contributions [48, 67].

$$V^{(vdw)}(\mathbf{r}^N, \mathbf{s}) = \sum_{i}^{N_a} \sum_{j=i+1}^{N_a} \left[\frac{C_{12}(i,j)}{r_{ij}^6} - C_6(i,j) \right] \frac{1}{r_{ij}^6} \tag{2.20}$$

where $C_{12}(i,j)$ is the van der Waals repulsion coefficient, and $C_6(i,j)$ is the dispersion coefficient for the interaction between the i^{th}, and j^{th} atoms separated by a distance of r_{ij}. In Lennard-Jones potentials, the repulsive and dispersive coefficients are defined as [67]:

$$C_{12}(i,j) = 4\epsilon\sigma^{12}, \tag{2.21a}$$

$$C_6(i,j) = 4\epsilon\sigma^6 \tag{2.21b}$$

Here ϵ is the depth of the potential well, and σ is the corresponding distance between the two sites where $V^{(vdw)} = 0$, and the minimum energy distance is $2^{1/6}\sigma$.

The van der Waals energy of the system is calculated by summing all van der Waals pairs in the system. However, it should be noted that those pairs between

atoms forming an angle, or dihedral-angle are excluded form the summation as the effect of the pair interaction is incorporated into the angle, or dihedral-angle torsion potentials.

2.2.4 Energy minimization

A widely used tool in MD simulations to obtain low-energy configurations of the molecular system is energy minimization with an empirical energy function. Some of the function minimization methods used in molecular simulations are noted below:

- Direct search methods, requiring only function values. They converge slowly and are therefore not practical to use [68, 69].
- Second-order methods, requiring function, derivative, and Hessian matrix. These methods are not well suited for application to large systems since they require expensive computations to calculate derivatives and Hessian matrices [48].
- The conjugate gradient methods search along directions corresponding to the local quadratic approximation of the function. This method usually converges super-linearly, which makes it suitable for energy minimization of very large systems. In the following simulations this method is chosen for performing energy minimization of the polymeric system. [70, 71].

2.3 Material system

The material chosen here is an epoxy polymer composed of diglycidyl ether of bisphenol A (DGEBA) monomers with 1,4 diaminobutane (DAB) and N,N'dimethyl-1,6-,diaminohexane (DDH). The chemical structure of the DGEBA epoxy monomer and the DAB and DDH curing agent are shown in Figure 2.1. The curing reaction between DGEBA and a curing agent takes place by the release of a hydrogen atom from

the curing agent and breaking one of the oxygen bonds in the DGEBA monomer, as shown in Figure 2.2. A carbon atom in the epoxy monomer is thus freed such that a nitrogen atom in the DAB curing agent can bond to the DGEBA monomer, while the released hydrogen atom forms a bond with the oxygen atom in the DGEBA monomer. The resulting polymer chain can subsequently cross-link with other monomers to create a cross-linked network based on the availability of reactive functional groups in the monomers. It should be noted that the DAB and DDH curing agents can bond to a maximum of four and two DGEBA monomers, respectively.

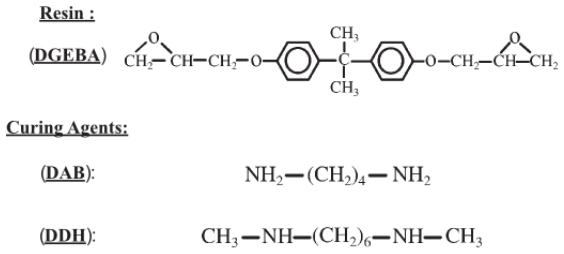

Figure 2.1: The chemical structure of (a) DGEBA, (b) DAB, and (c) DDH.

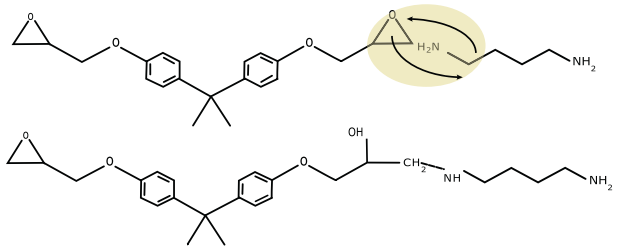

Figure 2.2: The chemical reaction between reactants during the curing process.

2.4 Coarse-Grained Molecular Dynamics Simulations

Coarse-graining is lumping atomic degrees of freedom into coarser particles to capture the high-frequency displacements, while reducing the number of total degrees of freedom in the system dramatically. The coarse-grained molecular methods correctly approximate the molecular properties of systems in which the intramolecular motion

is much less significant than the intermolecular motion. For example, in many materials that are composed of stable chemical compounds, the way these molecules interact as whole groups with each other often determines the physical and chemical properties of the bulk materials. While there are many different approaches for coarse-graining of polymers, they all share two common steps: (1) mapping the atomic structure into coarse-grained particle systems, (2) defining new inter-particle interactions between these coarse-grained particles.

Here, the atoms in the repetitive chemical units of the DGEBA monomer and DAB and DDH cross-linkers are mapped to coarser particles, called "Super-Atoms", as shown in Figure 2.3. The resulting coarse-grained structure for a DGEBA monomer has 20 times fewer degrees of freedom, 18 times fewer number of bonds, 34 times fewer number of angles, and 35 times fewer number of dihedral angles. The fewer number of degrees of freedom along with fewer number of angles and bonds results in a dramatic reduction of resources required for modeling the equivalent atomic struture of the monomer.

The coarse-grained model adopted here for modeling the interaction between different super-atoms follows broadly the model proposed by Tschoÿ *et al.* [44]. The details of the model are discussed in the following subsections:

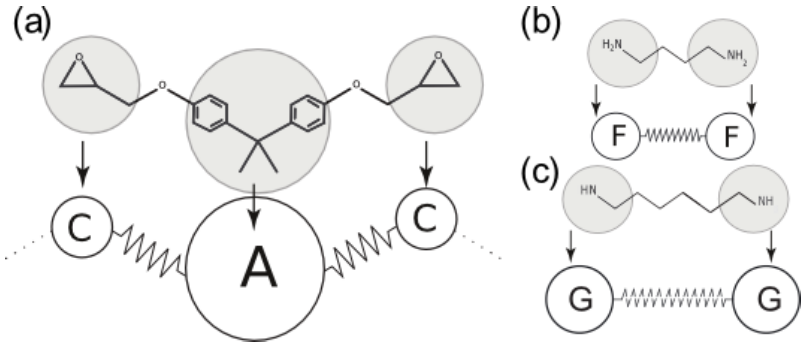

Figure 2.3: Mapping atoms to coarser super-atoms: (a) DGEBA; (b) DAB; and (c) DDH molecules.

2.4.1 Mapping and intra-chain potentials

Here, the interaction between super-atoms representing the repetitive chemical units of the DGEBA monomer and the curing agents are modeled by spring-like bond, angular, and torsional potentials that properly average the high-frequency internal degrees of freedom of the molecules. These potentials are calculated by inverting the Boltzmann distribution density function of their coarse-grained coordinate. The Boltzmann distribution density function of a monomer, P, can be expressed in terms of its atomic coordinates such as bonds, angles, and dihedral angles in the atomic system. The basic requirement of coarse-graining is that both the atomic and coarse grained systems under similar circumstances should reach the same average value for a given macroscopic quantity such a F. Thus, one can write:

$$\int_{\omega} P(l,\theta,\phi)F(l,\theta,\phi) = \int_{\Omega} P(L,\Theta,\Phi)F(L,\Theta,\Phi) \tag{2.22}$$

where for the coarse-grained structure L represents the lengths of the coarse-grained bonds between super-atoms (e.g. L_{AC} in Figure 2.3a), Θ represents the coarse-grained angles between super-atoms (e.g. $\Theta_{\widehat{CAC}}$ and $\Theta_{\widehat{ACA}}$ as shown in Figure 2.3b) and Φ represents the coarse-grained dihedral angles between bonded super-atoms (e.g. $\Phi_{\widetilde{CACA}}$ in Figure 2.3b). It should be noted that the flexibility of polycarbonate structures is mostly due to the rotational degrees of freedom along the carbon backbone structure. Therefore, a random conformation of the system can be achieved by changing dihedral angles on the backbone of its atomic structure while keeping the angles and bonds at their optimum values.

In the first step of calculating the probability density functions of the coarse-grained system, the molecular energy of the system was minimized using the UFF force fields [72, 73]. This optimized geometry then serves as the initial structure for semi-empirical quantum mechanics simulations with Hartree-Fock. The process

begins by selecting one dihedral angle on the backbone of the atomic structure and changing its angle while minimizing the energy of the system with this angle kept fixed. The dihedral angle potential function is computed by calculating the difference in the energy of the system after the system is relaxed with different values of the dihedral angle. The relaxed atomic structure will be adopted for the next sampling step. This process is repeated by selecting another random dihedral angle on the backbone of the relaxed atomic structure. This process is terminated when all the potential function of the dihedral angles along the backbone of the system are calculated. These calculations were performed using the Gaussian90 software [74] using the 6–31G* basis. A Metropolis Monte Carlo sampling method is used to sample the conformations of the atomic system at the desired temperature T. [75]. The locations of coarse-grained super-atoms are calculated from the atomic structures by finding the center of geometry of the groups of atoms in each super-atom. For the coarse-grained system, it is assumed that these coarse-grained coordinates are independent [44], and the probability density function of the system can be factorized as follows:

$$P(L,\Theta,\Phi) = P(L_{AC})P(\Theta_{\widehat{CAC}})P(\Theta_{\widehat{ACA}})P(\Phi_{\widetilde{CACA}}) \tag{2.23}$$

Thus, by computing the PDF of each coarse-grained coordinate, the coarse-grained potential functions can be predicted after accounting for the respective volume elements of the density functions at a certain temperature as follows:

$$\begin{aligned}
U^{L_{AC}}(L) &= -k_B T\, ln\left(\frac{P(L)}{L^2}\right)\\
U^{\Theta_{\widehat{CAC}}}(\Theta) &= -k_B T\, ln\left(\frac{P(\Theta)}{\sin(\Theta)}\right)\\
U^{\Theta_{\widehat{ACA}}}(\Theta) &= -k_B T\, ln\left(\frac{P(\Theta)}{\sin(\Theta)}\right)\\
U^{\Phi_{\widetilde{CACA}}}(\Phi) &= -k_B T\, ln\left(P(\Phi)\right)
\end{aligned} \tag{2.24}$$

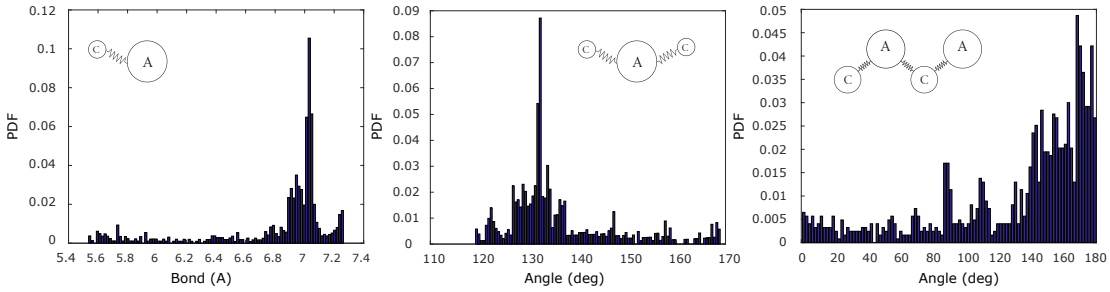

Figure 2.4: The histograms of coarse-grained coordinates (a) bond, (b) bending angle, (c) dihedral angle at $T = 300\,\mathrm{K}$.

Examples of the histogram for a coarse-grained bond, dihedral and $\widehat{CAC}$ angle of the DGEBA monomer at 300 K are shown in Figure 2.4. The computations were repeated for a range of temperatures from $150\,\mathrm{K} \leq T \leq 500\,\mathrm{K}$ and the coarse-grained potential functions for the different coordinates of the DGEBA monomer are shown in Figure 2.5. Then, the coarse-grained potentials are computed at different temperatures for according to equation 2.24. These potentials are parametrized for the coarse-grained MD simulations by fitting the harmonic functions for the bond and angular potentials and an OPLS [76] function for the dihedral potentials to the computed potentials. These simulations were also performed on the DAB curing agents, and cross-linked DGEBA:DAB polymers on a system as shown in Figure 2.3b to parameterize all the conformationally relevant coarse-grained degrees of freedom. Table 2.1 summaries all the optimized parameters calculated for the DGEBA:DAB polymer networks at room temperature. It should be also noted that due to the similarity in atomic structures of DDH and DAB curing agents, the coarse-grained potentials calculated for DAB are used interchangeably for DDH molecules. However, the DDH curing agents can only form two bonds to DGEBA monomers, while DAB curing agents bond with up to four DGEBA monomers.

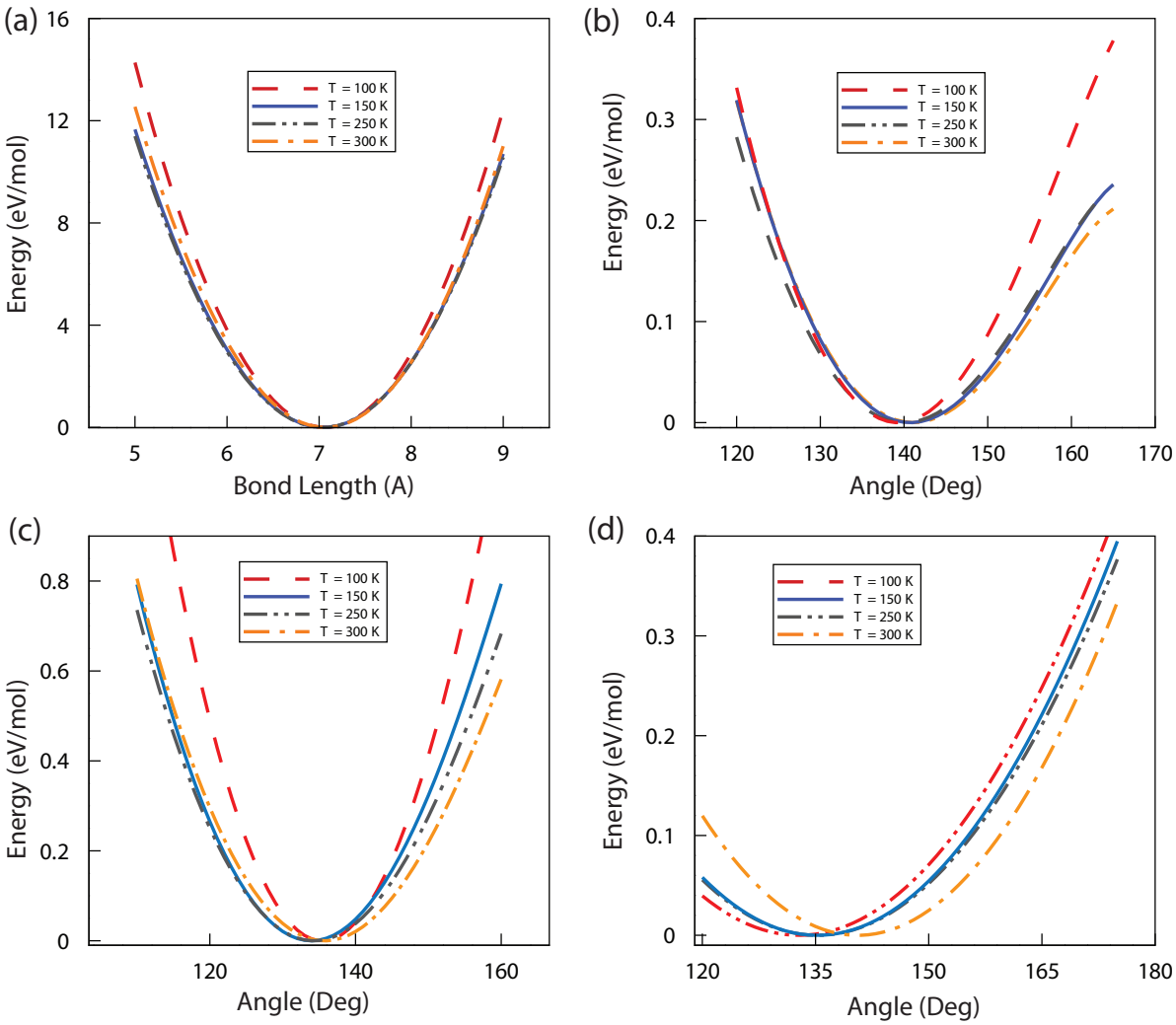

Figure 2.5: The calculated coarse-grained potentials from quantum mechanical simulations at different temperatures. (a) bond potential energy; (b) A-C-A angle potential energy; (c) C-A-C angle potential; and (d) dihedral angle potential.

Bond Potential		K_d	d_{eq}		
	$C \rightleftharpoons A$	5.5903	7.04		
	$F \rightleftharpoons F$	6.942	5.89		
	$F \rightleftharpoons C$	6.652	4.67		
Angular Potential		K_θ	θ_{eq}		
	$\widehat{CAC}$	6.741	136.969		
	$\widehat{ACA}$	3.499	143.125		
	$\widehat{FFC}$	10.944	150.84		
	$\widehat{CFC}$	11.995	65.132		
	$\widehat{FCA}$	8.875	75.13		
Torsional Potential		K_1	K_2	K_3	K_4
	$\widetilde{CACA}$	289.674	-161.759	57.656	-10.1758

Table 2.1: Parameters for coarse-grained potentials calculated at $T = 300$K (Figure 2.3b)

2.4.2 Pair potential

The interactions between non-bonded super-atoms in the network are described using a Lennard-Jones (LJ) potential function described by Equation 2.20. The Lennard-Jones potential is chosen since it results in a temperature independent self-diffusion coefficient at a constant density [44]. The cut-off radius of the LJ potential is 2.5σ. Here, the values of σ and ϵ are optimized to reproduce the experimentally measured density and glass transition temperature of the material. In the optimization procedure, the initial values for these parameters are chosen as $\epsilon = 2.5\,\mathrm{kCal\,mol^{-1}}$ and $\sigma = \left(\frac{\Psi M_m}{3\rho}\right)^{1/3}$, where Ψ is number density, ρ is the real density and M_m is mass of each monomer in grams. A number of simulations with different LJ potential parameters in the range of $\pm 25\%$ of the initial guess were performed. In these simulations, the temperature of the simulation cell is decreased from 700K to 100 K and the density is constantly calculated to find the glass transition temperature. The optimum set of parameters that are selected for the LJ potential in the current model is those that minimize the objective function:

$$f(\mathbf{x}) = \sum_{i=1}^{N=2} \left[\frac{g(\mathbf{x})}{X_i} - 1 \right]^2 \tag{2.25}$$

where $\mathbf{x} = \{\epsilon, \sigma\}$, $g(x)$ is the predicted values, and X_i $(i = 1, 2)$ are the known experimentally measured glass transition temperature and density. The optimized values are computed to be $\epsilon = 1.519\,\mathrm{kCal\,mol^{-1}}$ and $\sigma = 5.382\,\text{Å}$, which lead to a predicted density of $1.21\,\mathrm{g\,cm^{-3}}$ at room temperature and a glass transition temperature of $388 \pm 5.5\,\mathrm{K}$, which are in good agreement with experiments [6].

2.5 Bond Breaking Criteria

It has been observed from molecular simulations of polymeric systems that bonds, and angles between atoms remain intact before strain hardening begins [12, 21]. Therefore, it is common in coarse-graining models of polymer systems that bond breaking is neglected, especially when modeling of polymers in water or gel systems [41, 44, 47].

On the other hand, in the current method, bond breakage is accounted for by assuming a smooth transition from a bonded state, where a harmonic potential governs the interaction to a non-bonded state with van der Waals potential. In fact, the interaction, between the i^{th} and j^{th} super-atoms that are initially bonded and then transition to a van der Waals state can be calculated by the following equation:

$$V^{brk}(d_{ij}) = U_b + \mathcal{H}(d_{ij} - d_{brk}) \times V^{bnd}_{har}(d_{ij}, \mathbf{s}) + \mathcal{H}(d_{brk} - d_{ij}) \times V^{(vdw)}(d_{ij}, \mathbf{s}) \tag{2.26}$$

where $\mathcal{H}$ is heaviside function, and $V^{bnd}_{har}(d_{ij}, \mathbf{s})$, and $V^{(vdw)}(d_{ij}, \mathbf{s})$ are the bonded, and van der Waals potential defined previously. The value of d_{brk} is the bond breaking threshold which is optimized to generate a smooth continuous transition potential, which is equal to $1.1234 d_0$ for the bond along the DGEBA monomers. Here, to

simplify the model and simulations, it was assumed that only bonds along the DGEBA monomer break.

2.6 Summary and Conclusions

In this chapter, a new coarse-grained model for DGEBA polymer cured with DAB, and DDH curing agents was developed. The coarse-grained potentials for each coordinate defined between these super-atoms are calculated by collecting a large dataset of random-walk conformation of the system using the probability functions calculated for each dihedral angle at different temperatures. The pair potential between non-bonded super-atoms is optimized to correctly replicate the experimentally measured glass transition temperature of the epoxy. A summary of the findings include:

- The atomic model is coarsened by lumping groups of atoms into larger particles called super-atoms.
- The resulting coarse-grained structure for a DGEBA monomer leads to a system containing 20 times fewer degrees of freedom, 18 times fewer bonds, 34 times fewer angles, and 35 times fewer dihedral angles as compared to a fully atomistic system.
- The coarse-grained interaction potentials are defined by Boltzmann inversion technique.
- The pair potential is optimized to reproduce the experimentally measured density of the epoxy at different temperatures, as well as the glass transition temperature.
- A bond breaking criteria is introduced into the model by assuming a energetically smooth transition from a bonded state to a non-bonded state.

Chapter 3

New Method for Simulating for the Curing Process of Highly Cross-Linked Polymers

3.1 Introduction

For realistic simulations of epoxy polymer systems, the starting chain network in the simulations should represent a realistic cross-linked amorphous microstructure with the correct degree of cross-linking. The formation of these models for crosslinked networks has been studied by several authors, with the early motivations of understanding the reaction kinetics of cross-linking process [77, 78]. These methods mainly used Monte-Carlo techniques to simulate the kinetic of cross-linking in terms of degree of polymerization, molecular weight distribution, polydispersity and sol-gel transition. However, in these studies, useful information related to mechanical as well as thermodynamic properties are lost since these models did not account for the topological information of the network [79]. Later on, MD simulations were used to create a cross-linked network with topological information through several cross-linking ap-

proaches. The basic approach is typically focused on modeling a mixture of curing agents and epoxy monomers, which diffuse in a heated melt. When a curing agent is in a bond forming vicinity of a reactive epoxy monomer, a bond is created. This process is terminated when the desired degree of cross-linking is obtained [5, 80].

In one of the first attempts, a Poly methyl 2-methylpropenoate (PMMA) network was created using lattice-based simulations using a polymerization molecular dynamics scheme [81]. A methodology to cross-link low molecular weight water-soluble phosphate-modified epoxy resins was also proposed that successfully simulated the cross-linking reactions [82]. However, in both techniques the bond forming reactions were carried out simultaneously and in a single step, which led to a sudden change in the energy and entropy of the melt [83]. On the other hand, in a different approach, cross-linking was performed using an iterative mix of molecular dynamics and a molecular mechanics procedure where the newly formed topology is subjected to 1000 MD steps of relaxation. This approach carries out one cross-link per iteration, which is bound to have computational limitations when applied to cross-linking of larger systems [5, 80, 84–86].

More recently, a cross-linked network for EPON-862 epoxy resins was built to study the interfacial interactions during stress transfer [87]. This study provided insightful information about the material properties and interfacial interactions, without discussing the details of the cross-linking process. It should also be noted that most of the simulations of the formation of the cross-linked networks have been carried out for small systems. Furthermore, it has been shown that the rate of reaction in curing larger epoxy network systems dramatically decreases and cross-linking reaches a saturated state when the system converts to a gel after the first several thousands of steps in the simulation [88]. Thus, there is a need to develop a new methodology that is efficient to be able to create highly cross-linked networks.

The chapter is organized as follows. In the next section, a new strategy is pre-

sented with the main focus on the cross-linking procedure. Thereafter, the results on the analysis of thermodynamic and molecular properties as a function of cross-linking are presented. The results of the new algorithm are also compared with other available experimental and simulation studies.

3.2 Curing Algorithm

The curing process of highly cross-linked polymer networks consists of mixing curing agents and polymer monomers in a heated liquid melt until they form the required chemical bonds. The resulting unique structure of these polymer networks should be properly captured in the initial microstructure of fully atomic or coarse-grained MD simulations used for studying other properties of the material.

Traditionally, in simulations of the curing process, a melt composed of a mixture of prepolymers and curing agents is randomly placed in a cubical simulation cell having periodic boundary conditions imposed along all directions. The constituents are then allowed to diffuse in the simulation cell at a constant high temperature and pressure. A bond is formed with a certain probability every time the reactive end of an epoxy monomer is at a critical distance from curing agents. The simulation is then terminated when the required degree of cross-linking is achieved in the network [5].

This cross-linking algorithm typically generates good representative epoxy networks in systems having a small number of atoms. However, for systems having a large number of atoms, or if a high degree of cross-linking is required, this algorithm results in a system that reaches a saturated state at a degree of cross-linking lower than the desired value within several thousand simulation time steps [88]. Furthermore, this algorithm typically leads to a non-uniform distribution of cross-linked monomers inside the simulation cell for networks with high degrees of cross-linking.

On the other hand, in simulations where lower degrees of cross-linking are required, the short chains that were initially generated inside the simulation cell form bonds with their neighbors and nearest neighbors, which may result in the formation of chains that are comparatively longer than the desired average length of cross-linking [56].

To overcome these issues, here, a new algorithm is developed that not only prevents the formation of long uncross-linked chains, but also guarantees uniformity of the distribution of cross-linked monomers. In this approach, groups of partially cross-linked chains of epoxy monomers and curing agents, as shown in Figure 3.1, are used. These prepolymers are DGEBA monomers with a random degree of polymerization between 3 to 6 bonded through DAB curing agents. A mixture of these groups is randomly positioned within the simulation cell having periodic boundary condition imposed along all directions. These partially cross-linked chains ensure that long uncross-linked chains are not created.

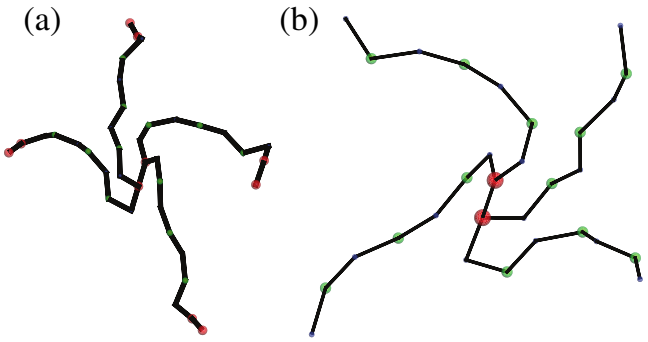

Figure 3.1: Partially cross-linked molecules used for cross-linking (a) Partially cross-linked epoxy (non-active) (b) Partially cross-linked epoxy with curing agents at its ends (active). The red beads are the cross-linker super-atom, while the green and blue beads represent the A and C epoxy super-atoms, respectively

In addition, to create a uniform cross-linked network, first, the simulation cell is divided into smaller regions. The inhomogeneity index of each region is then determined by subtracting the number of active curing agents from the number of reactive

DGEBA monomers. This number indicates whether there is a lack of curing agents in the region. In order to increase the likelihood of the bond forming in each region, the velocities of super-atoms of each curing agent that has not formed bonds with DGEBA polymers are modified such that the curing agent is pushed to its closest neighboring region that has less available reactive super-atoms. This modification is done by changing the direction of the velocity components of each super-atom toward its closest neighboring region that has an absence of cross-linkers. This modification may cause a spurious translation of the region to one direction. In order to remove the effects of these spurious translations on the system, after each modification step the velocity of the center of geometry of the system is calculated. The difference between the post-modification and pre-modification translational and angular velocities of the center of geometry of the region is averaged across all the super-atoms in the region to maintain the overall speed of the system. To conserve the temperature of the region after modifications, the velocities of super-atoms in each region will be scaled to match the temperature of the pre-modified system. After each redistribution step, the system is equilibrated to maintain the energy state of the system. This redistribution algorithm prevents locking reactive monomers in one region when there is a higher chance of bond forming in other regions, and mimics the process of shaking or stirring the system. Furthermore, if bond forming is allowed without any control of the rate of bond formation in different local regions, regions with a higher number of reactive super-atoms will exhibit a much faster rate of cross-linking formation. This will lower the mobility of uncross-linked super-atoms in these regions. Therefore, the redistribution of these super-atoms becomes harder, and a significantly longer time is required for them to be redistributed, which may not be attainable in the simulations time frame. It is especially important to control the rate of curing in the early steps knowing the redistribution will be highly restricted after a gel is formed during the curing process. To avoid this, the rate of curing is controlled in every region by

enforcing a probability of bond formation for a chemically reactive pair of epoxy and curing agents in every region as a function of the local degree of cross-linking, such that:

$$a = a_{min} + \mathcal{H}(\chi_{target} - \chi_{local}) \times \left(\frac{\chi_{cell}}{\chi_{target}}\right) \times a_{max} \times \left(\frac{\chi_{cell}}{\chi_{local}}\right) \tag{3.1}$$

where a is the acceptance rate, $\mathcal{H}$ is the Heaviside function, χ is the degree of cross-linking, which is calculated as the ratio of the number of available pairs of reactive super-atoms to the number of bonds formed in that region. Equation (3.1) severely slows down the curing process in the early stages of the simulations allowing the curing agents to redistribute evenly across the simulation cell. This equation will eventually increase the probability at which available pairs of reactive super-atoms successfully form bonds as the average degree of cross-linking of the simulation cell becomes closer to the target degree of cross-linking. This adaptive acceptance rate function leads to a uniform degree of cross-linking over the entire simulation cell even for networks with a low degree of cross-linking. It should also be noted that when a bond is created during the curing process, several angles and dihedral angles are formed between the two super-atoms at the ends of the bond and their neighboring super-atoms. These newly formed angular and dihedral coordinates are usually neglected in most coarse-grained models due to the complication in assigning the correct type of potential for each coordinate during the simulation. This new algorithm was included in a new library (USER-CRSLNK) for LAMMPS [89] that can dynamically detect the type of each coordinate based on the type of its forming atoms.

3.3 Results and Discussion

In the following, all simulations are conducted using LAMMPS [89]. The epoxy network is created by randomly generating a mixture of partially cross-linked DGEBA:DAB

reactive (33% mol) and active (66.7% mol) molecules in a cubical simulation cell having an edge length of 75 nm. Periodic boundary conditions are imposed along all directions to mimic the bulk properties of the epoxy network. The molecules are modeled using the coarse-grained bead-spring model as discussed previously. The initial system is a liquid mixture of the different molecules at a density of $1.16\,\mathrm{g\,cm^{-3}}$. It should be noted that in general the variations in the chain lengths, degree of cross-linking, and/or variation in the pre-polymerization structures chosen can affect the final predicted properties of the polymer networks. However, these effects are beyond the scope of the current study and are thoroughly investigated separately in Chapter 5. The LJ potential is disabled at this stage of the simulation, to avoid high repulsive forces if two atoms are placed very close to each other, which would severely decrease the integration time-step in the simulations. Instead, a soft cosine pair potential is employed:

$$U_{soft} = A + A\cos\left(\frac{\pi r}{r_0}\right) \tag{3.2}$$

where $r_0 = 2^{\frac{1}{6}}$ Å. The amplitude A is linearly increased from 0.0 to 100.0 kCal/mol over the first 50,000 time-steps to gradually move overlapping molecules away from each other. The system is then relaxed using the NVE ensemble with the displacement of super-atoms limited to 1 angstrom for 500,000 steps. Finally, the network is relaxed at the simulation temperature for one million time-steps. The simulations are conducted using the NPT ensemble where the Nose-Hoover thermostat and barostat are employed to control temperature and pressure during simulations. The temperature and pressure damping parameters are set to 200 and 1000 femtoseconds, respectively. Time step is 2.5 femtoseconds. These parameters are consistent with coarse-grained simulations of the curing process published in the literature [21, 81, 83]. The same simulation parameters are used for each simulation unless otherwise stated.

In simulations of the cross-linking process, the simulation cell is randomly populated with prepolymers and curing agents relaxed at 600 K. These molecules are then

allowed to diffuse inside the simulation cell with constant temperature and pressure conditions. When a reactive super-atom of DGEBA is in a bond forming vicinity of a reactive super-atom of the curing agent, a chemical bond is formed. The bond forming radius chosen as $1.6\,\sigma$. At this stage of simulation, a fictitious potential with a stiffness 100 times stiffer than the previously calculated potentials are used for bonds, angular, and torsional degrees of freedom. This is a common techniques used in coarse-grained simulation of curing process to avoid harmonic bonds from passing through each other, and forming long bonds in the cross-linking simulations [81, 83]. After the desired degree of cross-linking is achieved, the system is relaxed for 1,000,000 time-steps with the correct potentials to remove any artifacts caused by the stiffer intra-chain potentials during cross-linking simulation.

In order to show the effects of controlling the rate of bond formation, redistribution of curing agents, and the use of partially cross-linked pre-polymers in the curing process, here, a comparison is made between the traditional [5] and our new proposed curing algorithms by deactivating one of these features in three different simulations. The average degree of cross-linking in the simulation cell as a function of the number of simulation time steps for these simulations are shown in Figure 3.2. The first observation is that in the curing simulation, with no control over the rate of bond formation, the rate of the formation of bonds is as high as the traditional algorithm, and it also reaches a saturated states relatively early, tho at a higher degree of cross-linking due to the limited redistribution of curing agents in the early steps of the simulation. The importance of redistribution of curing agents is highlighted in the simulation with no redistribution process, shown as the green solid line in Figure 3.2, where the rate of bond forming is slow at the beginning of the simulation, and the final degree of cross-linking obtained from the simulation is only slightly higher than the traditional algorithm. At last, regular DGEBA pre-polymers and DAB curing agents are used instead of partially cross-linked molecules in the curing simulation ,

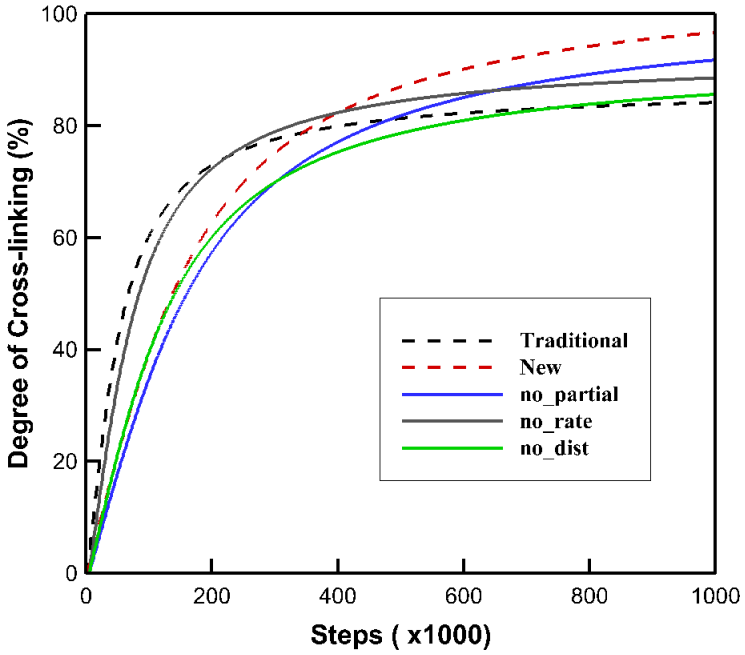

Figure 3.2: Comparison between the curing process by disabling rate control process, distribution process, and using regular pre-polymers.

as shown by the blue in Figure 3.2. It is clear that the redistribution of curing agents in a system in which the rate of bond forming is controlled is more effective than the other two combinations. The system is not saturated at the end of the simulation and has reached the highest degree of cross-linking of all four systems.

Finally, the average degree of cross-linking in the simulation cell as a function of the number of simulation time steps using both the traditional [5] and the new proposed curing algorithm are shown in Figure 3.3. In addition, the distributions of the local degree of cross-linking throughout the simulation cell are shown for both algorithms at three different time-steps in Figure 3.4. After 200,000 time-steps, marked as $\boxed{1}$ in Figure 3.3, the traditional algorithm shows a $63 \pm 8.5\%$ degree of cross-linking compared to $56 \pm 3.5\%$ for the new algorithm. In the new algorithm, the bond formation reaction is decreased in regions with a higher degree of cross-linking, while

the reaction rates are increased in other regions with the lower degree of cross-linking to create a uniformly cross-linked network. Therefore, during the early stages of the simulation, a lower average degree of cross-linking is reached compared to the traditional algorithm where reaction rates are uniform throughout the simulation cell. After $325,000$ time-steps, marked as $\boxed{2}$ in Figure 3.3, the degree of cross-linking in both algorithms is equal to 78%, however, as shown in Figure 3.4b the new algorithm shows a much more uniformly-distributed cross-linked network (standard error of $\pm 5.4\%$) as oppose to the traditional algorithm where a wider distribution of cross-linking is observed across the simulation cell with a standard error of $\pm 10.3\%$. After $750,000$ time-steps, marked as $\boxed{3}$ in Figure 3.3, the average degree from the new algorithm is $95 \pm 3.2\%$, while in the traditional algorithm the degree of cross-linking did not change much above the 80% value reached in $\boxed{2}$. This is due to the fact that the cross-linking rate in the traditional algorithm drops dramatically as reactive super-atoms are trapped in areas with the higher degree of cross-linking, while there is a lack of reactive units in other regions to form bonds. On the other hand, the new algorithm shows a better performance as it redistributes reactive super-atoms from areas with higher degree of cross-linking to areas with lower degree of cross-linking.

The simulation volume during the cross-linking process as a function of the degree of cross-linking as predicted by the new algorithm is shown in Figure 3.5a. The decrease in volume during the curing simulation is in good agreement with the increase in density predicted by fully atomic MD simulations [90]. The volumes of the relaxed microstructure as a function of time, before and after curing are shown in Figure 3.5b. The cured network is observed to result in a volume shrinkage of 5% at a degree of cross-linking 95%, which is in accordance with volume shrinkage observed of the cured microstructure [82]. Furthermore, the gel point of the system during the curing processed is measured. One way to measure gel point of the system is to plot

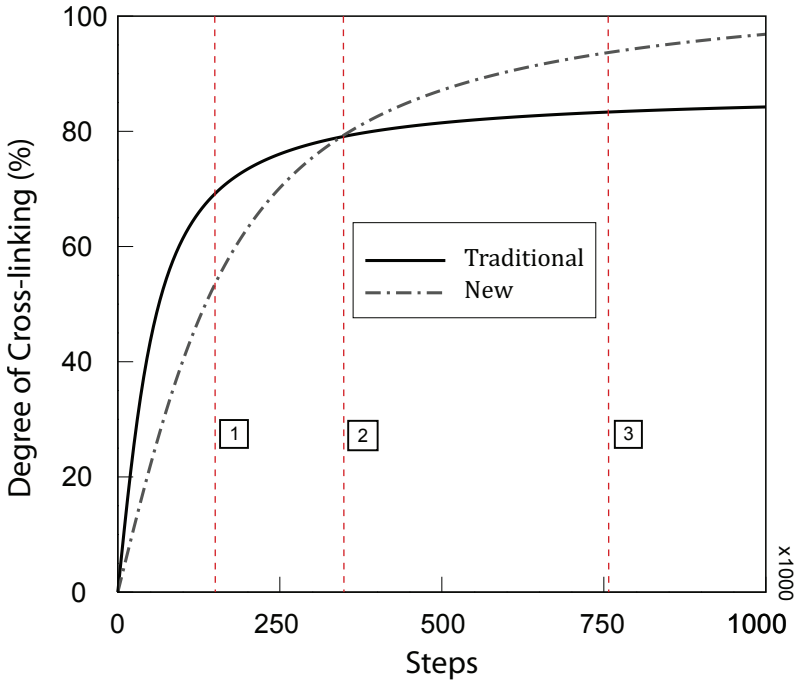

Figure 3.3: A comparison between the traditional [5] and the current cross-linking algorithm. Numbers in squares indicate the steps at which the microstructures in Figure 3.3 were generated at.

the molecular mass of the largest polymer block as a function of curing conversion [83]. A polymer block is a group of polymer chains are that cross-linked and chemically bonded. The system will convert to a gel at the curing conversion rate when the a sudden rise in the molecular mass of the system is observed. The molecular mass of the largest polymer block is shown in Figure 3.6. It is observed that most of the largest polymer bluck are formed during $65 - 70\%$ cure conversion process. The calculated gel point during the curing process is at 67% cure conversion percentage, which is in good agreement with the theoretical cure conversion percentage of 58%, as well as the experimental measures, which are in the range of $50 - 80\%$ [91, 92].

To study the temperature dependence of the cross-linked network, a simulation was performed to calculate the glass transition temperature. By definition, the glass transition temperature, T_g, is the reversible transition in amorphous materials or in amorphous regions within semi-crystalline materials from a molten or rubber-like

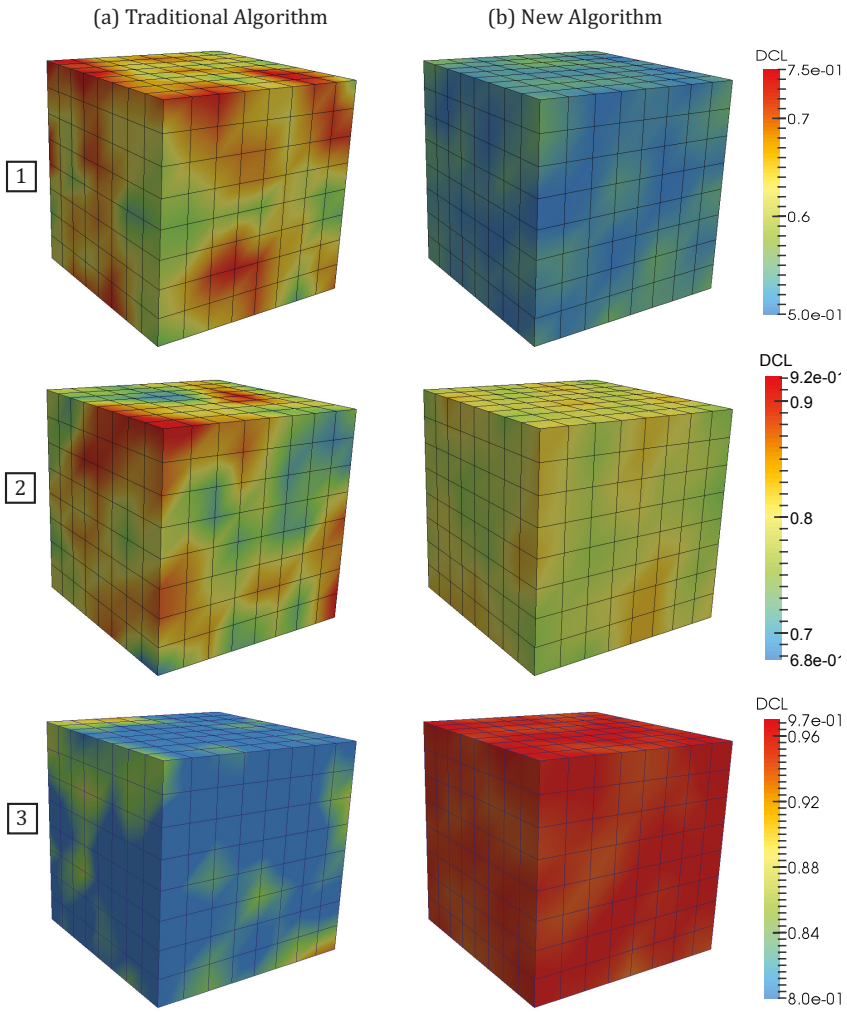

Figure 3.4: Contours showing the degree of cross-linking throughout the simulation cell from (a) the traditional [5], and (b) the new cross-linking algorithms at different steps as indicated in (Figure 3.3).

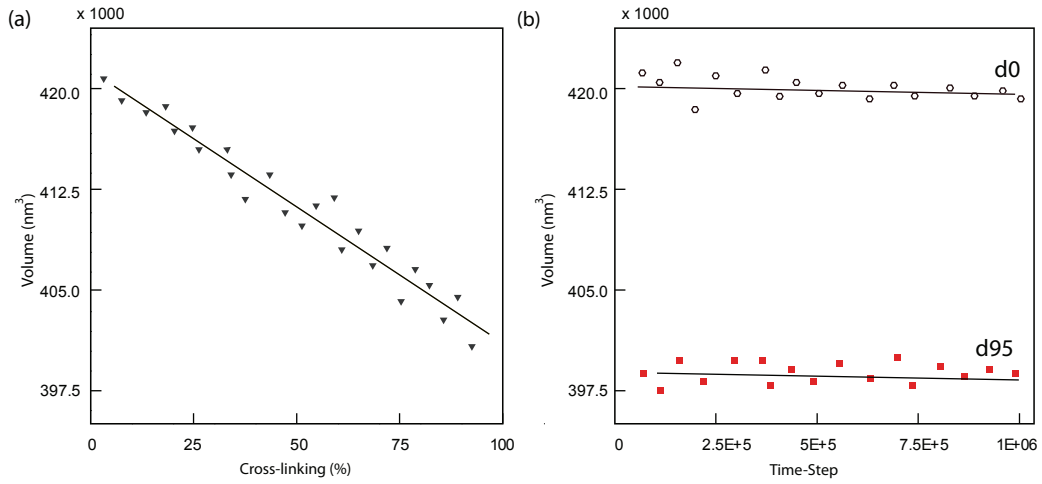

Figure 3.5: (a) Simulation cell volume as a function of degree of cross-linking. (b) Comparison between densities of an uncross-linked and tightly cross-linked (95% cross-linking) network

.

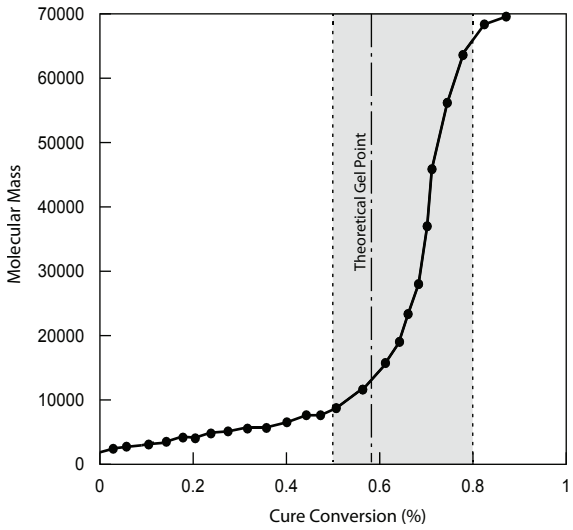

Figure 3.6: Molecular mass build-up as a function of cure conversion. The shaded area indicates the experimentally observed range of gel point, and the dash-dot line indicates the theoretically predicted value.

state to a hard and relatively brittle state [10]. One way to measur the glass transition temperature is to find the temperature where a kink is observed in the specific volume (ρ^{-1}). To calculate the glass-transition temperature, the epoxy microstructure is first relaxed at 700 K. The simulation temperature is then reduced to 150 K in 4×10^6 time-steps with a time step of 2.5 femtoseconds. The density versus temperature for the DGEBA:DAB cross-linked network is shown in Figure 3.7a. The calculated glass-transition temperature of the system is predicted by the current simulations to be 389 ± 8.5 K, which is in a good agreement with the experimentally measured glass-transition temperature of 393 K [6]. It should be noted that a comprehensive study on the effect of the cooling rate on the predicted glass transition temperature of polymers from MD simulations has been previously performed [93]. Based on that study it was shown that the glass transition temperature from MD is less sensitive to the cooling rate than that in experiments. Nevertheless, the predicted glass transition temperature from MD simulations is always within the error measurements of experimental data. Another important thermodynamic property is the coefficient of thermal expansion, which is defined as:

$$\alpha = \frac{1}{V}\left(\frac{\partial V}{\partial T}\right)_P \tag{3.3}$$

where V, P and T are volume, pressure, and temperature of the sample, respectively. The change in volume ($\frac{dv}{V}$) versus temperature as predicted from the current simulations is shown in Figure 3.7b. The kink suggests a glass transition temperature of 385 ± 6.5 K ,which complies with experimentally measured glass transition temperature of the material. On the other hand, the thermal expansion coefficient of the rubbery epoxies are roughly 3 times higher than their thermal expansion in glassy region [10]. It is also observed that the slope of the rubbery region is 3.66 times higher than the slope of glass region, which is in a good agreement with the experimentally observed trend.

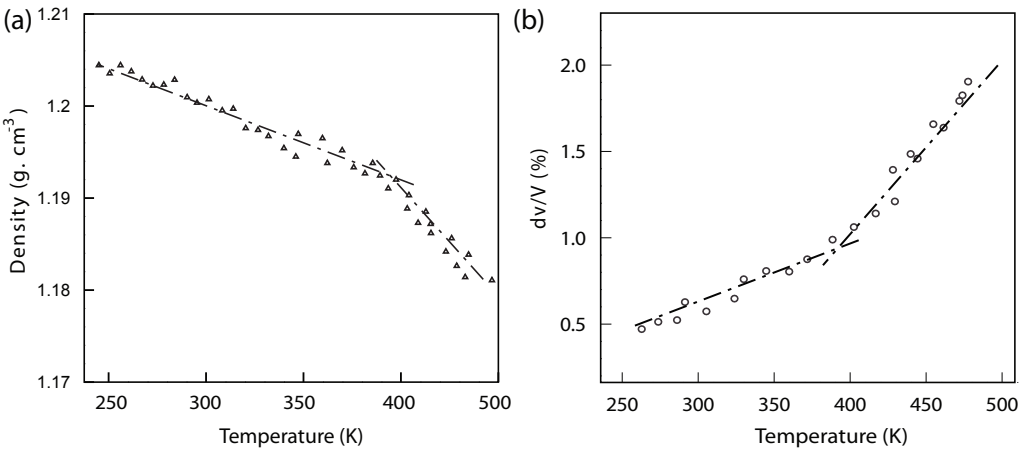

Figure 3.7: (a) Density; and (b) specific volume as a function of temperature.

3.4 Summary and Conclusions

In this chapter, a new curing algorithm was proposed for creating large highly cross-linked systems. The main advantage of the proposed curing algorithm over current curing algorithms in the literature is that it creates a uniformly cross-linked structure regardless of the degree of cross-linking of the system, and allows for creating cross-linked polymer networks with a very high degree of cross-linking. A summary of the findings is listed below.

- A new curing algorithm was developed to create highly cross-linked polymer.
- This algorithm creates a uniformly cross-linked microstrcuture regardless of the desired degree of cross-linking of the system.
- This algorithm prevents reaching a premature saturated state before reaching the final degree of cross-linking by continuously shaking the molecules out of immobile regions.
- The gel point calculated from the curing simulations is in good agreement with experiment, and theory.

- The shrinkage of the system after cross-linking is in good agreement with experimentally measured shrinkage of cross-linked epoxies.

Chapter 4

Quantifying the Distribution of the Free-Volume Holes in Polymeric Networks

4.1 Introduction

One key factor in the characterization of polymer sub-atomic microstructure is the existence of free-volume holes, which are defined as the volumes between polymer chains within the microstructure. The free-volume holes are typically characterized as spherical or ellipsoidal volumes that are confined by the polymer chains in the network [28, 29]. With sufficient imposed thermal and/or mechanical energy, polymer chains can move into the free-volume holes and undergo large conformational changes, while bonds and angles on the backbone of the atomic structure remain intact [29]. The size of these free-volume holes are directly associated with the energy of their surrounding atoms. When these atoms are tightly packed, the energy fields in the core of these volumes are higher. As a result, the energy required for the atoms to move into these volumes are high, and consequently these atoms are comparatively

less mobile than those around larger volumes [94]. In addition, the topology of the polymer network is important in understanding the mobility of the chains in the system. The free-volume associated to the chain ends is larger than the free-volume holes associated to the cross-linked chains [27, 28, 94, 95]. Therefore, in an entangled network where there are more free chain ends compared to a cross-linked network, polymer chains move more freely.

The evolution of the distribution of free-volume holes can help explain the molecular origins of mechanical properties of polymers, such as plastic deformation [96], and the dependence of polymer properties on temperature and pressure [27, 97]. There is also a free-volume based theory to explain the viscoelastic properties of polymers [97] that describes the kinetic and dynamic behavior of polymeric chains and free-volume holes in the matrix. Therefore, it is of great importance to characterize the distribution of free-volume holes and quantify their evolution in polymeric systems.

The free-volume hole distribution in a polymer network is experimentally measured using positron annihilation lifetime spectroscopy (PALS). PALS experiments are based on the fact that annihilation of ortho-positronium (o-Ps) particles in low electron density regions of structure such as vacancies in the crystalline systems or the free volume holes in the amorphous ones is a very sensitive indicator of the size of these regions [27, 28]. Since the annihilation time of a o-Ps is a direct function of the size of the low density region that the particle flies through, the distribution of the size of these regions inside a system can be measured if the annihilation time of o-Ps, created in a reaction of a positron with the electron cloud of its surrounding environment, is formulated as a function of size of these regions [28, 94, 95]. In the calculation of the distribution of the size of the free-volume holes, the shapes of these regions are typically quantified as spheres. Thus, the distribution of low electron density regions inside a system can be measured as the distribution of radii of their representative spheres. Nevertheless, despite experimental advances in quan-

tifying free-volume holes, experimental investigations of the molecular mechanisms of polymeric materials still suffer from complications and difficulties associated with collecting conformation specific data [21, 52, 53].

Numerical methods such as molecular dynamics (MD) simulations have been extensively used to deduce the molecular details of plastic flow, glassy response, and the pressure temperature dependence of polymeric systems [12, 13]. Many MD investigations have also shown a correlation between the many polymer properties and the degree of cross-linking [13], network connectivity [19], curing agent functionality [19], and chain configurations [24]. While such MD studies have provided a wealth of knowledge, there is still a lack of understanding of the role of microstructure variations on the predicted properties of polymers. The first attempt in quantifying cavities and voids from MD simulation was voxelizing space in which the simulation cell is voxelized, and each voxel is tagged as free or occupied to create a qualitative pattern of the cavity in the system [98]. In another work based on the work by Rigby et. al probe of different radii was used to break down the cavities into spheres with the sizes comparable to those measured from PALS [99]. This method was used in a series of studies to calculate the free-volume size of atomic systems [100–104]. More recently, the method of voxelizing space was vastly optimized to calculate free-volume of microstructures at different temperatures for system composed of thousands of polymer chains [105]. Nevertheless, the major drawback of this method is the time and resources needed to analyze larger systems for calculation of free-volume holes. For instance, voxelizing a simulation cell with an edge length of 20 nm with the voxel size of 0.5 Å requires resources large enough to store information of 64,000,000 voxels in addition to the information associated with the location and size of the atoms in the system. This problem precludes the use of this method for calculation of the free-volume holes in coarse-grained MD simulations, where the size of simulation cells are considerably larger.

In this chapter, a new model is developed to accurately find and quantify the free-volume hole distribution within large scale polymer networks. The predicted free-volume hole distributions from the simulations are compared to those measured from PALS experiment to verify the model.

4.2 Experimental Quantification of Free-Volume Hole Distribution

4.2.1 Positron annihilation lifetime spectroscopy (PALS)

The positron, the anti-particle of the electron, has identical properties to electrons with the exception of having the positive charge. Positrons can be generated by various nuclear reactions, which results in pair production followed by high-energy irradiation. The most common source of positrons is Na which emits a positron bream through a nuclear decay to Ne [28]. Because the void volumes make up a sizable portion of the volume of the material, the positrons directed into an epoxy system sense the exsitance of these free-volume holes. Theoretical and experimental studies on the interaction of a positron with its surrounding solid has shown that positrons are more energetically stable in the vacuum than in the vicinity of the solid, which is due to a strong repulsive potential between the ion core and the positively charged positron [27, 28].

PALS is a sophisticated method to measure the free-volume hole distribution in polymeric materials. The free-volume hole distribution is measured by measuring the annihilation time along with angular deflection of the emitted positron beam into the material. When a positron is flying across a polymeric material, it may pick up an electron from its surrounding molecules and form a positronium (Ps). Thus, a positron in a polymeric material can have two possible states at the time of annihila-

tion: delocalized/localized positron state, free delocalized/localized Ps state [27, 28]. The localized sites are the low electron density regions, which are more energetically favorable sites for positrons and Ps. Therefore, the annihilation signals of the emitted beam are mostly contributed from them. Ps atoms can have two separate states due to their different spins, an anti-parallel spin state, which is called para-positronium, and a parallel spin state that is called ortho-positronium (o-Ps). Studies show that these particles annihilate with distinctly different rates depending on the state in the microstructure depending on the size of the free-volume holes. In PALS experiment, it is the o-Ps lifetime that directly correlates to the size of free-volume holes [28, 95]. Therefore the intensity of the o-Ps component of the annihilated beam has information on the size of the free-volume holes.

The annihilation time of the positron inside the microstructure can be written as [27].:

$$\tau = \sum_{i=1}^{N} I_i \exp^{-\lambda_i t} \tag{4.1}$$

Decomposing the annihilation time into three components, the shortest-lived component, τ_1, is attributed to the annihilation of p-Ps molecular particles. The intermediate-lived component is attributed to the direct annihilation of positrons and positron-molecular species. The long-lived component, is annihilation of o-Ps atoms inside free-volume holes. Using qunatum mechanics models, the annihilation time of positrons in free-volume holes is formulated as a function of radius of free-volume hole as below [27, 28]:

$$\lambda = 2\left[1 - \frac{R}{R_0} + \frac{1}{2\pi}\sin\left(\frac{2\pi R}{R_0}\right)\right] \tag{4.2}$$

where R_0 is $R + \Delta R$ and ΔR is an empirical parameter calculated by fitting data with the known hole and cavity size. In amorphous materials the annihilation time

of the localized positrons in a subnanometer-size hole of the free volume decreases dramatically from 142 ns for self-annihilation in infinitely large holes in a vacuum to a few nanoseconds that reflects the hole size at the moment of annihilation [28, 95]. It should be mentioned that PALS experiments are suitable for measuing the mean volume of the holes and, their size distribution. However, it is impossible to directly measure the local hole density or the hole fraction of a volume. Thus, numerical methods can alternatively provide more information on the local distribution of free-volume holes as well as their mean values and distributions.

4.3 Numerical Quantification of the Free-Volume Hole Distribution

In order to quantify the free-volume holes inside the simulation cell, first, a volume needs to be assigned to different super-atoms. Knowing van der Waals increments of atomic volumes [106], we can calculate the total volume of one super-atom as the smallest ellipsoid that encapsulates all the atoms in the super-atom. The radius of super-atoms in DGEBA, DAB, DDH atomic structures are shown in Figure 4.1.

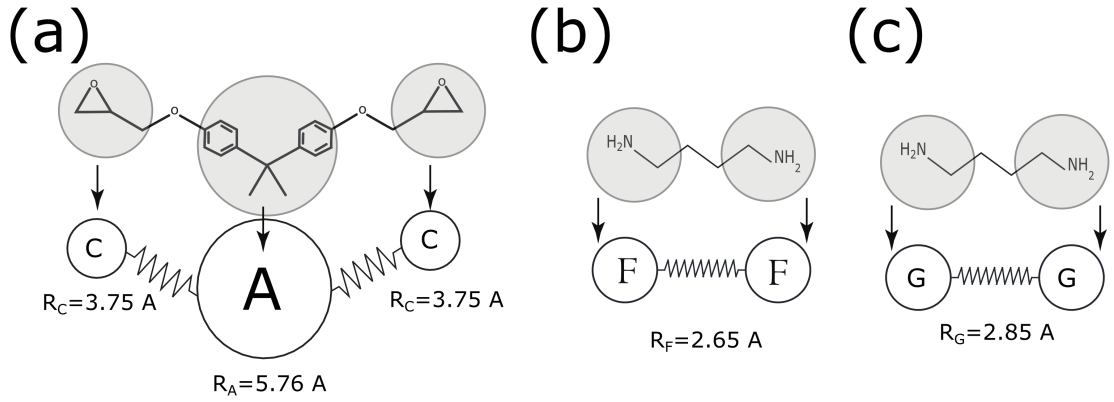

Figure 4.1: Volume of super-atom in (a) DGEBA, (b) DAB, and (c) DDH molecules.

To characterize free-volume holes it is very important to differentiate between free-volume holes in cross-linked regions versus those in entangled regions of the microstructure. A two dimensional (2D) schematic of free-volume holes in a cross-linked and an entangled network are shown in Figure 4.2. In a cross-linked network, low electron density regions are the volumes between groups of cross-linked networks that are wrapped by polymer chains. The free-volume associated to the free ends of polymer chains are larger than those inside a cross-linked system [101, 105]. Therefore, o-Ps particles annihilate faster in a cross-linked network, which results in detection of smaller free-volume holes in a cross-linked system via PALS. Thus, for a given system, increasing degree of cross-linking will reduce size of free-volume holes.

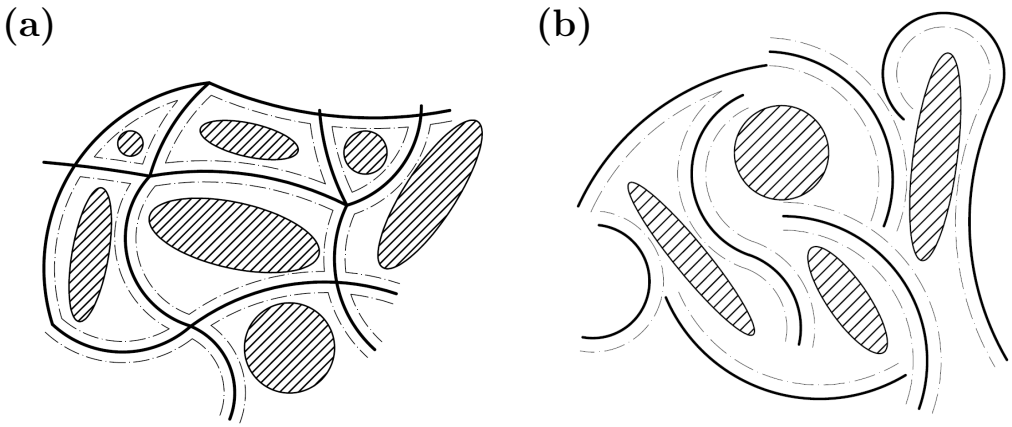

Figure 4.2: Two dimensional schematic of the free-volume holes for: (a) cross-linked; and (b) entangled polymer networks. The free-volume holes are represented by hatched ellipses and circles, the polymeric chains are shown as black lines, and the dashed dots are the bounded volume of each polymer chain.

In the following, a new methodology is developed to quantify the free-volume distribution and its evolution from atomistic simulations of polymeric networks. This methodology also provides a tool to validate the simulation results by direct comparison with PALS experimental measurements from real polymeric materials [28, 95]. Several examples of these comparisons are shown in Chapter 5, and Chapter 6. This tool is publicly available as an open-source software on Github [107].

4.3.1 Free-Volume holes in cross-linked networks

To start the quantification process, first, the volumes within the cross-linked part of the network are determined. This is achieved by a geometry-aware graph algorithm that searches through the network to find the volumes confined between the cross-linked chains. To find each free-volume hole, first, a triplet of consecutively bonded super-atoms is randomly chosen (c.f. $\widehat{ABC}$ as shown in Figure 4.3(a)). The shortest path of connected supper-atoms from super-atom A to super-atom C that does not pass through super-atom B is then identified and it along with the randomly selected triplet are designated as a closed loop of connected super-atoms, as shown in Figure 4.3(b). This process is repeated for all available triplets of super-atoms until all the closed loops in the network have been found. Each loop bounds a polygonal surface inside the network. These surfaces create envelopes that wrap around the free-volume holes inside the simulation cell. In order to quantify these volumes, the largest ellipsoids inside each wrap of polymer chains is fitted, as shown in Figure 4.3(c). Since this algorithm finds the shortest closed surfaces formed by polymer chains, it can automatically detect necking or openings in the microstructure and merges or splits these neighboring holes accordingly, as shown schematically in Figure 4.4.

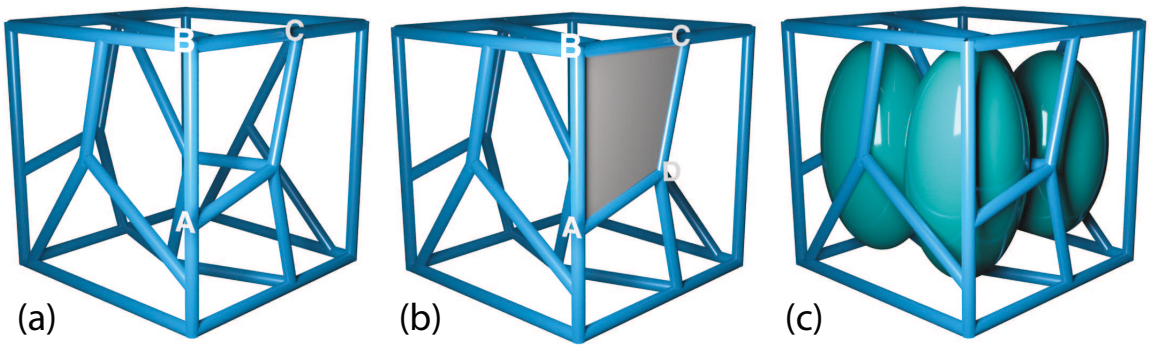

Figure 4.3: Detecting free-volume holes in a cross-linked network: (a) a random triplet of connected super-atoms is chosen (e.g. ABC), (b) the shortest path from super-atom A to super-atom C that does not pass through super-atom B is determined to define a closed loop polygonal plane; (c) the largest possible ellipsoid is then fitted in the confined volumes between the connected polygonal planes.

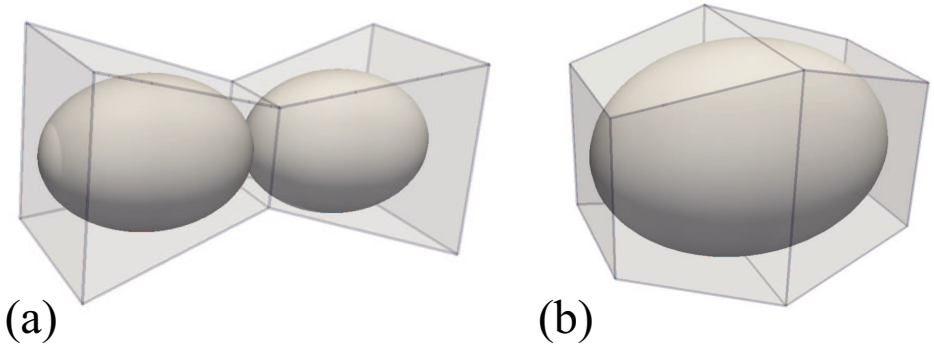

Figure 4.4: Schematics of splitting and merging free-volume holes in a cross-linked network: (a) a tight necking splits the volumes; and (b) a wide opening leads to merging volumes.

4.3.2 Free-Volume holes in entangled networks

One way to think about quantifying the free-volume holes in a cluster of molecules is to think about the share of each atom from the entire volume of the system. The systematic way of calculating the volumes of each node in a spatial system is to create a Voronoi diagram of the system using the Delaunay tessellation algorithms [108], as shown in Figure 4.5. A Delaunay tetrahedron is a tetrahedron composed of four atoms such that no other atom in the system is inside its circumsphere. Therefore,

each tetrahedron is an isolated volume whose volume belongs only to the atoms at its corners. A share of the tetrahedron volume is assigned to each corner atom by dividing its volume into four parts according to the location of its center of geometry. Thus, the volume that each atom occupies in the system can be calculated by a summation over all the of volumes of each node from the tetrahedrons containing the node.

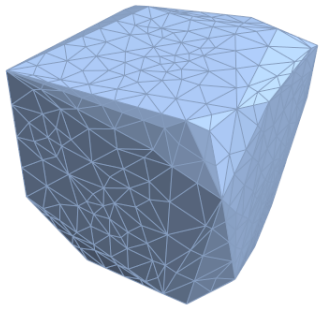

Figure 4.5: A 3D triangulation of microstructure

Here, the free-volume holes between atoms are calculated by merging the neighboring tetrahedrons such that the merged volume can fit a larger sphere at its center of geometry than the tetrahedrons. To do that, each tetrahedron will be tested for merging with its neighboring tetrahedrons. The minimum distance of the center of geometry of the created volume to the surface of each super-atom is calculated. If the distance of the created volume is larger than the radius of the spheres in both tetrahedrons, then the two tetrahedrons will be merged. Otherwise, two other neighboring tetrahedron will be tested. This process continues to find all possible volumes in the system.

As a simple rule, volumes with wider spacing between their corners will accommodate a larger sphere than one with tightly spaced corners. Therefore, the following guideline is designed to speed up the analyses and avoid checking each tetrahedron with its four neighboring tetrahedrons in the merging process.

- If the center of geometry of a tetrahedron is inside of one of the spheres of its corners atoms, the tetrahedron is too small to contribute to the free-volume of the system. Therefore, it has to be filtered out of the calculations.

- Two neighboring tetrahedrons create a low-intensity energy field if they merge through their largest plains. Otherwise, the merged volume will have a closed-pack of atoms (Figure 4.6).

- If the lines connecting the center of geometry of the tetrahedrons to the center of merging planes form a sharp angle, the resulting volume will be distorted and make a higher energy density field (Figure 4.7).

It should be noted that an ellipsoid provides the best fit for the general cavity shape over all other basic geometrical shapes [105, 109]. Thus, for a highly irregular highly irregular free-volume hole, an ellipsoid is the best representation of the random set of points in three dimensional space [109]. Thus, after all the volumes are created in the system, an ellipsoid is fitted inside each volume to provide a quantitative measure of that volume. These ellipsoids are used to extract data such as aspect ratio and volume of holes. However, given the quantum state of positron is a sphere, the radii that are used for comparison with PALS experiments are the radii of the spheres fit in the center of each ellipsoid.

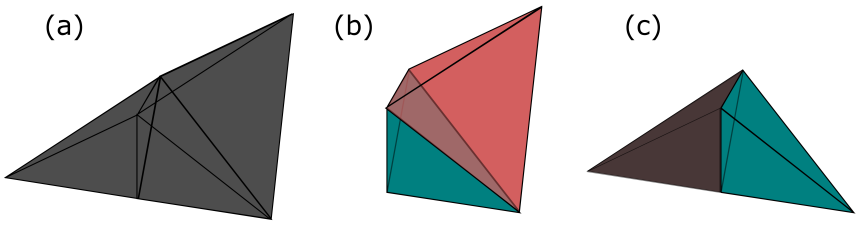

Figure 4.6: (a) A system of three tetrahedrons; (b) merging through the largest planes; (c) merging through the smaller plane.

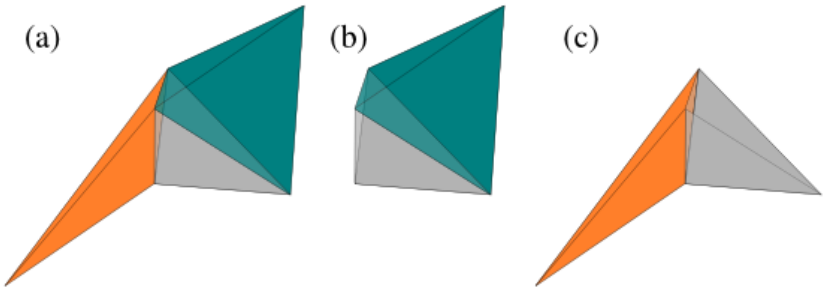

Figure 4.7: (a) A system of three tetrahedrons; (b) merging through the planes forming wide angle; (c) merging through the planes forming sharp angle.

In the following chapters, free-volume hole distributions calculated from coarse-grained simulations at different temperatures, pressures, and under active deformation are compared to those measured from PALS experiments.

Chapter 5

Correlating the Free-Volume Holes Distribution to the Glass Transition Temperature of Polymers

5.1 Introduction

The glass transition temperature, T_g, is one of the most important properties of any epoxy system as it dictates the service temperature, and the application of the epoxy. The glass transition temperature is the temperature at which the polymer transitions from a glassy phase to a soft rubbery state. The fundamental mechanisms underlying this transition from a glassy material to a rubbery material has been continuously a subject of debates for years. Viscous flow inside a polymer network, as a thermally activated process, has an important role in describing the underlying mechanism of this transition [110–112]. Given adequate time, viscous flow takes place by localized rearrangement of a single chain over local potential barriers. This rearrangement, though

not an irreversible process, severely retards the recoverable elastic deformation of the system [110, 111]. Irreversibility, thus, occurs when these local rearrangements take place in many local regions. As the temperature decreases, the relaxing molecules tend to form packs of molecules in the amorphous states of the polymer, which will give rise to a distribution of local barrier heights. The rise in the local barrier heights will hinder the viscous flow of the molecules in the system, such that when the temperature approaches the glass transition temperature, the viscous flow can no longer occur at an observable rate. This is where the glass transition is observed. However, the possibility of viscous rearrangements involving the sites with lower barriers still exists, which will give rise to a secondary relaxation, if the temperature holds below the glass transition temperature [110, 111].

On the other hand, the viscous flow, and subsequently the rubbery-to-glassy transition, mainly occurs due to the movement of large segments of polymer in the system [10].Thus, it is expected that the glass transition temperature is dependent on the flexibility of the polymer backbone as well as the strength of intermolecular forces. For instance, when intermolecular interaction forces are strong then the attractive force between molecules becomes stronger, which hinders the relative rearrangement of polymer chains. Therefore, polymers with low chain stiffness (i.e. having lower barrier), have a lower T_g [113, 114]. It is also observed that insertion of an aromatic ring in the backbone, that strengthens the rigidity of the backbone of the polymer chains, leads to a substantial increase in T_g [9, 115]. On the other hand, molecules with higher molecular weight are bulkier with lower mobility. Thus, for a given polymer, the glass transition temperature increases with the average molecular weight [113–115].

In addition, cross-linking can increase the glass transition temperature of a polymer since at high degrees of cross-linking the linkage between segments are spaced so closely, which severely impedes the mobility of large segments that are engaged in the

glass-rubber motion [10]. However, if the average lengths of the segments of between cross-linker is longer than the length required to initiate large segmental movement of polymer around its backbone, the cross-linking does not alter the glass transition temperature significantly [10, 116, 117].

Despite the success of the free-volume theory, which was developed decades ago, in explaining the intrinsic nature of viscous displacements in polymers, very limited experimental information regarding the free-volume holes and their spatial fluctuations are available. It was only a decade ago when PALS experiments provided a sophisticated approach to extract useful information about the distribution of free-volume holes. Recently, the temperature and pressure dependence of free-volume hole distribution of epoxies were measured using PALS experiment [26–28, 94]. Observations showed that there is a direct correlation between the distribution of free-volume holes and the temperature/pressure response of polymers. In addition, the glass transition temperature calculated from the average radius of free-volume holes was shown to be in good agreement with those measured from experiments such as differential scanning calorimetry (DSC)[23]. Nevertheless, one of the short-comings of PALS experiments is that they are incapable of measuring the local distribution of free-volume holes, which makes it impossible to correlate free-volume hole distributions to local phenomena such as unrecoverable plastic deformation, or crack nucleation.

In this chapter, the pressure and temperature dependence of free-volume holes in the epoxy systems are shown from the coarse-grained MD simulations of epoxies. Then, for verification purposes, several comparisons between the calculated free-volume hole distributions with those measured from PALS experiments on similar type of epoxy under identical condition are made. Finally, a new thermal evolution model for free-volume holes is proposed to better predict the glass transition temperature of the epoxy system for any given initial distribution of free-volume holes.

5.2 Temperature Dependence of Free-Volume Hole Distribution

5.2.1 Temperature effects

The relaxed coarse-grained microstructure and the distribution of free-volume holes at room temperature for a polymeric network constructed from DGEBA prepolymers having an initial length of 5 monomers and a degree of cross-linking of 85%, are shown in Figure 5.1. The relaxed microstructure has a density of 1.15 g·cm^{-3}, which is in agreement with the experimentally measured density of 1.13 g·cm^{-3} [27].

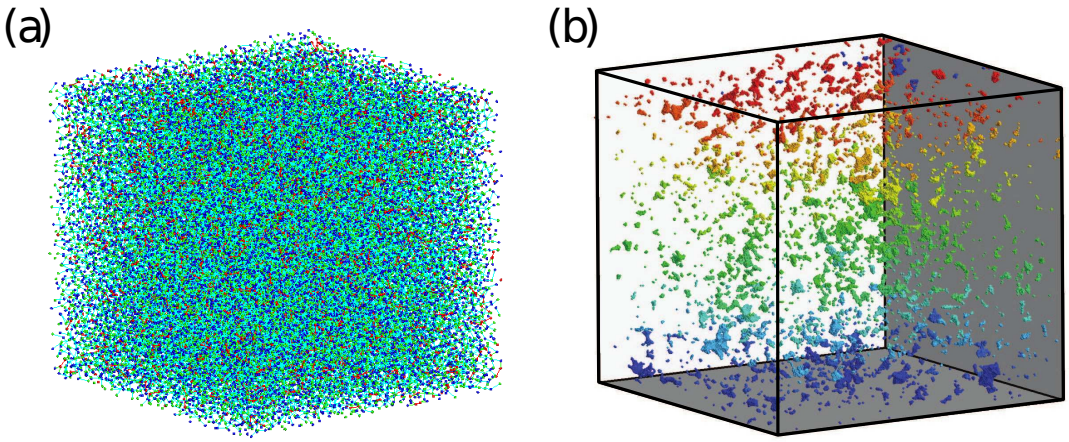

Figure 5.1: (a) Coarse-grained microstructure; and (b) distribution of the free-volume holes at room temperature. The colors in (b) are only to help for visualization.

The glass transition temperature is calculated by cooling down the temperature of the relaxed microstructure from 550 K to 150 K in 4×10^6 time-steps with a cooling rate of 2.75×10^8 K s^{-1}. The predicted specific volume, ρ^{-1}, versus temperature, T, for this simulation is shown in Figure 5.2(a) along with the average radius of free-volume holes as a function of temperature. The predicted glass transition temperature of 63°C is in agreement with the one measured experimentally for the same epoxy [27]. The crossover temperatures, shown as $\boxed{1}$, $\boxed{2}$, and $\boxed{3}$ in Figure 5.2, between these

stages are considered to denote transitions between two coexisting phases with different structures such as supercooled and glassy regions, or glass and liquid/rubber regions [9, 118]. A high-temperature transition is also observed in free-volume versus temperature curve of the epoxies. This transition mainly originates from the annihilation mechanism of the o-Ps. In fact, the o-Ps annihilation time is a function of the energy density of the environment. The increasing size of the free-volume hole does not significantly alter the electron density of the free-volume, therefore the annihilation time and the resulting free-volume hole size will remain constant. Because the computationally obtained distribution of the free-volume holes is calculated by analyzing the topology of polymer networks, the temperature dependences of these free-volume holes does not show the high-temperature crossover temperature, as shown in Figure 5.2(a) [100–102, 104]. It is also shown that the average radius of free-volume holes lie along the specific volume versus temperature curve. Similar observations have also been made from PALS experiments, where the glass transition temperature of the material was measured from the average radius of free-volume holes versus temperature curves [26, 27]. In the two regions where the temperature is much lower or much higher than the glass transition temperature, the volumetric changes are mainly constrained by the movement of the surrounding polymer chains. This leads to comparatively tighter distribution of free-volume hole's radii at very low, or high temperatures as shown in Figure 5.2(b). It is also shown in Figure 5.2(b) that the distribution of free-volume hole's radii widens at temperatures close to the glass transition temperature of the epoxy [6].

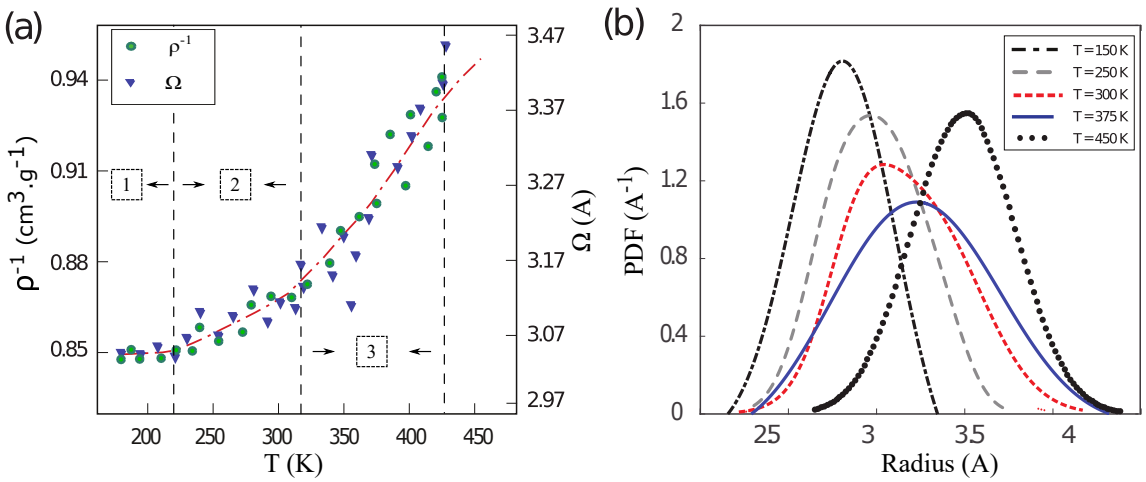

Figure 5.2: (a) Specific density and average free-volume holes radius as a function of temperature. (b) Probability density function of free-volume holes' radii of the microstructure at different temperatures.

5.2.2 Pressure effects

The probability density function (PDF) of the free-volume holes radii at different pressures as predicted from the current simulations are shown in Figure 5.3. In addition, those measured from PALS measurements at the same pressures [6] are also shown for comparison. A qualitative agreement is observed between the simulation predictions and experiments, however, it is clear that the average size of free-volume holes predicted from the current simulations are consistently larger than those measured experimentally. This can be attributed to the fact that the smaller free-volume holes between atoms in a atomic structures are not preserved in a coarse-grained system. Therefore, it is expected that the average radius of free-volume holes are shifted to the right.

5.2.3 Effects of different microstructural features

A number of simulations were performed for different length of DGEBA prepolymers for a given degree of cross-linking, and for different degrees of cross-linking for a given

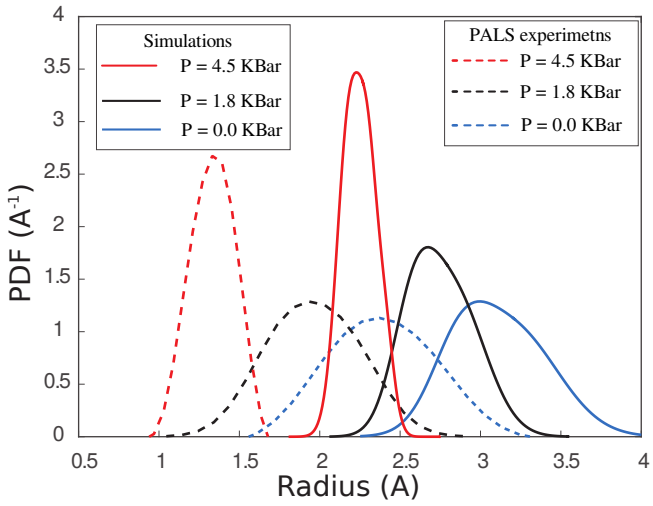

Figure 5.3: Probability density function of free-volume holes radii of the relaxed microstructure at different pressures. Data from PALS measurements [6] are also shown for comparison.

lengths of DGEBA prepolymers in order to investigate the effect of microstructural features on the predicted free-volume hole distribution and glass transition temperature of the epoxy. For this purpose, first, three cross-linked networks are created by curing DGEBA chains with an initial length of 5 monomers to three different degrees of cross-linking of 75%, 85%, and 95%. Second, three other cross-linked networks having a degree of cross-linking of 85% are created with three different DGEBA prepolymers with length of 2, 4, and 6 monomers. The average radius of free-volume holes versus temperature for all these simulations are shown in Figure 5.4(a). As summarized in Figure 5.4(b), there is a strong correlation between the predicted glass transition temperature and the average radius of free-volume holes and the initial microstructure. The mobility of chains is lower in networks having smaller free-volume holes, thus, these epoxies exhibit a glassier behavior, and the glass transition occurs at higher temperatures.

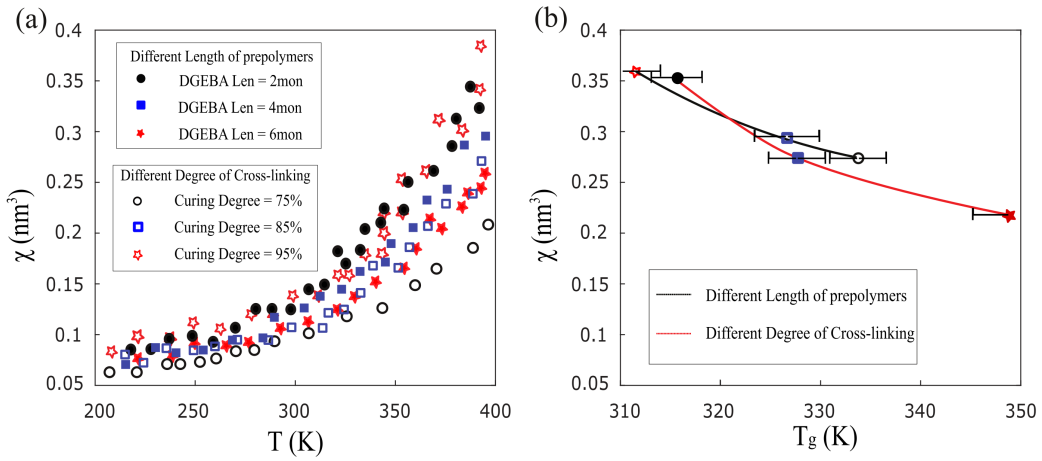

Figure 5.4: (a) The average volume of the free-volume holes as a function of temperature for different degrees of cross-linking, and initial length of DGEBA prepolymers. (b) Correlation between average volume of free-volume holes and glass transition temperature of the epoxy.

5.3 Microstructural-Based Glass Transition Temperature Predictive Model

As discussed in the previous section, free-volume holes play a crucial role in determining the glass transition temperature of the epoxy. As such, in this section the distribution of free-volume holes is incorporated into a model to predict the glass transition temperature of epoxy polymers. To that end, the volume of the entire simulation cell is divided into a solid volume, corresponding to the total volume of all polymer chains, V_{chain}, and the total free-volume, V_{free} [119]. The free-volume holes undergo significant changes in their total volume with varying temperature. On the contrary, temperature will have a negligible effect on the solid chains volume [119]. Furthermore, it is also common that the free-volume holes are classified as "frozen" or "mobile" [120]. Here, an evolution model for one free-volume hole is proposed to capture the volumetric change of the free-volume hole as function of change in temperature and assumed to follow a quad-linear relationship with temperature, as

shown schematically in Figure 5.5, in a similar manner to the evolution of the average radius of the free-volume holes with temperature (as discussed in Section 5.2.2 and observed from PALS measurements [27]). The mathematical representation of this model takes the form:

$$\begin{aligned}\Delta r = \Delta T\{\, \alpha_l \mathcal{H}(r_l - r) + \alpha_f \mathcal{H}\left((r - r_l) \times (r - r_{tg})\right) + \\ \alpha_m \mathcal{H}\left((r - r_m) \times (r_h - r)\right) + \alpha_h\, \mathcal{H}(r - r_h)\}\end{aligned} \tag{5.1}$$

where α_l, α_f, α_m, and α_h are the slopes of the four different stages on the radius versus temperature curve, and r_l, r_{tg}, and r_h are the radii at which the slope of the curve changes, as indicated in Figure 5.5. Given any distribution of free-volume holes for a polymer, the temporal evolution of the average radius of free-volume holes can be measured by calculating the change in radius of the individual free-volume holes according to the change in temperature using equation (5.1). The values for the different α's and r's should then be optimized such that the average radius of free-volume holes as computed from equation (5.1) would be equal the real value for the polymer. As a first example of the proposed model, the histogram distribution of free-volume holes as predicted at room temperature, and the predicted average volume of free-volume holes, χ, as a function of temperature, for a polymeric network constructed from DGEBA prepolymers having an initial length of 5 monomers and a degree of cross-linking of 85% are shown in Figure 5.6. The individual bars of the histogram are treated as representative for individual free-volume holes. The parameters in equation (5.1) are then optimized such that the evolution of these individual free-volumes holes lead to average free-volume holes at different temperatures that match those predicted from simulations. The initial values of the α's, r_l, and r_h are directly taken from the simulated curve shown in Figure 5.6(b). The initial value of r_{tg} is assumed to be the radius, at which the frozen fraction of the free-volume holes

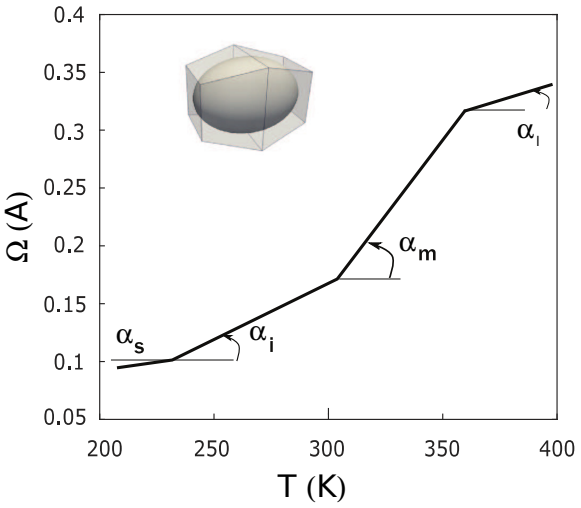

Figure 5.5: Schematic of the thermal evolution model proposed for a single free-volume hole.

Caibration	α_l	r_l	α_f	r_{tg}	α_m	r_h	α_h
Simulation	0.0007	2.1968	0.0040	3.1815	0.0147	6.6792	0.0012
Experiment	0.0008	2.1851	0.0050	2.6050	0.0121	4.5700	0.0010

Table 5.1: Calibrated variable for the thermal evolution model (Eq 5.1)

is equal to the experimentally measured value of frozen fraction of free-volume holes [120]. The optimized values of the α's and r's in equation (5.1) that would best fit the simulated χ versus T relationship are listed in Table 5.1, and the predicted average radius of free-volume holes versus temperature from equation (5.1) is also shown in Figure 5.6(b). It is clear that there is a good agreement between the model and simulation results. The thermal expansion coefficients of calculated from the model are also in good agreement with those calculated from the simulation.

The calibrated evolution model, equation (5.1), with the optimized parameters in Table 5.1 is used to predict the average volume of free-volume holes versus temperature curves for the same epoxy with different degrees of cross-linking and lengths of prepolymers. The average volume of free-volume holes versus temperature as pre-

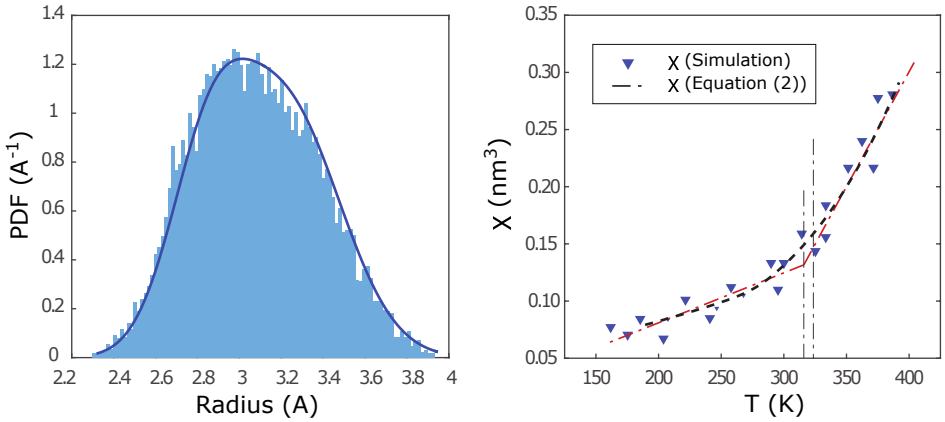

Figure 5.6: (a) Probability density function of free-volume holes radii at room temperature. (b) Comparison between the average volume of free-volume holes, χ, as calculated from the model, and predicted from the simulations.

dicted from equation (5.1) with the predicted initial free-volume holes at room temperature from the simulations of the different cases are shown in Figure 5.7. Furthermore, the results as predicted from the simulations are also included for comparison. It is clear that the analytical model prediction of the glass transition temperature of the polymer in each case matches well those predicted from the simulations for the different degrees of cross-linking and lengths of DGEBA prepolymers.

In another example, equation (5.1) was also optimized according to PALS measurements to see if it can reasonably predict the glass transition temperature of the system given the initial distribution of free-volume holes. First, a large number of free-volumes holes were sampled over the free-volume holes radii PDF at 40 °C from PALS experiments as shown in Figure 5.8(a) [6]. These along with the average volume of holes as a function of temperature (shown in Figure 5.8(c)) are used to optimize the parameters in equation (5.1), and the optimized values are listed in Table 5.1. The PDF of the free-volume hole radii at 100 °C (Figure 5.8(b)) was then used to test the model. The predicted curves of the average volume of free-volume holes versus temperature are plotted in Figure 5.8(c). The predicted curves show a good agreement with the experimentally measured curve, indicating that the model can successfully capture the evolution of free-volume holes as a function of temperature.

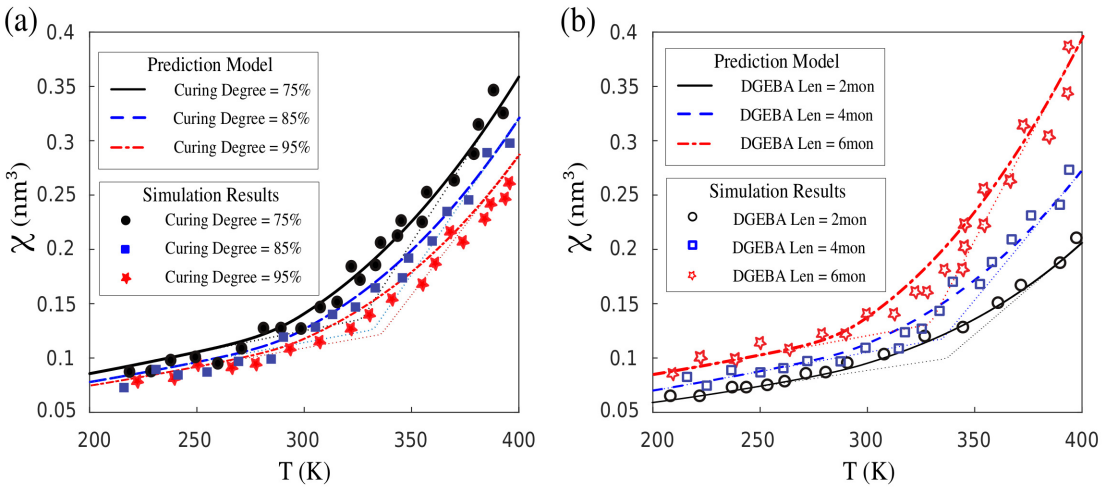

Figure 5.7: Comparison between the average volume of the free-volume holes at different temperatures as calculated from model and predicted from the simulations for epoxies having: (a) different degree of cross-linking; and (b) different length of prepolymers.

The above results suggest that equation (5.1) can be calibrated given an initial distribution of free-volume holes and the evolution of the average free-volume holes as a function of temperature for a given degree of cross-linking and length of prepolymers, then effectively used to predict accurately the glass transition temperature for another polymeric network having the same chemical composition but different degrees of cross-linking or length of prepolymers. It should be noted that the optimized values are function of cooling rate. Therefore, it can only be utilized when the glass transition temperature is required at the same cooling rate as the model is calibrated too.

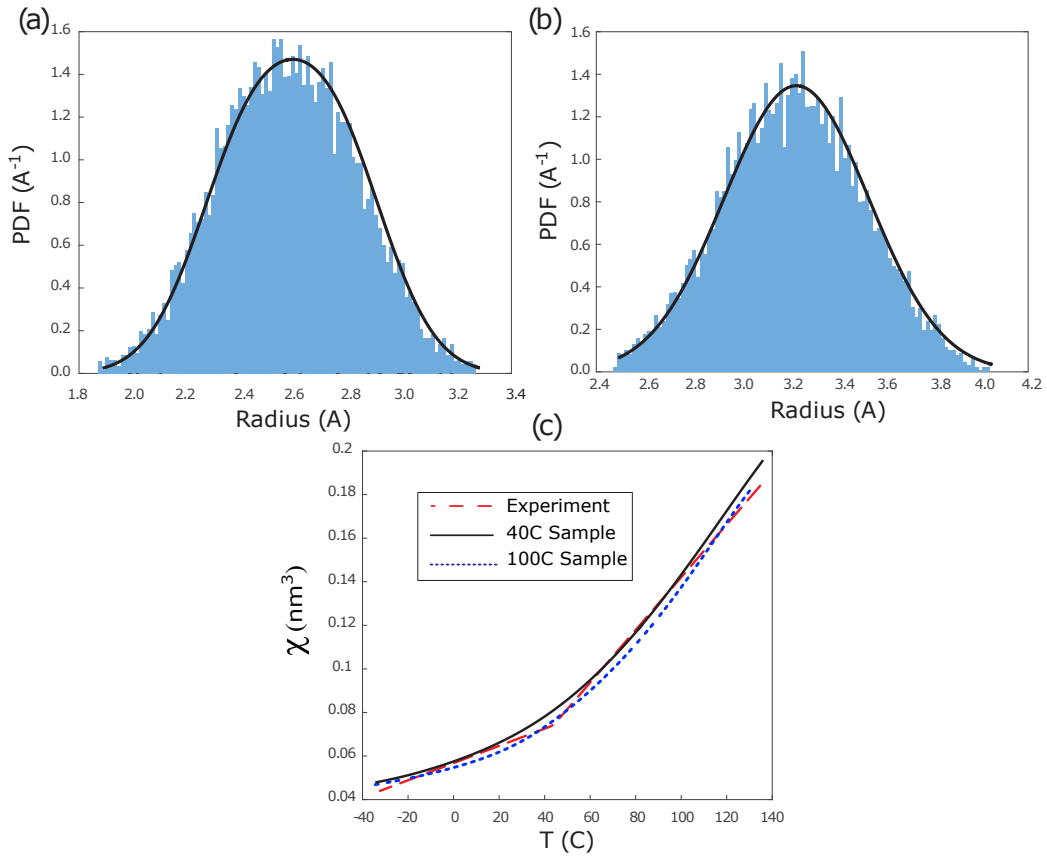

Figure 5.8: (a) Probability density function of the free-volume holes radii at $T = 40\,^{\circ}\mathrm{C}$. (b) Probability density function of the free-volume holes radii at $T = 100\,^{\circ}\mathrm{C}$. (c) The experimentally measured, calibration at $T = 40\,^{\circ}\mathrm{C}$, and computed at $T = 100\,^{\circ}\mathrm{C}$ curves of the average radius of free-volume holes versus temperature.

5.4 Summary and Conclusions

In this chapter, the free-volume algorithm discussed in Chapter 4 is utilized to calculate free-volume hole distributions of several highly cross-linked DGEBA epoxies at various pressures, and temperatures. These distributions are compared to their counterparts measured from the PALS experiments under identical conditions. The algorithm is shown to provide comparable results with PALS experiment results at different temperatures and pressures. The thermal behavior of an individual free-volume is then characterized using a model that is calibrated to mimic the accurate average behavior of free-volume holes of a benchmark simulation. The calibrated model was employed to predict the glass transition temperature of different microstructures by evolving every free-volume hole via the model. Comparison between the predicted glass transition temperatures and the simulated glass transition temperatures for different degrees of cross-linking and lengths of prepolymers implies that this model is capable of successfully predicting the glass transition temperature of the material using only a single PDF of the free-volume holes radii of each microstructure. To further investigate this observation, the free-volume holes radii PDFs measured in PALS experiment for an epoxy polymer at two different temperatures were also used to sample two sets of free-volume holes. The free-volume holes sampled over the PDF at 40 °C was employed to calibrate the model for the material. Then, the model was tested using the free-volume holes sampled over the PDF at 100 °C to predict the glass transition temperature of the material. The comparison between the predicted curve and calibrated curve shows a tremendous agreement, proving that the model is capable of predicting the thermal evolution of free-volume holes in an epoxy polymer. The proposed model can be utilized to effectively optimize the design of polymeric systems on the basis of glass-transition temperature, degree of cross-linking, and average length of prepolymers.

Chapter 6

Correlating the Free-Volume Hole Distribution to the Elasto-Plastic Properties of Polymers

6.1 Introduction

The high strength and adhesion of highly cross-linked polymer networks to a solid surface are the most important properties of these materials that are used extensively as resins in the aerospace composite materials. Therefore, understanding the dominant mechanisms of deformation, and adhesion of these materials is of a crucial importance. Mechanical deformation of epoxy polymers has been studied for years, and the basic features of the stress-strain curves are well-known [12–14]. These material exhibit an elastic response where the strain and stress are linearly proportional. At slightly larger strains, when inter-molecular barriers to segmental rearrangements are overcome, yielding occurs. After yield the material undergoes strain softening, a reduction in stress to a level corresponding to plastic flow. At higher strains, when strain hardening happens, the stress increases again when the chain molecules orient

around the direction of loading. The balance between strain softening and hardening is critical in determining material properties such as strength and toughness. When strain localization is suppressed the material has ductile tendencies rather than brittle deformation. The strain localization process is highly controlled by the segmental mobility of the polymer chains, which are a strong function of the local energy barrier for orientations of chains [9, 10].

Despite all the experimental and modeling advances reported in the literature, the molecular origins of these properties are not well understood. In comparison to crystalline solids where theories based on dislocation motion have succeeded in illuminating the mechanisms controlling the plasticity, lack of long-range order within polymeric systems precludes the use of similar theories. However, there are theoretical models to explain the plasticity of polymeric systems on the notion of small localized transformations within the material in response to an applied stress. The model proposed by Eyring [15] postulates that the energy barriers of these local transformations alternate according to the applied stress. This model fails to describe the behavior of the material over a wide range of temperatures and strain-rates due to the lack of incorporation of the underlying molecular process [16]. In another theory, it is assumed that the applied stress alters the energy level associated with the rotational isomeric state of a dihedral angle along the chain [16, 24, 121]. This model considers the barrier to be due to the resistance to molecular segmental rotation posed by intramolecular and intermolecular interactions of the chain with the surrounding material [122]. However, this model also fails to describe the origin of plastic deformation of the epoxies at high strain rates [121].

On the other hand, further investigation of these theories via experimental techniques is very hard due to the difficulties associated with collecting conformation-specific data, especially during active deformation. Only recently, experiments have demonstrated transient features of the molecular response during the active deforma-

tion of polymers. Nuclear Magnetic Resonance spectroscopy (NMR) experiments on Nylon have demonstrated stress-induced mobility within the amorphous regions [53]. It is also observed that the mobility of the monomers under active deformation will be different from that in the undeformed case due to the uniaxial extension [53, 123]. The trivial contribution to this mobility results from the constant rate of the affine extension of the polymer chains. The particles throughout the sample are accordingly convected with some local velocity, which masks the polymer-specific effects of the deformation on the segmental mobility. It is also observed that the translational mobility of the chains below the yield point changes negligibly, while changes occur in the post-yield region where an acceleration of the parallel diffusion of chains inside the sample is observed by more than one order of magnitude. This change in mobility is also observed in terms of increase in the internal dynamic behavior, i.e. the dihedral angle transition rate, under the influence of a deformation from coarse-grained MD simulations [12, 53].

Another important aspect in characterizing plastic deformation of an epoxy polymer is the curing process, and microstructural effects such as density of entanglement, the average length of cross-linking and etc. Tsige et al. [19] studied the effect of curing agent functionality on the plastic deformation and adhesive properties of cross-linked polymers. They showed that the plateau regime in the stress-strain curve is highly dependent on the functionality of the curing agents, as it was reported that the higher the functionality of the agents, the shorter the plateau is. It was also observed that strain range of the plateau regime is reduced with the increase of the density of cross-linker, and also increase of the functionality of curing agents. This is because the bond density is larger at larger functionality, and thus more bonds are stressed. Therefore, the work to failure decreases with increase in functionality. On the other hand, it was also found that the number of chemical bonds on the solid surface controls the type of failure at the interface. Increasing the number of chemical bonds on

the surface results in a cohesive failure [19, 88]. It has been also shown that bond breaking starts in regions with a low local mobility of chains [19]. As it was previously discussed in Chapter 5, the local mobility of polymer chains directly depends on the free-volume hole distribution in a polymer network. It was also shown that change in microstructural feature of an epoxy such as functionality of curing agents, or length of cross-linking alters the glass transition temperature of the polymer. Given that plasticity is usually associated with the local mobility of chains in the system, the main question is whether there is a similar correlation between plastic deformation of an epoxy and the free-volume distribution of the system.

In addition, perhaps the most interesting application of molecular simulations of polymers is to investigate the structural variation of resin around the fibers in PMCs. Especially, with the development of coarse-grained models, which have pushed the length scale of molecular simulation far beyond the scope of conventional detailed atomic models, there is a great opportunity for investigating the properties of the matrix of PMCs using these techniques. In addition, given that damage in PMC materials is a multi-scale problem in nature, the information from these low scale simulations can be upscaled to higher length scale models, such as finite element models, for better prediction of the strength and damage prediction of PMCs.

Structural variations of the matrix around the fibers and nanoparticles in nanocomposite materials have been studied using both experimental and numerical techniques [124–133]. Having a large number of fibers in a PMC structure introduces an enormous amount of interfacial surface, which dramatically alters the conformations of polymer chains in their vicinity [134]. It has been observed that the interfacial contact perturbs the structure of its surrounding resin (e.g. density, chain orientation, arrangement, and stretching or wrapping around the fibers) [130, 135], and the dynamics (e.g. slower dynamics of the chains in the vicinity of the fiber and formation of glassy polymer layers around the fiber) of the polymer [128, 129]. This region of

altered polymer properties is commonly called the interphase.

Manipulation of the interphase properties is perhaps the most important step in creating a better composite. However, a well-defined manipulation of the interphase properties requires a thorough understanding of structure-property relationships in PMCs. This includes knowledge of the correlation between the structure and properties of the interphase at a quantitative level. Despite numerous experimental [136–138] and theoretical [139–141] studies, an accurate understanding of these relationships is still missing. A possible explanation for this is perhaps the inconsistency and discrepancy between different experimental results. For instance, some experiments suggest a structural variation around the fibers and nanoparticles due to lack of mobility of polymer chains around the fibers [134, 138, 142, 143], while other experiments report a negligible difference in the properties of the matrix between the interphase and bulk [136]. This discrepancy in the experimental results emphasizes the need for information from model that account for the conformation of polymer chains around the fibers.

In this chapter, first, stress-strain relation of a lightly cross-linked DGEBA above the glass transition temperature is calculated. Then, several cross-linked DGEBA system are cured at different conditions to investigate the effects of free-volume holes on the strength of epoxy systems. To study the structural variations of the matrix in PMCs, a large matrix is cured in the presence of two fibers to calculate the variation of free-volume as a function of distance from fibers. Using this distribution, a finite element framework is designed to model a large size PMC with a matrix having localized material properties. Finally, to show the importance of utilizing position-based properties on the prediction of strength and damage evolution in PMCs, FEM simulations are compared to damage of identical PMCs having a homogeneous matrix.

6.2 The Elasto-Plastic Response of the Epoxy

Here, the stress-strain relation of a loosely cross-linked DGEBA system is examined. In the current simulations, an initial blend of DGEBA prepolymers, DAB, and DDH reactive curing agents with a ratio of 5:1:4 is introduced into a cubical simulation cell having an edge length of 70 nm. The DGEBA prepolymers used here have a random number of monomers with an average length of 5 monomers per prepolymer. Given that DDH agents can only form two chemical bonds with DGEBA monomers, the resulting cured network will have long segments between DAB hardeners in the system. Therefore, the polymer chains can freely rotate around their backbone and move in large segments of chains during the deformation.

To mimic the bulk response of the material, periodic boundary conditions are imposed along all three directions. The molecules are modeled using the coarse-grained model discussed previously in Chapter 2. The initial system is a liquid mixture of the different molecules at a density of $1.16\,\mathrm{g\,cm^{-3}}$. The system is cured to a 85 % degree of cross-linking at 600 K using the curing algorithm discussed in Chapter 3, and relaxed at the simulation temperature of 450 K for one million time-steps. The system is under uni-axial tension with a strain rate of $10^5\,\mathrm{sec^{-1}}$. The deformation is applied by enlarging the volume of the simulation cell in the direction of the applied force according to the imposed strain rate. All the simulation parameters are those stated in Chapter 5, unless otherwise stated.

The strain and stress relationship of the network at 450 K along with the average radius of free-volume holes as a function of strain is shown in Figure 6.1. Three different behaviors are observed during deformation. At the beginning of the deformation, the material deforms elastically, with the stress linearly increasing with increasing strain. At this stage, the material can fully recover from the deformation to its initial state if the load is removed. On the other hand, it is also observed that the average radius of free-volume holes increases with increasing strain. In the second

region, material yields under deformation, and comply with the applied deformation by undergoing unrecoverable plastic deformation. It is observed that the radius of average free-volume holes remain constant upto 45 % strain, and slightly increases in size with increasing strain to a maximum size of 3.2Å. A similar qualitative trend is seen from PALS simulations of polymers under deformations, although the range of strain in the experiment is shorter than the current simulation [29].

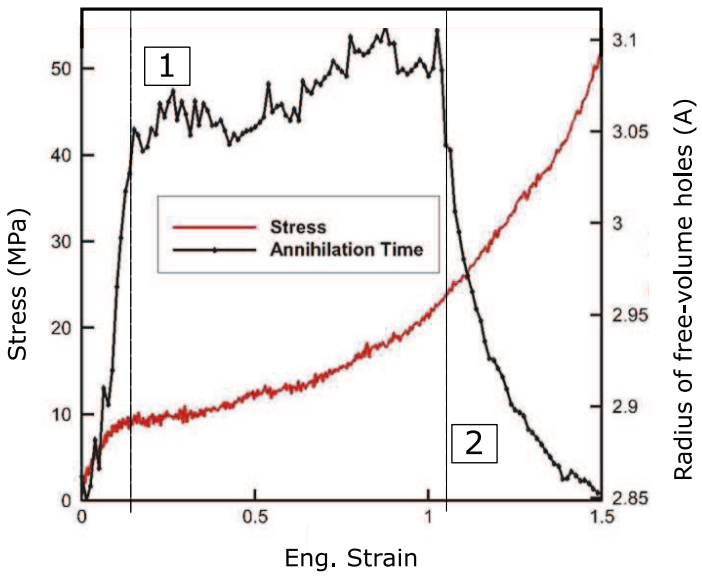

Figure 6.1: Stress-Strain relation of epoxy

From the current simulations the energy of the system is decomposed into energy terms associated with stretching bonds, bending angles, and turning dihedral angles as well as pair potential energy, as shown in Figure 6.2. It is seen that the bonds remain intact throughout the deformation upto the 95% strain, Figure 6.2(a). As the bonds start to pull taut, the point marked as 2 in Figure 6.1, radius of average free-volume holes decreases rapidly.

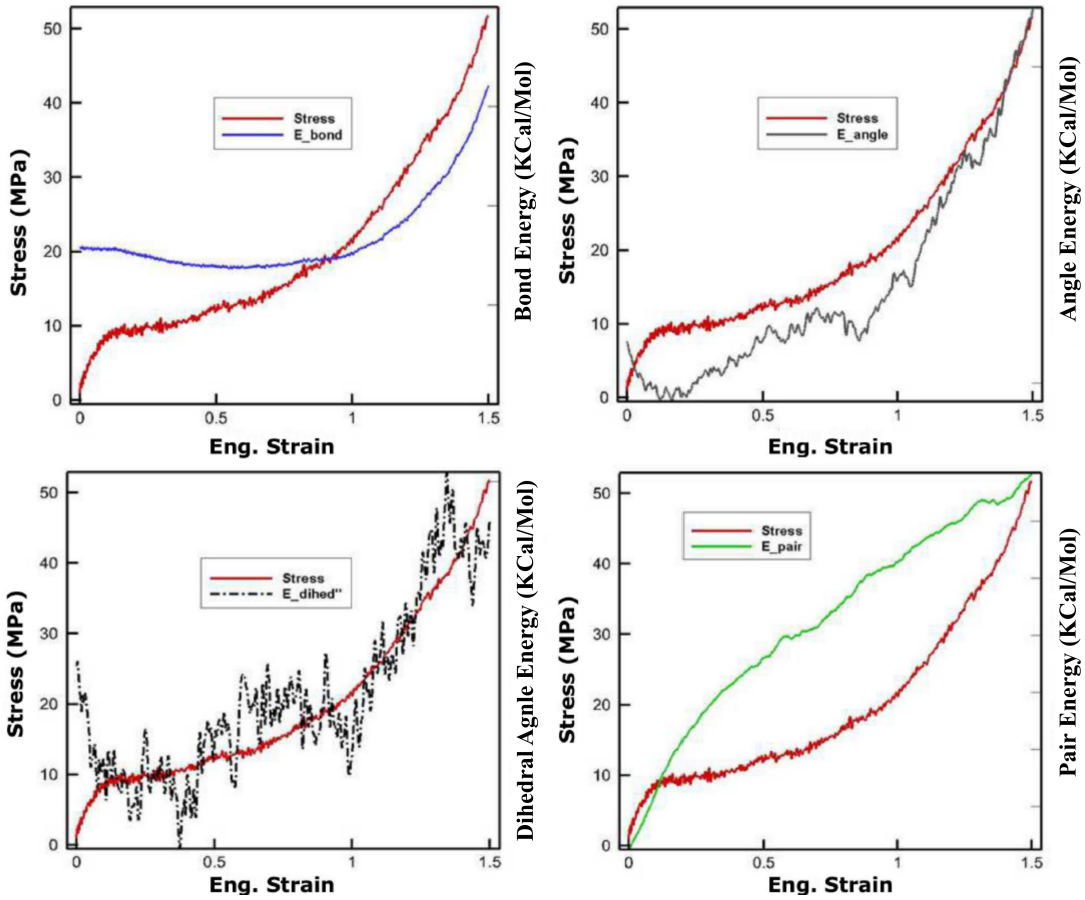

Figure 6.2: Evolution of energy of the system under active deformation in terms of energy of (a) bonds, (b) angles, (c) dihedral, and (d) pair potential

6.2.1 Simulations of the glassy response of the DGEBA epoxy

Here, in order to mimic the glassy response of the epoxy under deformation, a cross-linked network is created by randomly generating a mix of DGEBA prepolymers with an average length of 5 monomers per prepolymer, and DAB curing agents with the ratio of 2:1 in a cubical simulation cell having an edge length of 70 nm. DAB agents create up to four chemical bonds with DGEBA monomers. Given the ratio of 2:1 of curing agents in the initial melt, there are two active functional groups per DGEBA monomer in the system. Therefore, the resulting cured network is a highly cross-linked system with a short average length of segments between DAB cross-linkers.

This severely limits the roation of polymer segments around their backbone. Therefore, this system reflects a glassy response under deformation. Periodic boundary conditions are imposed along all directions to mimic the bulk properties of the epoxy network. The initial system is a liquid mixture of the different molecules at a density of $1.16\,\mathrm{g\,cm^{-3}}$. A similar curing process as described in Chapter 3 is employed to create a cross-linked network with a degree of cross-linking of 85 %. The system is relaxed using the NVE ensemble with the displacement of super-atoms are limited to 1 angstrom for 500,000 steps. Then, the glassy system is reached by a rapid temperature quenching the system to room temperature in one million time-steps at zero pressure. The system is relaxed at zero pressure and at room temperature using Nose-Hoover thermostat and barostat. The system is under uni-axial tension with a strain rate of $10^5\,\mathrm{sec^{-1}}$. Bond breaking takes place when a bonds stretches more than 12 % of its initial length. The simulation parameters are those used in Chapter 3 unless otherwise stated.

The strain-stress relationship of the network at room temperature along with the evolution of the average radius of free-volume holes, and associated energy of the system to the bonds, angles, and dihedral angles as a function of strain are shown in Figure 6.3. First, a quick comparison between the response of the loosely cross-linked and the highly cross-linked systems shows a stiffer response, as well as higher strength for the highly cross-linked system. It is also observed that failure occurs at comparatively lower strains in the highly cross-linked system. The change in energy of the system during deformation resembles the pattern that is observed during energetic hardening of loosely cross-linked system, implying that the bonds and angles are engaged in the predicted stiffness of the system from early stages of deformation. The ultimate stress of the simulation is subjective to the predefined length of bond breaking. However, the elastic modulus of the system is in the range of 133 MPa which is in the same order of magnitude of the experimentally measured elastic mod-

ulus of the epoxy [144–147].

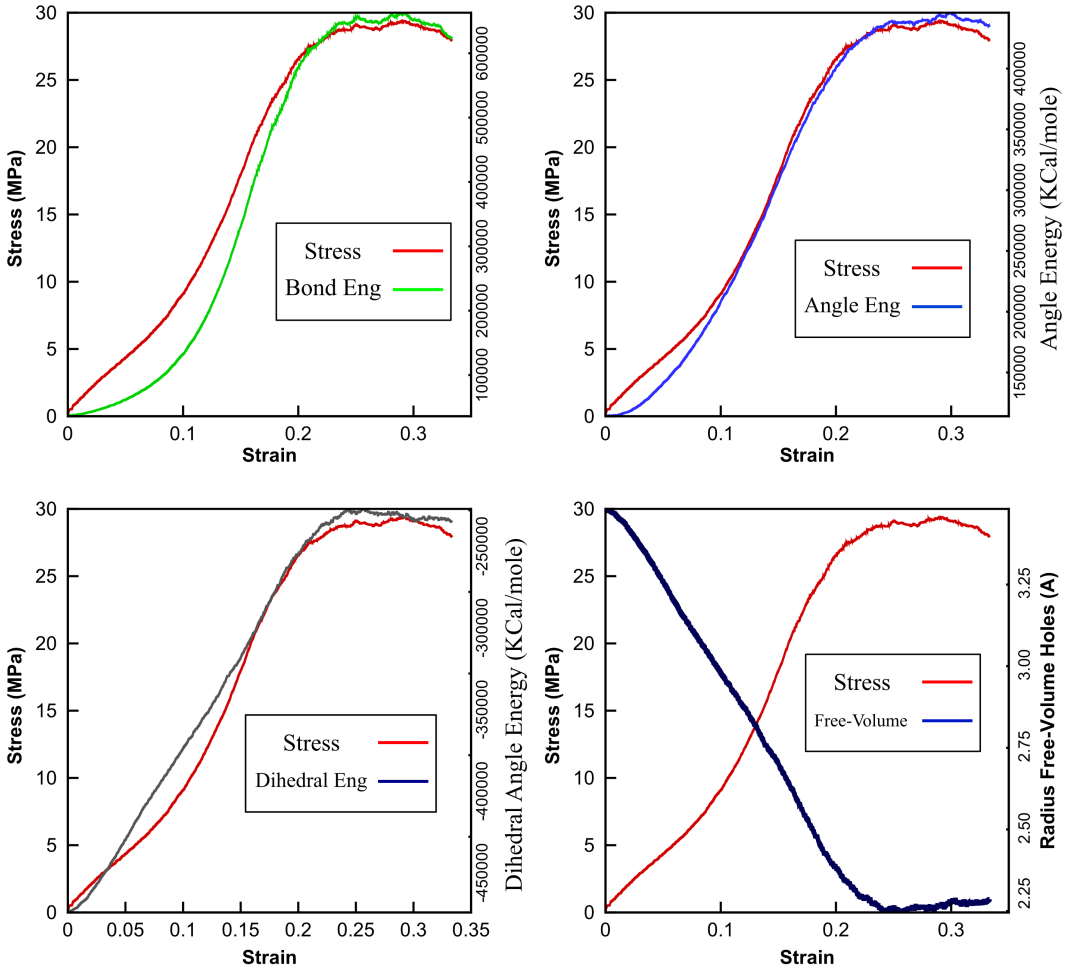

Figure 6.3: Stress-Strain curve along with evolution of (a) bond, (b) angle, (c) dihedral angle energy, and (d) average radius of free-volume holes as a function of strain

6.2.2 Effects of different microstructural features

A number of simulations were performed for different lengths of DGEBA prepolymers for a given degree of cross-linking, and for different degrees of cross-linking for a given lengths of DGEBA prepolymers in order to investigate the effect of microstructural features on the predicted free-volume hole distribution and elastoplastic properties

of the epoxy. For this purpose, first, four blends of DGEBA prepolymers and DAB agents are created having the initial DGEBA length of 3, 4, 5, and 6 monomers. Then, each mix is cured to the degrees of cross-linking of 35%, 50%, 75%, 85%, and 95%. The average radius of free-volume holes in each microstructure is then calculated. The correlation between degree of cross-linking and initial length of prepolymer with average radius free-volume holes are shown in Figure 6.4. It is observed that longer length of prepolymers and lower degree of cross-linking contribute to larger free-volume holes within the polymer network. To investigate the effects of free-volume hole distribution on the elastic properties of the epoxy, each sample is subjected to uni-axial tension with a strain rate of $10^5\,\mathrm{sec}^{-1}$ under the similar controlled conditions described previously. Elastic modulus, ultimate strain, as well as the average radius of free-volume holes for several microstructures, are shown in Table 6.1. The elastic modules of the epoxy microstructure as a function of the average radius of free-volume holes are shown in Figure 6.5. As summarized in Table 6.1, systems with a smaller size of free-volume holes exhibit higher strength but fail at lower strains. For a cross-linked system created by curing of DGEBA prepolymers with shorter initial length, the average length of the segments between curing agents is shorter. The rotations of these segments around their backbones are more restricted compared to the system with longer segments. Therefore, the bonds and angles are engaged in the deformation of system from very early stages that leads to a rapid increase internal energy of the system. This contributes to a higher strength for these systems, while their bonds break at lower strains.

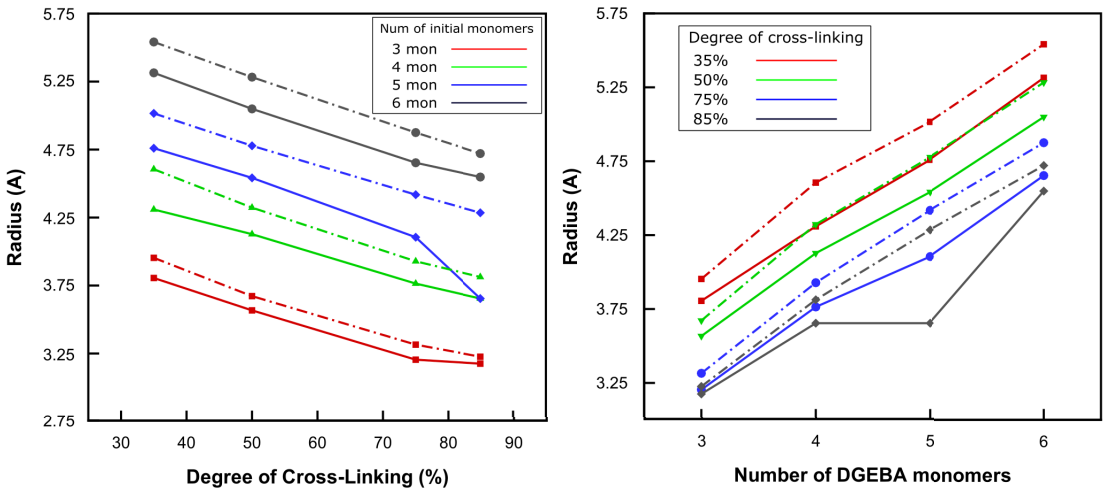

Figure 6.4: Variation of free-volume hole radii as a function of (a) degree of cross-linking; (b) initial length of prepolymers. Solid lines are for a simulation cell having edge length of 20 nm, while the dash-dot lines are from a simulation cell having edge length of 70 nm.

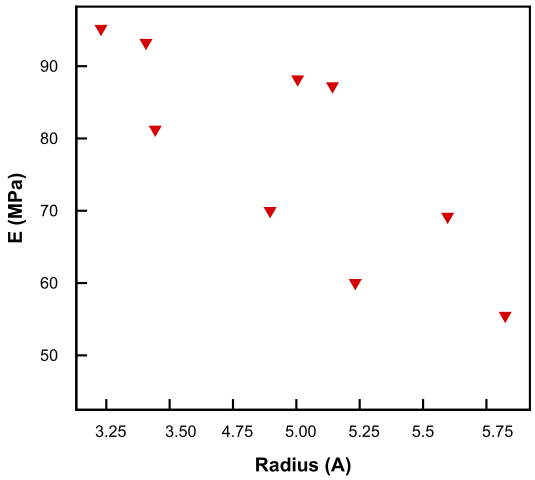

Figure 6.5: Elastic modulus of the epoxy at room temperature for different microstructures.

Radius of free-volumes (Å)	E (MPa)	ν	ϵ_u
5.25	60	0.43	0.236
4.73	69	0.43	0.215
4.61	70	0.41	0.195
3.75	93	0.42	0.187
3.25	112	0.41	0.175

Table 6.1: Summary of the predicted mechanical properties of DGEBA epoxies for miscorstructures with different radius of average free-volume holes

6.3 Location Specific Variations in the Matrix Microstructure of Polymer Matrix Composites

Recently, detailed MD simulations of a silica nanoparticle embedded in polystyrene level have shown that the resin in the immediate neighborhood of the particle has a layerized structure [140, 141]. Analyzing the radius of gyration of the polymer chains has also shown that polymer chains extend to near the particles. The difference between the relaxation time of the matrix near and far from the fiber is also an indicator of slower dynamics of chains around the fibers [141]. However, it is not clear whether this difference is originated from the structural and chemical variation of the matrix around the fiber, or it is simply caused by the mechanical stiffening of the chains around the fibers due to mechanical locking that takes place between chains and the surface of the harder fiber or nanoparticle. Here, the curing algorithm is used to create a cross-linked structure around the fibers of a PMC to identify whether the structure of matrix varies from point to point according to the distance from the fibers.

6.3.1 Simulations of polymer matrix composites

In order to investigate the microstructural variation of the matrix around a fiber in a PMC, a simulation cell having dimensions equivalent to the average distance between

two fibers, which is on the order of 1µm, is needed. However, even with the most efficient coarse-grained models, an enormous amount of resource is required to model a polymer network in a cubic cell with the edge length of a micron. One way to overcome this is to increase the length of simulation cell in the direction normal to the fibers, while limiting the size in the other two directions to smaller lengths. On the other hand, as it is shown in Figure 6.4, structural properties of cross-linked polymer networks, such as free-volume holes distribution, vary with the size of simulation cells. To find out the smallest edge length of a simulation cell that has a distribution of free-volumes independent of the size of the cell, the free-volumes in several microstructures within cells with different edge lengths are compared. This way, any microstructural variation observed across the simulation cell is imposed by the effect of the presence of the fibers, not the length of the cell in the shorter directions. Here, four cubical simulation cells with edge lengths of 20 nm, 50 nm, 70 nm, and 100 nm are created. Then, DGEBA prepolymers, with an average length of 5 monomers, and DAB curing agents are randomly populated inside each cell to achieve a melt with an initial density of $1.16\,\mathrm{g\,cm^{-3}}$. In each case, the network is cured to the maximum degree of cross-linking of 85%. The average radius of free-volume holes in each sample at four different degrees of cross-linking is shown in Figure 6.6. It is observed that the cross-linked network with edge length of 20 nm has slightly smaller free-volume holes as compared to the other simulation cell size. Also, it is observed that the average radius of free-volume holes for networks having an edge length of 50 nm and larger. Thus, the edge length larger than 50 nm is chosen as the smallest length in all the following simulations.

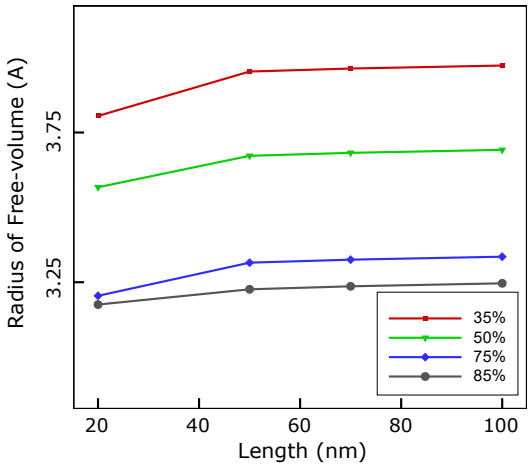

Figure 6.6: Effect of the simulation cell edge length on the predicted average free-volume hole radius for different degrees of cross-linking.

6.3.2 Curing of the matrix between two fibers

The polymers have comparatively lower mobility around the fibers than in the bulk. Thus, it is expected to have different structural properties in the vicinity of the fibers of a PMC as compared to far from them [132]. In the literature, there is an absence of a sophisticated algorithm for creating the structure of matrix around the fibers of a PMC. This is mostly due to the fact that the size of the simulation cell needed for modeling the matrix of a PMC material is substantially larger than the possible scope of MD simulations. Here, a curing process similar to the one discussed in Chapter 3 is employed to create a highly cross-linked matrix in a simulation cell with a length of 800 nm in x direction, and edge lengths of 50 nm in the other two directions. The simulation cell is bound to two fibers at the longer ends of the cell. Periodic boundary conditions are imposed along the shorter directions, y and z, to mimic the bulk properties of the epoxy network. Given that the average radius of carbon nanofibers (CNT) is on the order of a couple of microns, and the depth and width of the simulation cell is only 50 nm, the geometry of the fibers at the ends of the simulation

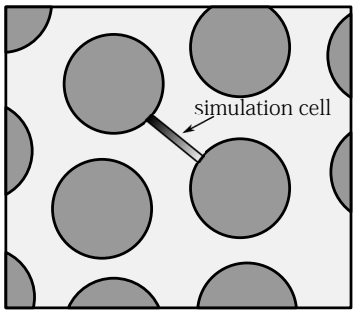

Figure 6.7: Simulation cell between two fibers in a PMC material

cell are simplified as a straight walls, as shown in Figure 6.7. Depending on whether the fiber is chemically coated, fibers either form chemical bonds with the matrix at the interface or the interaction will be merely limited to Van der Waals interactions [19, 142, 148]. Here, the fiber-matrix interaction is simplified using a Lennard-Jones potential function similar parameters defined in Chapter 2.

The simulation starts by randomly populating DGEBA prepolymers, and DAB curing agents inside the simulation cell. These molecules are allowed to diffuse inside the simulation cell according to the guidelines described in Chapter 3. The curing process is then paused after the system reaches a degree of cross-linking of 85%. Finally, the system is relaxed for 1,000,000 time-steps at room temperature.

The average radius of free-volume holes as a function of distance from the surface of the fibers is shown in Figure 6.8. It is observed that the free-volume holes are larger in the immediate neighborhood of the fibers, and decrease in size with increasing distance from the interface. It is also observed that within a distance of 150 nm away from the fiber, the average radius of free-volume holes is smaller than the bulk of the matrix. This is likely due to the fact that polymer chains in the vicinity of the fiber are very immobile. The lack of mobility leads to an accumulation of polymer chains close to the surface of the fiber, creating a denser distribution of polymer chains, and smaller free-volume holes.

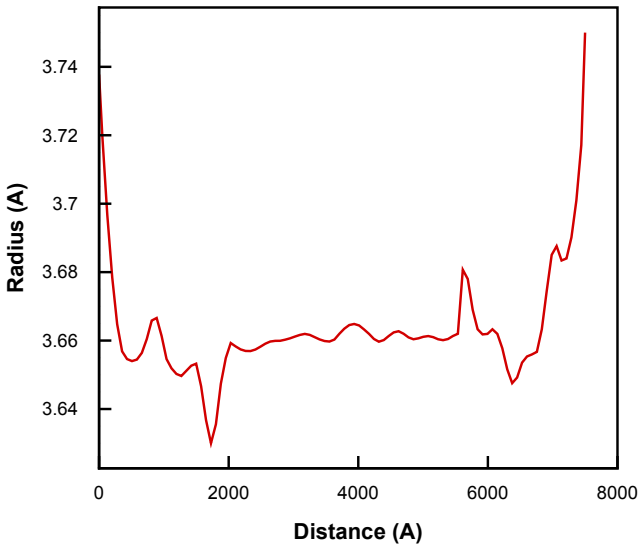

Figure 6.8: The average radius of free-volume holes as a function of distance from the fibers

In the previous section, it was shown that size of free-volume holes dictates the elastic properties of epoxies. Therefore, the variation of free-volume hole radii around the fibers suggests a variation in mechanical properties of resin in those regions. So, perhaps, the more interesting question is if the structural variations of resin around the fibers varies the properties such as strength and damage of PMC.

6.4 Multi-Scale Finite Element Modeling of Damage in PMC Materials

Simulations of damage of a composite material requires a higher length scale model (i.e. FEM) to precisely account for the geometry and interaction of fibers during the deformation. On the other hand, damage in a composite material is inherently a multi-scale phenomenon of coupling damage initiation and propagation at different length scales. However, it is a very common practice in finite element modeling

of composite materials that the matrix is assumed to have homogeneous properties across the simulation box with a damage model that does not account for the effect of microstructure and different damage mechanisms at micro-scale [39, 40]. At the heart of any FEM simulation lies the constitutive model which is a mathematical representation of the materials behavior. The accuracy of FEM results is determined by how accurately the model represent the material at different loading conditions. Furthermore, It is also shown in recent MD simulations of nanoparticles embedded in epoxies at the atomistic level that the resin in the immediate neighborhood of the particle has a layered structure [140, 141]. Therefore, for an accurate FEM representation of damage in PMC, the constitutive model used should not only represent the behavior of the material but also account for structural variation of the resin around the fibers. Here, a multi-scale finite element paradigm is developed to account for structural variation of resin around the fiber by correlating the constitutive model to the free-volume hole distribution of matrix in the PMCs.

6.4.1 Constitutive equations and damage model

The stress-strain relationship provides the overall mechanical response of a material subjected to loading under certain conditions. Here, the stress-strain curves that are generated from coarse-grained MD simulations by applying deformation on the edges of the simulation cells are used to calculate mechanical properties of the epoxy. First, the length of the system in the direction of loading at equilibrium at constant pressure and temperature is defined as h_{equ}. Then the strain is induced by scaling the length of the system to $h = (1 + u)\, h_{equ}$ in terms of the unique displacement matrix u and the equilibrated length of system h_{equ}. With the displacement field defined as $u\,\vec{e}$, the linear strain tensor ϵ is calculated as.

$$\epsilon_{\alpha\beta} = \frac{1}{2}\left(\frac{\partial u_\alpha}{\partial e_\beta} + \frac{\partial u_\beta}{\partial e_\alpha}\right) \tag{6.1}$$

For most solid materials, a linear strain-stress relation holds for the beginning of the deformation until the stress reaches the so-called proportional limit. If the stresses exceed this limit, the deformation becomes nonlinear but the elastic behavior of the material continues until elastic limit of the material is reached. To determine the Young's modulus of the material, the slope of the stress-strain relation of the material in the proportional region is computed using a least square regression. Then, the Poisson ratio, which is the ratio of transverse contraction strain to longitudinal extension strain in the direction of the stretching force, is calculated using $\nu = -\frac{\epsilon_e}{\epsilon_v}$.

As the loading exceeds the proportional limit of the material, the material undergoes a plastic deformation. Here, the plastic deformation region of the stress-strain curve is also simplified to a linear relation until the ultimate stress is reached. To account for the damage that takes place in the matrix at higher strains, it is assumed that the material degrades within 5% of strain before it loses its stiffness. The degradation of the material is, then, measured as a function of stress as follows [149]:

$$\sigma = (1 - sdeg) \times \acute{\sigma} \tag{6.2}$$

where $\acute{\sigma}$ is the stress of the undamaged part, and *sged* is the degradation of the material. After the material is completely degraded, it will be removed from the system to avoid numerical instability of the FEM model. The schematic of material bahavior as a function of strain is shown in Figure 6.9. The values of E, ϵ_y, σ_u, and ϵ_u as a function of the average radius of the free-volume holes are defined from the uni-axial tension coarse-grained MD simulations of the epoxy as discussed in Section

6.2.2. The functional form for these quantities can be represented as follows:

$$
\begin{aligned}
E(r) &= 7.3705r^2 - 88.4084r + 321.27; R^2 = 0.9392 \\
\epsilon_y(r) &= y = 0.0226r^2 - 0.1545r + 0.3426; R^2 = 0.9102 \\
\sigma_u(r) &= 1.4556r^2 - 12.091r + 37.605; R^2 = 0.7466 \\
\epsilon_y(r) &= 0.0136r^2 - 0.0869r + 0.3161; R^2 = 0.8912
\end{aligned}
\tag{6.3}
$$

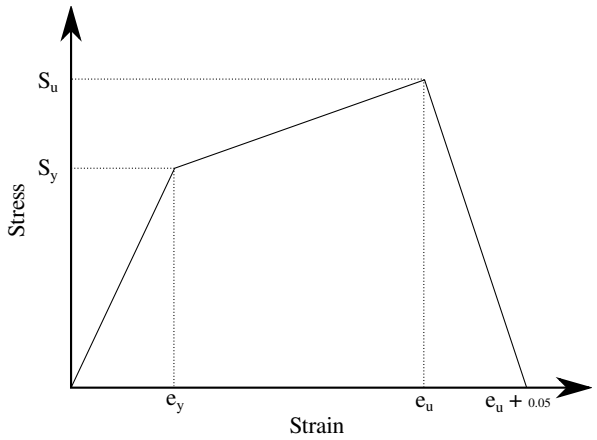

Figure 6.9: The simple stress-strain relation of the epoxy

6.4.2 Distribution of material properties in the matrix

As it was shown in Section 6.2.2, the free-volume size of a resin dictates its material properties such as elastic modulus and ultimate strain. In order to create a finite element model that represents the structural variation of resin around the fibers, here, the mechanical properties of each element are chosen such that the corresponding size of the free-volume holes for the element follows the free-volume distribution calculated from the coarse-grained MD simulations. For this purpose, first, the MD simulation cell is divided into multiple regions along the direction normal to the fibers. Then, the probability density function of free-volume hole radii for each region is calculated. Next, a random radius is assigned to each element based on the distance of its cen-

ter of geometry from its closest fiber such that the distribution of the random radii chosen for an element within a range of distance from the fibers follows the distribution calculated from coarse-grained MD simulation. Finally, elastic properties, and constitutive model of each element are chosen based on the radius of voids that is assigned to the element. This process is demonstrated in Figure 6.10.

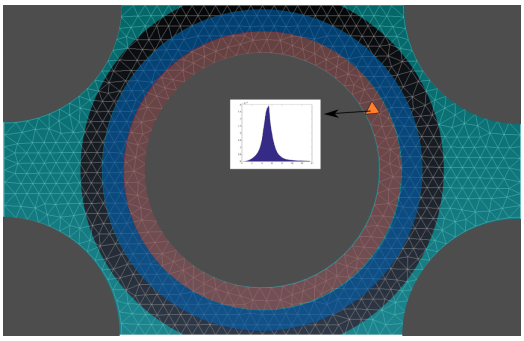

Figure 6.10: Sampling material properties using the coarse-grained MD simulation of matrix

The contour of the radius of free-volume assigned to each element is shown in Figure 6.11 for a PMC with the length of 11 µm, and width of 7 µm having five fibers with the radii of 2.5 µm at the corners and the center of the box. It is seen that the material properties vary in different layers in the immediate vicinity of the fibers similar to what is observed in Figure 6.8. This variation reflects the structural variation of resin around the fibers in composite materials.

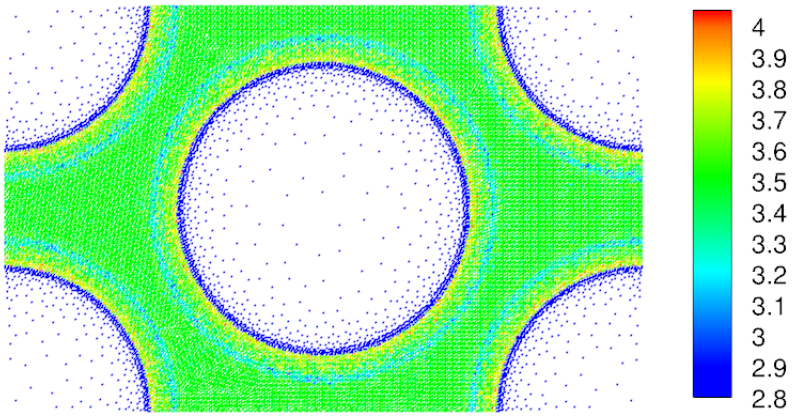

Figure 6.11: The contour of distribution of the radius of free-volume holes across the matrix, the blue color of elements inside the fibers are due to the radius of 0 assigned to them

6.4.3 Uni-axial tension simulations

Here, to investigate the effects of structural variation of resin on the behavior of composites, the strength and damage of two PMCs with a localized, and a homogeneous damage model predicted from a two-dimensional finite element model are compared. First, to investigate the effect of the localized damage model on the damage growth of PMCs, a fiber with the radius of 2.5µm is embedded at the middle of a matrix in a simulation cell with dimensions of 20 µm in length and 10 µm in height. A quasi-static uni-axial tension is then imposed on the shorter dimensions of the simulation cell. In order to eliminate the effect of mesh quality on the direction, and location of the damage, a structured symmetrical mesh composed of 17,324 regular quadrilateral elements is generated, as shown in Figure 6.12. In Figure 6.12(a), the uniform average properties of the matrix are assigned to all elements in the PMC matrix. In Figure 6.12(b), the material properties of each element around the fiber is randomly selected using the guideline discussed above. The constitutive equations of the matrix are defined as a function of radius of average free-volume holes as defined by Equation 6.3. The fiber is assumed to deform elastically with an elastic modulus of 270 GPa,

and poison ratio of 0.3. The simulations are conducted under plain strain conditions assuming the samples have an infinite depth. Free end boundary conditions are imposed at the right edge, and the displacement of nodes on the left edge are constrained. Periodic boundary conditions are applied at the top and bottom edges of the simulation cell. Simulation is conducted by exerting a displacement of 6µm in 200 steps on the right edge of the cell. The following simulations are done in the commercial software Abaqus [149].

The contours of horizontal, and vertical displacements for both samples are

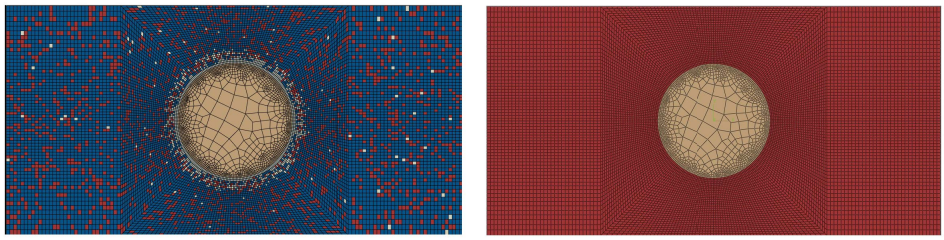

Figure 6.12: Finite element mesh used for the simulation with (a) mechanical properties of matrix vary with distance from the fiber, and (b) matrix has uniform properties across the cell.

shown in Figure 6.13. Given that simulations are done under displacement control conditions, the horizontal and vertical displacements of each sample are identical as expected.

Given the identical displacement fields of both PMCs, it is expected to observe a variation in stress across the PMCs. The contours of stress components, σ_{xx}, and σ_{yy} are shown in Figure 6.14. It is seen that the stress components have a more uniform, and patterned distribution in the sample with homogeneous matrix property than the one with localized properties.

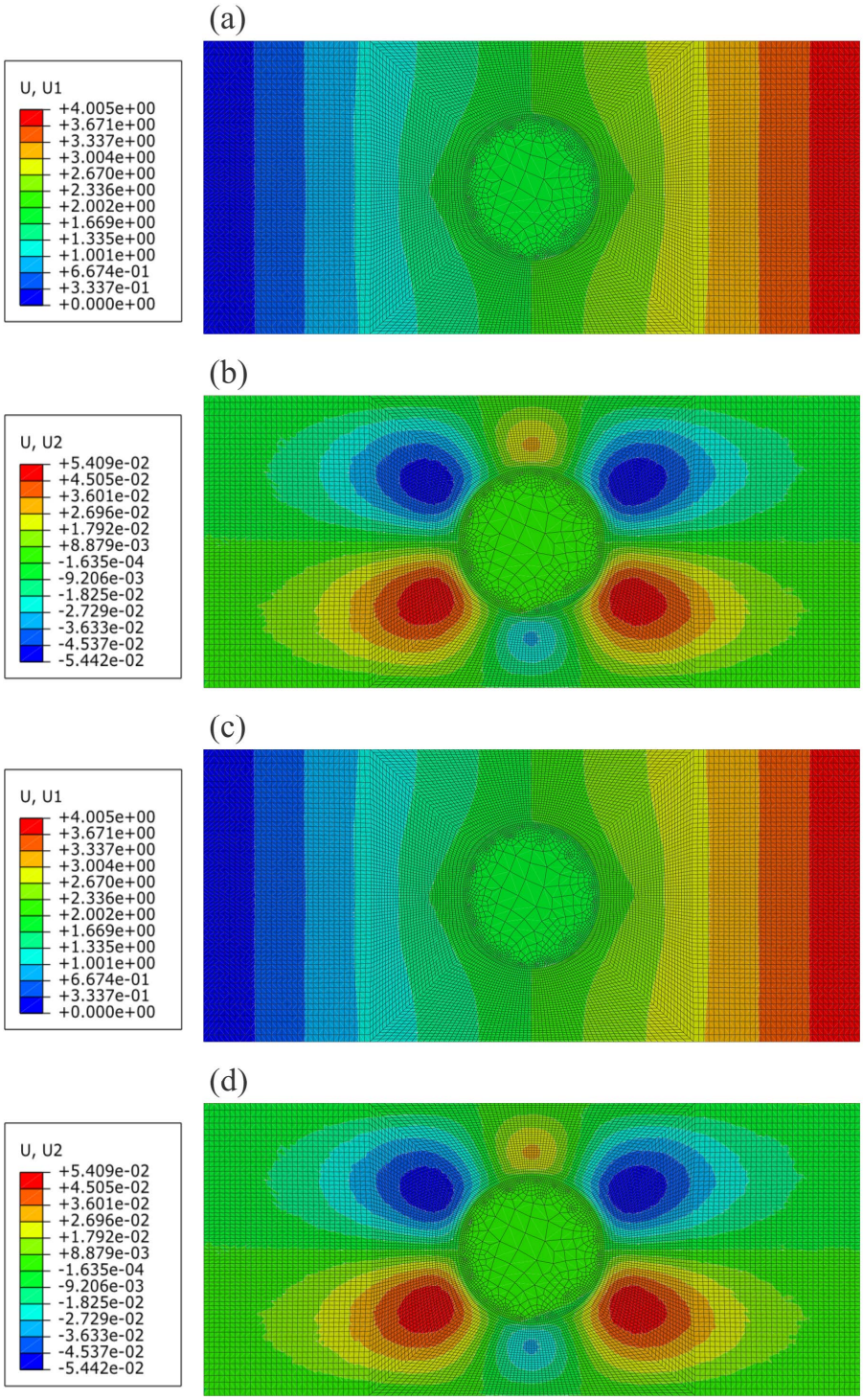

Figure 6.13: The contour of (a) horizontal, and (b) vertical displacements for sample with uniform resin, (c) horizontal, and (d) vertical displacement for sample with varying structure of resin

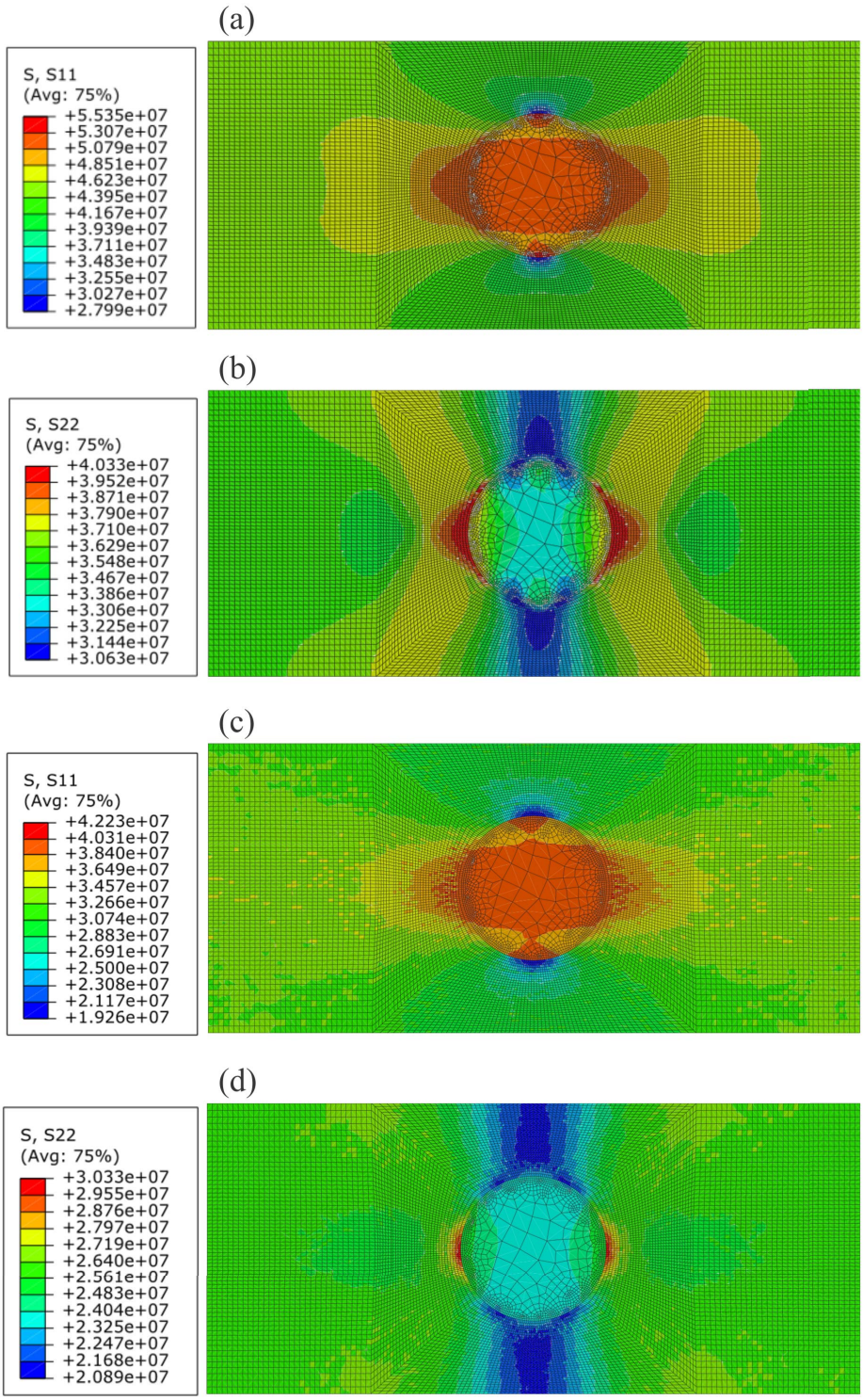

Figure 6.14: The contour of stress components (a) σ_{xx}, and (b) σ_{yy} for the PMC with homogeneous resin, (a) σ_{xx}, and (b) σ_{yy} for the PMC with varying structure of resin

The contours of material degradation at one step before failure are shown in Figure 6.15 for both samples. Given the symmetric nature of the problem, it is to expect that the failure occurs concurrently around the fiber where the shear bands are forming. As shown in Figure 6.15(a), the degradation bands on the PMC with homogeneous of matrix properties shows a symmetric pattern for damage growth along two shear bands around the fiber. However, for the PMC having a matrix with position-dependent properties, the failure takes place at the edge where the resin is slightly stiffer. The stress and strain relation for both samples are also shown in Figure 6.16. The slopes of stress-strain curves for both samples are very close to each other, indicating that the elastic properties of the uniform matrix correctly represents the average behavior of the matrix. However, as the material deforms plastically, it is seen that the final strength of the material predicted from the PMC with uniform matrix is higher than the one with localized damage model.

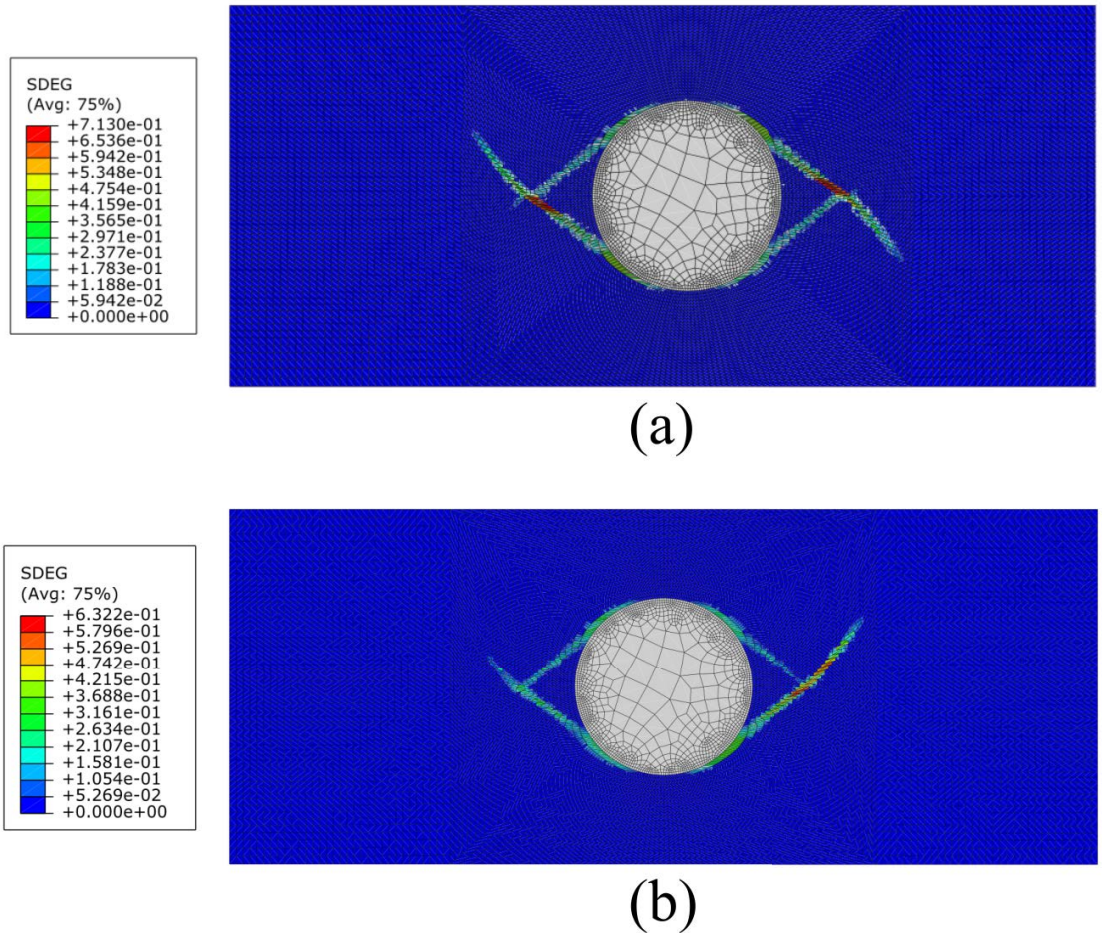

Figure 6.15: The contour of material degradation for the PMC with (a) homogeneous resin, (b) resin with varying material properties

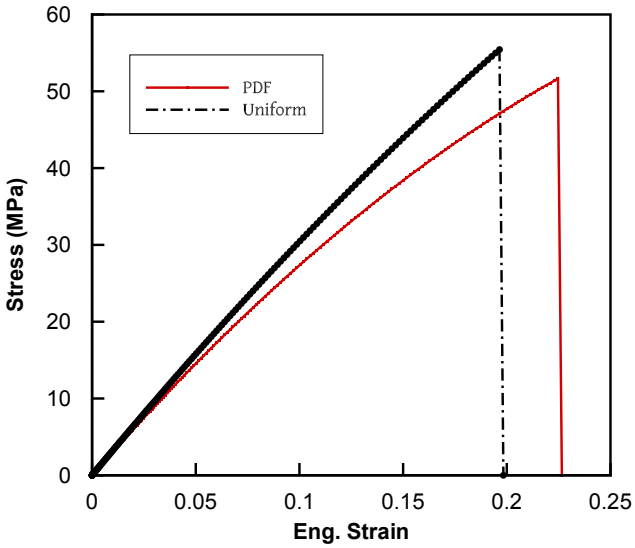

Figure 6.16: stress-strain relation of the PMC with homogeneous matrix and PMC with localized damage model

Similar simulations were performed repeated to for a simulation cell having five fibers with a radius of 2.5µm located at the corners and the center of the simulation cell. An unstructured mesh is generated that is composed of 18,854 number of regular triangular elements, as shown in Figure 6.17. The mesh has a finer resolution around the fibers to capture the structural variations of resins around the fibers more accurately. In Figure 6.17(a), the material properties such as elastic modulus, and damage model of each element are chosen according to the guidelines discussed in detail in the previous section to account for structural variation of the matrix around the fibers. The matrix of the PMC shown in Figure 6.17(b) has homogeneous material properties. Fibers are assumed to deform elastically with Elastic modulus of 270 GPa, and poison ratio of 0.3. The constitutive equations of the matrix is defined as a function of radius of average free-volume holes defined in Equation 6.3. The simulation cell has an edge of 11 µm in length, and 7 µm in width. The simulation is conducted under plain strain conditions assuming the samples are infinitely long in depth. Free end boundary condition is imposed at the right edge, and displacement

of nodes on the left edge are constrained. Periodic boundary conditions are applied at the top and lower edges of the simulation cell. Simulation is conducted by applying a displacement of 2nm which is exerted on 200 steps on the right edge of each cell.

The contours of deformations for each cell are drawn in Figure 6.18. Similar to

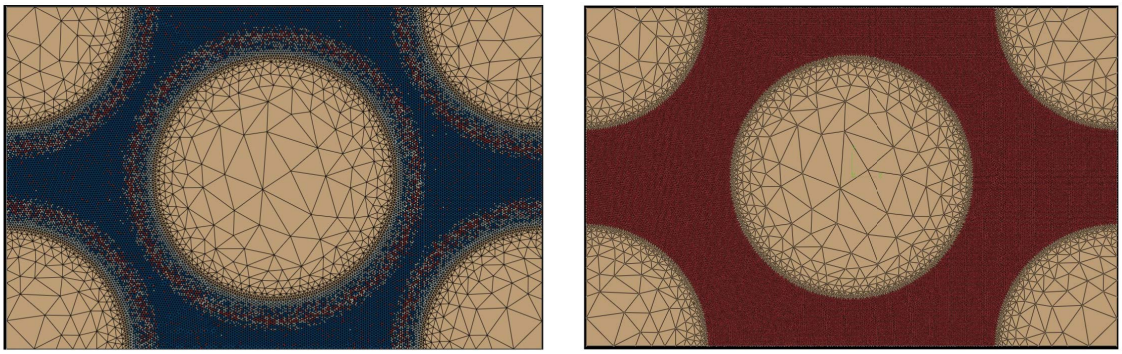

Figure 6.17: Finite element mesh used for the simulation with (a) mechanical properties of matrix vary with distance from the fiber, and (b) matrix has uniform properties across the cell.

previous simulations, identical deformation fields are observed for each simulation. However, the contour of ductility shows the matrix exhibits a ductile response in isolated bands around the fibers, while the ductility map is more diffused and dispersed for the PMC with the matrix having a localized damage model, as shown in Figure 6.19. The contours of degradation of material around the fibers show a similar dominant pattern for damage growth in both simulations. However, in the simulation with the matrix with localized damage model damage initiation is observed around the fibers on the right bottom corner of the cell, while the matrix in a similar location on the other cell is not damaged. Finally, the stress-strain curves of both cells are plotted in Figure 6.21. It is seen again that the PMC with the homogeneous matrix exhibits a higher strength. In comparison to the PMC with only one fiber in the middle of the matrix, this PMC is less ductile, and stiffer due to the effects of added fibers.

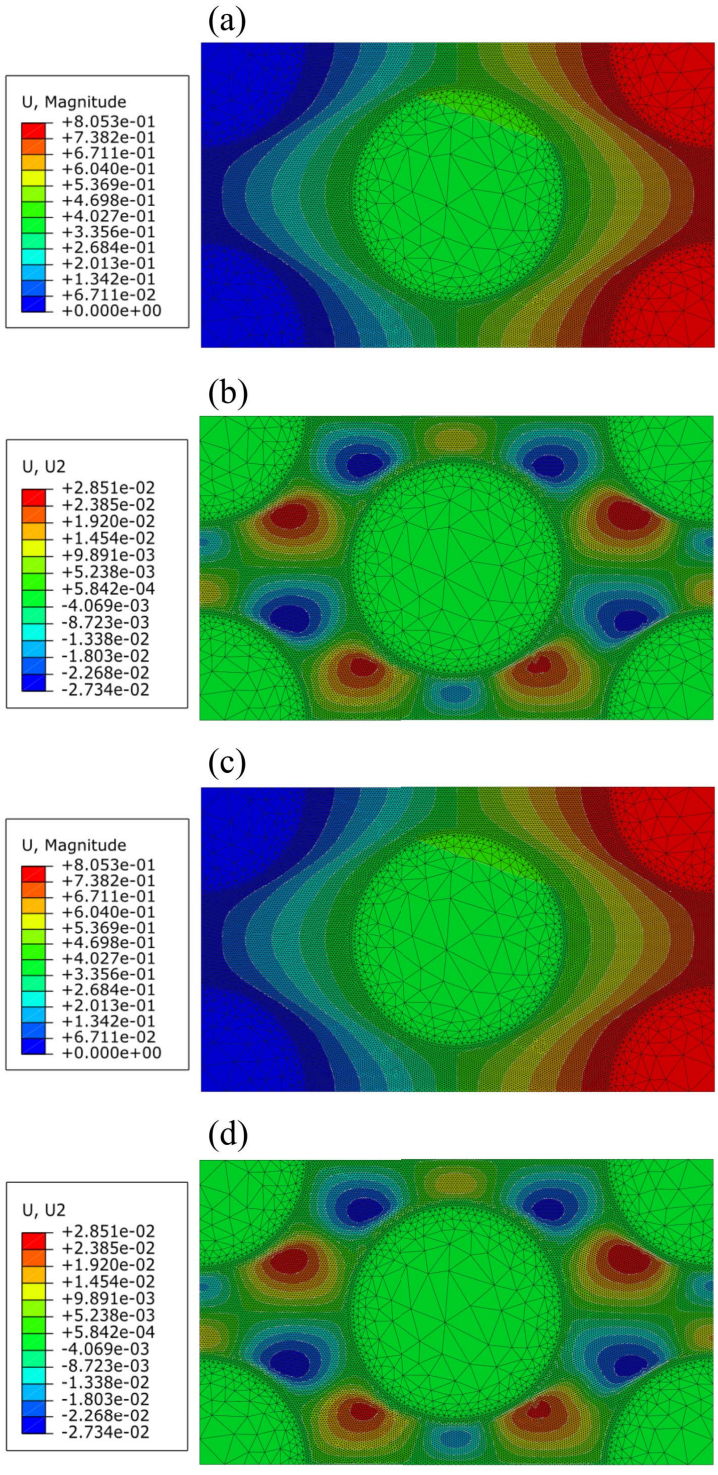

Figure 6.18: The contour of (a) horizontal, and (b) vertical displacements for sample with uniform resin, (c) horizontal, and (d) vertical displacement for sample with varying structure of resin.

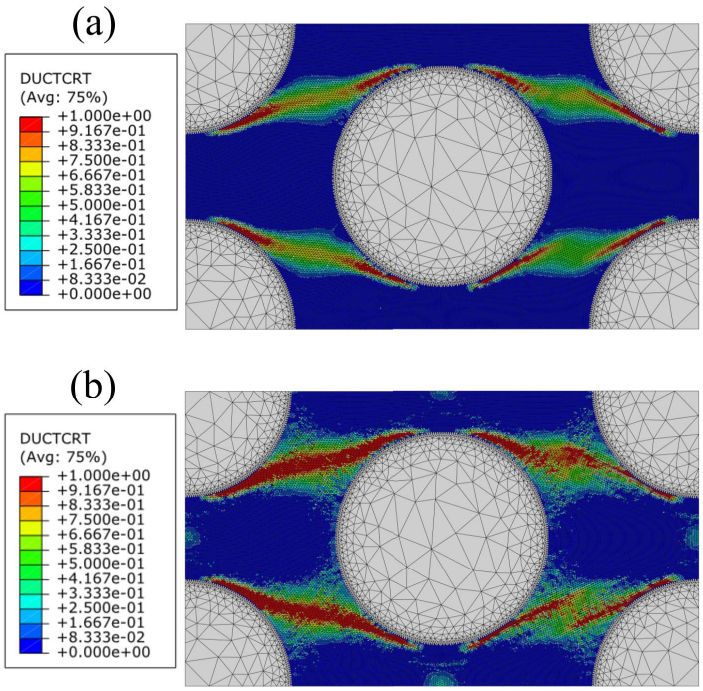

Figure 6.19: The ratio of ductility in the PMCs for (a) cell with the matrix having uniform properties, and (b) matrix having localized damage model.

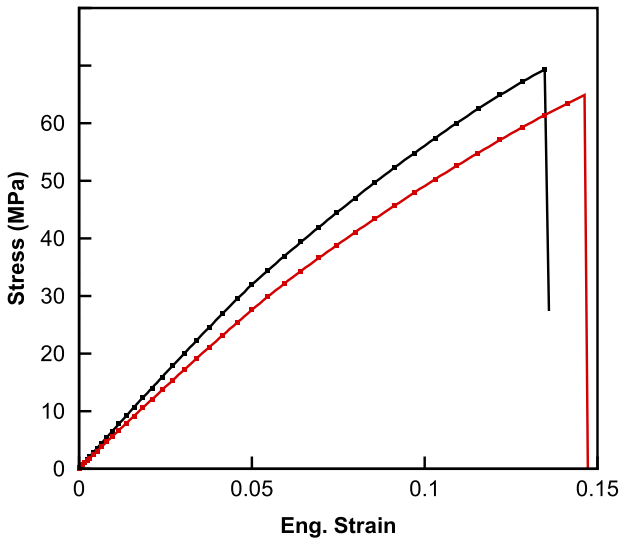

Figure 6.21: stress-strain relation of the PMC with homogeneous matrix and PMC with localized damage model

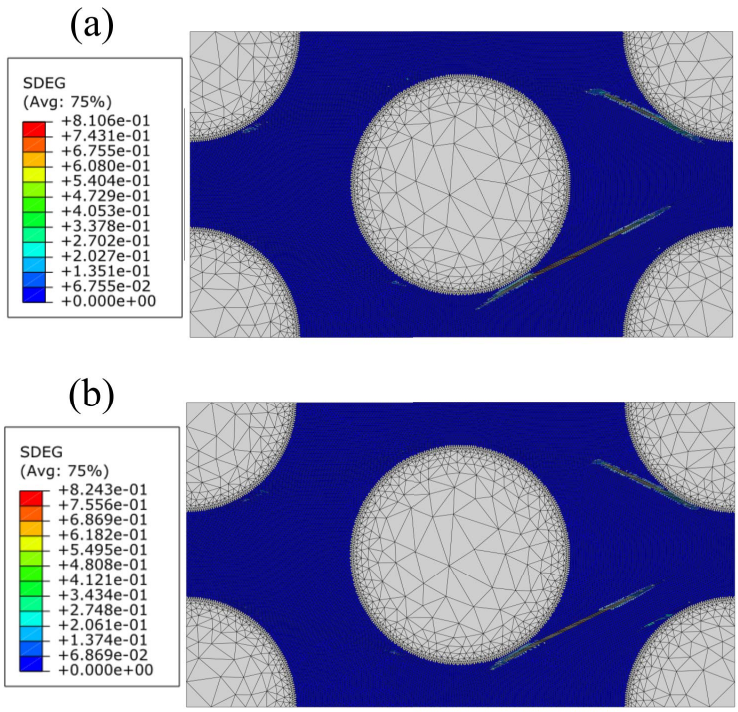

Figure 6.20: The degradation in the PMCs for (a) cell with the matrix having uniform properties, (b) matrix having localized damage model

6.5 Summary and Conclusions

In this Chapter, the effects of free-volume on the strength, and elastoplastic behavior of the epoxy systems is investigated. First, it is shown that the the radius of average the free-volume holes decreases rapidly during the energetic hardening region of stress-strain relation of a loosly corss-linked DGEBA system, the bonds are pulled taut under deformation. Then, the effect of free-volume size on strength of glassy cross-linked DGEBA networks is investigated. It is observed that a system with smaller size of free-volume hole exhibits a tougher response. Then the free-volume distribution is calculated for the matrix around fibers in PMCs. The results show variation of free-volume hole size around the fibers. So, a multi-scale finite element model is used to investigate the effects of the structural variations of matrix on the strength and damage growth in PMCs. The comparison between two fem models , one with a homogeneous matrix, and one with a matrix with localized properties, shows that uniform matrix overestimates the strength of PMC. It is also observed that the direction of damage growth in the PMC varies for the PMC with localized matrix properties. A summary of the findings is listed below.

- Epoxies with smaller free-volume holes have a higher strength due to lower mobility of polymer chains.
- Free-volume holes in a matrix are larger around the fiber in comparison to those in the bulk.
- Material properties of the matrix in PMC is a function of distance from the fiber.
- The multi-scale finite element simulation shows that a PMC with a uniform matrix properties overestimate the strength of composite.

- The finite element simulations of damage growth shows that the damage propagation varies for the composite with the localized damage model.

Chapter 7

Conclusions and Suggested Future Directions

7.1 Summary and Conclusions

In this work, a coarse-grained MD model was developed to study the effect of structural features, in particular free-volume hole distributions, of cross-linked networks on the predicted properties of epoxy systems. The problems presented in this thesis were mainly focused on creating a better insight into the molecular origins of the unique properties of cross-linked epoxy systems such as thermal transitions, strength, and damage of matrix in composites. One of the major shortcomings of a higher scale computational model used for modeling amorphous polymer systems is the inability of these models to incorporate the structural features of the system. This is mostly due to the complexity of getting conformation specific experimental data from low scale experiments. Here, new tools were developed that allows researchers to extract useful information such a distribution of voids, the local density of the system from various types of molecular models. The tool, developed in this thesis, can be used to incorporate information from lower scale models to coarser length scale models in a

hierarchical fashion for a more physics-based prediction of properties of a component.

The materials chosen here were diglycidyl ether of bisphenol A , DGEBA, as polymers, and 1,4 Diaminobutane, DAB, and N,N'dimethyl-1,6-, diaminohexane, DDH, as curing agents. This material was chosen primarily for its general use as a matrix in polymer matrix composites in many aerospace applicanttions. Nevertheless, the tools and approaches described in this thesis can be applied to any polymeric materials. A coarse-graining method was proposed in which atoms of DGEBA monomer were grouped into two coarser particles, defined as super-atoms. Similarly, the curing agent molecules are also represented by super-atoms that encapsulate all the atoms in their molecules. The interactions between atoms inside these beads are accounted for defining a spring-bead interaction between the coarse-grained particles. The interaction potentials, which represent the stiffness of the springs between the super-atoms, are calculated by inverting the Boltzmann distribution of the coarse-grained coordinates that are computed at different temperatures by sampling over the energy surface of these systems using a large number of quantum mechanics simulations. The pair potentials are optimized for the density of the system at different temperatures. The combined number of degrees of freedom for a DGEBA monomer, locations, angles, bonds, and dihedral angles, are twenty times fewer that the equivalent atomic structures of the monomer. On the other hand, given the coarser length scale of the atoms in the coarse-grained model, the system is softer. Hence, longer time intervals can be used for the integration of dynamic equations of motions. Therefore, the effective speed-up gained from coarse-graining is higher. Furthermore, a bond breaking criteria is developed with the assumption of a smooth transition in the energy of the system when bonds break, and atoms move from a chemically bonded state to a non-bonded state. The length of $1.122 \times d_{equ}$ was defined for two atoms at max stretch.

For a realistic simulations of highly cross-linked epoxy systems, the starting chain network in the simulations should represent a realistic cross-linked amorphous mi-

crostructure with the correct degree of cross-linking. Here, a new curing algorithm was developed to create highly cross-linked networks with a uniform distribution of cross-linking across the simulation cell. This algorithm controls the degree of cross-linking at different regions in the simulation cell and creates a shaking process in regions where the potential reactive monomer are trapped to release the monomers and allow easier movement inside the simulation cell. The curing process modeled with this algorithm was compared to the traditional curing algorithm in the literature. The outcoming cross-linked system is more uniform than the network cured by the traditional algorithm. It was also shown that the new algorithm can create networks with a higher degree of cross-linking than the traditional methods. A 5% volumetric shrinkage is observed for the network after curing, which is in good agreement with experimentally measured volumetric shrinkage. It was also shown that the network goes from a liquid state to a gel state at the curing degree of 70 %. This is in good agreement with both theoretical, and experimentally measured gel point of the system.

A new algorithm was also developed to quantify the free-volume hole distribution inside a polymeric network. This algorithm creates a geometry graph of the polymer chains to search for free-volume holes in the system. The free-volume hole distributions of a highly cross-linked DGEBA epoxy network at different temperatures and pressures were compared to the distributions measured from PALS experiment on the similar material. The calculated distributions are in good agreement with those measured in PALS experiments. It is also shown that the glass transition temperature measured from the kink on the average radius of the free-volume holes versus temperature curve is in good agreement with the glass transition temperature measured by the specific density versus temperature curve. Similar observation were made from the PALS experiments that suggest that the glass transition temperature can be directly measured from the evolution of free-volume holes of the system as a function

of temperature.

To investigate the effect of structural variation on the glass transition temperature of the epoxies, several highly cross-linked epoxy systems were created by changing the initial length of DGEBA pre-polymers at different degrees of cross-linking. The distribution of the free-volume holes calculated from the simulations shows a system with a longer initial length of prepolymers has larger free-volume holes and increasing the degree of cross-linking of the system reduces the average size of free-volume. The internal energy of the system determines the size of free-volume holes. Larger free-volume holes are indicators of lower energy in free volumes, therefore polymer chains in a system with larger free-volume holes are considered to be more mobile compared to those in a system with smaller free-volumes. Thus, as shown by the results presented in Chapter 5, it is expected that a system with higher mobility exhibits softer behavior, and subsequently a lower glass transition temperature.

To quantify the effects of free-volume holes on the glass transition temperature of the system, a thermal evolution model was proposed for a single free-volume hole. The parameters of this model were optimized to represent the evolution of the average size of the free-volume holes of the system. Given that the material is the same for each system, the same parameters were used to see if the model can predict the glass transition temperature of networks with different distributions. The glass transition temperatures predicted from the evolution model were shown to be in excellent agreement with those calculated from the simulations. The evolution model suggests that glass transition of an epoxy can be predicted given the initial distribution of free-volume holes. The model was also used to predict the glass transition temperature of a real polymer given the PALS measurements of the free-volume holes, and were shown to be excellent agreement with the experimental predictions.

The effect of free-volume holes on the strength and mechanical behavior of epoxy systems under mechanical loading was also investigated. It was shown that a cross-

linked system with smaller free-volume holes shows higher strength, while it fails at lower strains. The explanation of this behavior is based on the mobility of these systems. A system with smaller free-volume holes is less mobile than as system with larger free-volume holes. When an epoxy system is under deformation, if the polymer chains are long enough to allow large segmental rotations and undergo large conformation changes without bending bonds, and angles the material behaves like a rubber. When a system is immobile, the bending and stretching of bonds and angles along the backbone of polymer chains contribute to the stiffness of the system. Therefore, a system with lower mobility usually exhibits a stiffer behavior. However, because bonds and angles are engaged in the deformation of the system from the beginning of the deformation, bonds will break at a comparatively lower stain compared to a softer system.

Finally, a coarse-grained simulation cell representing the matrix of a PMC spanning between two fibers was created by curing a blend of prepolymers. The spacing between the fibers in this simulations was on the order of 800 nm. The distribution of free- volume holes was then calculated for the system. It is observed that the free-volume around the immediate vicinity of the fibers are different in size than those in the bulk of the matrix. Given the established correlation between the average size of free-volumes and mechanical properties of the matrix, it is concluded that mechanical properties of the matrix around the fibers are different that the bulk of the matrix. Therefore, a multi-scale finite element framework was designed to account for the structural variation of the matrix around the fibers by randomly assigning material properties to the elements in the immediate vicinity of the fibers based on their distance to the matrix-fiber interface, and according to the free-volume holes distribution calculated from the coarse-grained MD simulations. The strength and damage of the PMCs having resins with localized material properties were compared to PMCs with homogeneous matrix properties. The comparison shows that the matrix with

homogeneous resin overestimates the strength of the PMC. It was also observed that damage initiates in a different location inside the matrix of the PMC with localized resin properties. This difference suggests that a better understanding of the structure of resin is required for a more accurate prediction of the damage in PMCs.

7.2 Suggested Future Directions

The research described in this dissertation is only a humble step in the direction towards developing a complete, physically accurate, meaningful multi-scale description of the properties of epoxy polymers, and PMCs. There is an enormous number of idealizations, simplifications, approximations and neglected mechanisms that need to be addressed. An equal emphasis should also be placed on improving the computational tools used in these simulations. In this section, a number of these problems will be briefly described. This is by no means an extensive list of the issues that need to be addressed in the future.

First and foremost, all coarse-grained models suffer from a lack of precision in capturing the accurate conformation of polymer chains under deformation. Coarser representation of beads means lower accuracy in modeling the confirmation of atoms. Therefore, for applications the required an accurate modeling of chains conformations, such as deformation under high strain rate, coarse-grained models usually result in a catastrophic increase in temperature in the simulation cell. Here, the coarse-grained model was initially used to calculate free volume holes of epoxies at different temperature and pressures. So, a coarse-graining technique was adapted to reproduce a relatively accurate thermal behavior of these systems. This model needs to be modified if a more accurate characterization of the behavior of polymer chains under active deformation is required.

The thermal evolution model proposed for prediction of the glass transition tem-

perature of these systems was built upon simulations conducted at an identical cooling rate. However, it is known that cooling rate varies the glass transition temperature of the system. So, further investigation is needed to incorporate the effects of cooling rates in the prediction of glass transition temperature.

In the simulations of PMCs, a fundamental simplification used was for the fiber-matrix interaction. In this thesis, the fiber matrix interaction was simplified by LJ potentials. However, it is known that the electrostatic charges on the surface of nanotubes play an important role in fiber-matrix interaction. A careful characterization of fiber-matrix interaction at the interface is required for a more accurate physics-based representation of PMCs. On the other hand, fibers with industrial applications are usually chemically coated, so they can form the bond and improve the adhesion of matrix to the fiber. It is very crucial to know how the chemical coating of fibers alters the structure of the resin around it. After the fiber-matrix interaction is well-characterized and the interaction of fiber and matrix are incorporated into a coarse-grained model, different curing techniques should be used to created the structure of the matrix between fibers. It is clear that the curing process does affect the structure of the matrix around the fiber, although its effects can not be well understood as long as the well-defined model for fiber-matrix interaction is missing. Also, comparison of the structural features of the matrix such as free-volume holes distribution of the matrix with PALS experiment can be used to shed light on the problem, and create a thorough understanding of the matrix properties around the fibers.Finally, the finite element simulations used here as a proof of concept to highlight the effects of a localized damage model on the strength and damage evolution of PMCs. However, these simulations are not nearly enough to develop an understanding about the failure, and damage mechanisms of these materials. First, a cohesive zone model needs to be calibrated to account for the fiber-matrix debonding. Then, several simulations with different arrangement of fibers in the PMC should be conducted to understand the

effect of fiber arrangement on the failure pattern of PMCs.

Appendix A

Coarse-Grained potentials

Bond Potential*	T = 150 K		T = 250 K		T = 300 K	
	K_d	d_{eq}	K_d	d_{eq}	K_d	d_{eq}
$C \rightleftharpoons A$	8.323	7.10	5.882	7.06	5.5903	7.04
$F \rightleftharpoons F$	10.311	5.90	7.287	5.85	6.942	5.89
$F \rightleftharpoons C$	9.904	4.65	7.000	4.66	6.652	4.67
Angular Potential†	K_θ	θ_{eq}	K_θ	θ_{eq}	K_θ	θ_{eq}
$\widehat{CAC}$	11.697	135.866	7.525	134.445	6.741	136.969
$\widehat{ACA}$	4.574	140.531	3.545	141.961	3.499	143.125
$\widehat{FFC}$	13.974	151.73	11.721	150.84	10.944	150.84
$\widehat{CFC}$	14.663	65.046	12.185	65.132	11.995	65.132
$\widehat{FCA}$	11.975	75.01	9.246	75.13	8.875	75.13

$^\star : U_{bond} = \frac{1}{2}\, k_d (d - d_{eq})^2, \qquad ^\dagger : U_{angle} = \frac{1}{2}\, k_\theta (\theta - \theta_{eq})^2$

Table A.1: Parameters for coarse-grained potentials calculated at different temperatures

Torsional Potential*		K_1	K_2	K_3	K_4
T = 150 K	$\widetilde{CACA}$	297.854	-168.0599	60.015	-10.2135
	$\widetilde{ACFC}$	27.125	-16.452	10.325	-1.125
	$\widetilde{ACFF}$	19.345	-14.055	9.744	-1.542
	$\widetilde{CFFC}$	29.233	-16.854	11.123	-1.954
T = 250 K	$\widetilde{CACA}$	296.2	-168.8352	59.8352	-10.74
	$\widetilde{ACFC}$	25.315	-16.021	10.015	-1.045
	$\widetilde{ACFF}$	18.954	-13.532	9.452	-1.235
	$\widetilde{CFFC}$	28.123	-16.123	10.865	-1.684
T = 300 K	$\widetilde{CACA}$	289.674	-161.759	57.656	-10.1758
	$\widetilde{ACFC}$	25.012	-15.851	9.754	-0.985
	$\widetilde{ACFF}$	18.025	-13.132	9.109	-1.0135
	$\widetilde{CFFC}$	25.845	-15.754	10.124	-1.215

* : $U_{dih} = \frac{1}{2}K_1[1+\cos\phi] + \frac{1}{2}K_2[1-\cos 2\phi] + \frac{1}{2}K_3[1+\cos 3\phi] + \frac{1}{2}K_4[1+\cos 4\phi]$

Table A.2: Parameters for coarse-grained potentials calculated at different temperatures

Appendix B

Calculation of the Glass Transition Temperature

In reality, the glass transition is not a discrete thermodynamic transition, but rather a temperature range over which the mobility of the polymer chains increases significantly than a discrete thermodynamic transition. However, typically a single value for T_g is defined as the mean temperature bounded by tangent lines to the two straight regions of the high and low-temperature parts of the specific volume versus temperature curve. It has been shown in the literature that the specific volume versus temperature curves of polymeric system can be accurately fitted using a spline function [105]. Therefore, a distinct kink on the curve is not observed for calculation of glass transition temperature. Here, to calculate the glass transition temperature of the epoxies, the following guild lines is employed [93]. First, the temperature range is dived into several regions. Then, two lines are fitted into the the data points at the first, and last regions. Next, the two lines in the two first and last regions are fitted to the data points. The two lines that more accurately represent the shape of the spline function are selected as the lines of the glassy and rubbery regions. The temperature at the intersection of these two lines is the glass transition temperature.

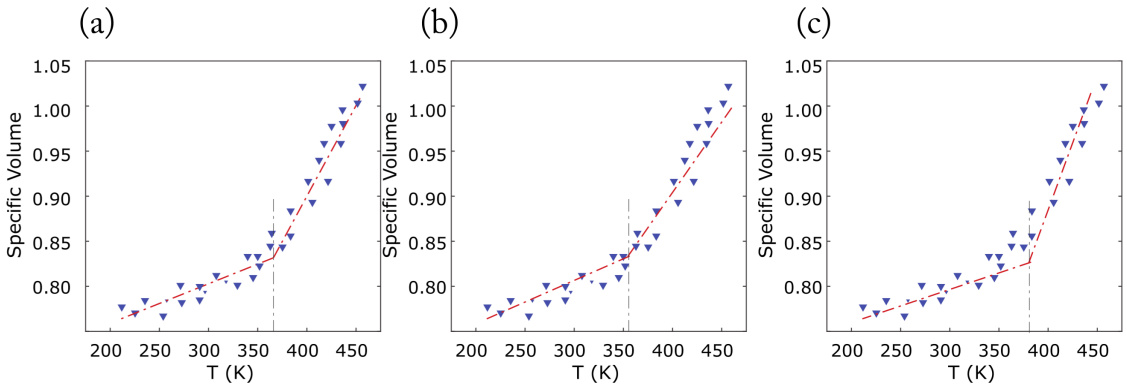

Figure B.1: (a) Lower bound, (b) midpoint and (c) higher bound of the range of glass transition temperature.

The standard error for measuring the glass transition temperature is calculated by finding the range of intersections from all possible fits to the data set by two straight lines.

Bibliography

[1] http://bit.ly/2dylimk, .

[2] http://www.pbs.org/wgbh/nova/tech/strong-materials, .

[3] http://bit.ly/2dk3yn9, .

[4] http://bit.ly/2et2oey, .

[5] C. Wu and W. Xu. Atomistic molecular modelling of crosslinked epoxy resin. *Polymer*, 47(16):6004–6009, 2006.

[6] Q. Deng and Y.C. Jean. Free-Volume Distributions of an epoxy polymer probed by positron annihilation: pressure dependence. *Macromolecules*, Di(26):30–34, 1993.

[7] R.F. Heizer. The background of thomsen's three-age system. *Technology and Culture*, 3:59–266, 1962.

[8] U.S. Congress. *Advanced Materials by Design*. 1988.

[9] A. Schiraldi and P. Baldini. *Epoxy polymers*, volume 28. Wiley, 1983.

[10] A. Rudin and P. Choi. *The elements of polymer science and engineering*. Academic Press, 2013. ISBN 9780123821782.

[11] R.A. Dickie, S.S. Labama, and R.S. Bauer. *Cross-linked Polymers: Chemistry, Properties and Applications*. American Chemical Society, 1988.

[12] F.M. Capaldi, M.C. Boyce, and G.C. Rutledge. Molecular response of a glassy polymer to active deformation. *Polymer*, 45(4):1391–1399, 2004. doi: 10.1016/j.polymer.2003.07.011.

[13] V. Lyulin, K. Balabaev, A. Mazo, and M. Michels. Molecular dynamics simulation of uniaxial deformation of glassy amorphous atactic polystyrene. *Macromolecules*, 37(23):8785–8793, 2004.

[14] D. Hossain, M.A. Tschopp, D.K. Ward, J.L. Bouvard, P. Wang, and M.F. Horstemeyer. Molecular dynamics simulations of deformation mechanisms of amorphous polyethylene. *Polymer*, 51(25):6071–6083, 2010.

[15] H. Eyring. Viscosity, Plasticity, and Diffusion as Examples of Absolute Reaction Rates. *The Journal of Chemical Physics*, 4(4):283, 1936.

[16] R.E. Robertson. Theory for the Plasticity of Glassy Polymers. *The Journal of Chemical Physics*, 44(10):3950, 1966.

[17] K. Chen and K.S. Schweizer. Suppressed Segmental Relaxation as the Origin of Strain Hardening in Polymer Glasses. *Physical Review Letters*, 102(3):038301, 2009. doi: 10.1103/PhysRevLett.102.038301.

[18] R.S. Hoy and M.O. Robbins. Strain Hardening in Polymer Glasses: Limitations of Network Models. *Physical Review Letters*, 99(11):117801, 2007. doi: 10.1103/PhysRevLett.99.117801.

[19] M. Tsige, D.L. Christian, and J.S. Mark. Role of Network Connectivity on the Mechanical Properties of Highly Cross-Linked Polymers. *Macromolecules*, 37 (22):8466–8472, 2004.

[20] L. Yang, D.J. Srolovitz, and A.F. Yee. Extended ensemble molecular dynamics

method for constant strain rate uniaxial deformation of polymer systems. *The Journal of Chemical Physics*, 107(11):4396, 1997.

[21] Y. Shaorui, C. Zhiwei, and Q. Jianmin. A coarse-grained model for epoxy molding compound. *Journal of Physical Chemistry B*, 118(6):1660–1669, 2014.

[22] M. Sharifi, C. Jang, C.F. Abrams, and G.R. Palmese. Epoxy Polymer Networks with Improved Thermal and Mechanical Properties via Controlled Dispersion of Reactive Toughening Agents. *Macromolecules*, 48(20):7495–7502, 2015.

[23] M.J. Richardson and N.G. Savill. Derivation of accurate glass transition temperatures by differential scanning calorimetry. *Polymer*, 16(10):753–757, 1975.

[24] J.I. McKechnie, R.N. Haward, D. Brown, and J.H. Clarke. Effects of chain configurational properties on the stress-strain behavior of glassy linear polymers. *Macromolecules*, 26(1):198–202, 1993.

[25] C. Kang and S. Kenneth. Stress-enhanced mobility and dynamic yielding in polymer glasses. *Europhysics Letters*, 79(2):26006, 2007.

[26] D. Kilburn, D. Bamford, G. Dlubek, J. Pionteck, and M. A. Alam. The size and number of local free volumes in polypropylenes: A positron lifetime and PVT study. *Journal of Polymer Science, Part B: Polymer Physics*, 41(23): 3089–3093, 2003.

[27] Y.C. Jean, T.C. Sandreczki, and D.P. Ames. Positronium annihilation in amine-cured epoxy polymers. *Journal of Polymer Science Part B: Polymer Physics*, 24(6):1247–1258, 1986.

[28] Y.C. Jean. Positron annihilation spectroscopy for chemical analysis: A novel probe for microstructural analysis of polymers. *Microchemical Journal*, 42(1): 72–102, 1990.

[29] S.J. Wang, C.L. Wang, and B. Wang. Microstructure and mechanical properties of polymer studied by positron annihilation. *Journal of Radioanalytical and Nuclear Chemistry*, 210(2):407–421, 1996.

[30] G.U. Losi and W.G. Knauss. Free Volume Theory and Nonlinear Thermoviscoelasticity. *Polymer Engineering and Science*, 32(8):542–557, 2004.

[31] K. Bathe. *Finite Element*. Prentice Hall, 1996. ISBN 0133014584.

[32] O.C. Zienkiewicz, R.L. Taylor, and J.Z. Zhu. *The Finite Element Method: its Basis and Fundamentals*. Butterworth-Heinemann, 2013.

[33] E.J. Barbero, P. Lonetti, and K.K. Sikkil. Finite element continuum damage modeling of plain weave reinforced composites. *Composites Part B: Engineering*, 37(2-3):137–147, 2005.

[34] P.F. Liu and J.Y. Zheng. Recent developments on damage modeling and finite element analysis for composite laminates: A review. *Materials and Design*, 31 (8):3825–3834, 2010.

[35] T. Okabe, N. Takeda, Y. Kamoshida, M. Shimizu, and W. A. Curtin. A 3D shear-lag model considering micro-damage and statistical strength prediction of unidirectional fiber-reinforced composites. *Composites Science and Technology*, 61(12):1773–1787, 2001.

[36] Y. Takahashi, Y. Kikuchi, A. Konosu, and H. Ishikawa. Development and validation of the finite element model for the human lower limb of pedestrians. *Stapp car crash journal 2000-01-SC22*, 44:335–55, 2000.

[37] Z. Xia, T. Okabe, and W.A. Curtin. Shear-lag versus finite element models for stress transfer in fiber-reinforced composites. *Composites Science and Technology*, 62(9):1141–1149, 2002.

[38] P. Zhao and S. Ji. Refinements of shear-lag model and its applications. *Tectonophysics*, 279(1-4):37–53, 1997.

[39] J. Fish, Q. Yu, and K. Shek. Computational damage mechanics for composite materials based on mathematical homogenization. *International Journal for Numerical Methods in Engineering*, 45(11):1657–1679, 1999.

[40] G.Z. Voyiadjis, P.I. Kattan, and Z.N. Taqieddin. Continuum Approach to Damage Mechanics of Composite Materials with Fabric Tensors. *International Journal of Damage Mechanics*, 16(3):301–329, 2007.

[41] S.J. Marrink, H.J. Risselada, S. Yefimov, D. Tieleman, and A.H. De Vries. The MARTINI force field: Coarse grained model for biomolecular simulations. *Journal of Physical Chemistry B*, 111(27):7812–7824, 2007.

[42] W. Shinoda, R. DeVane, and M.L. Klein. Multi-property fitting and parameterization of a coarse grained model for aqueous surfactants. *Molecular Simulation*, 33(1-2):27–36, 2007.

[43] J.C Shelley, M.Y. Shelley, R.C. Reeder, S. Bandyopadhyay, and M.L. Klein. Article A Coarse Grain Model for Phospholipid Simulations A Coarse Grain Model for Phospholipid Simulations. *Journal of Physical Chemistry B*, 105 (April):4464–4470, 2001.

[44] W. Tschöp, K. Kremer, J. Batoulis, T. Bürger, and O. Hahn. Simulation of polymer melts. I. Coarse-graining procedure for polycarbonates. *Acta Polymerica*, 49(2-3):61–74, 1998.

[45] H. Fukunaga, J. Takimoto, and M. Doi. A coarse-graining procedure for flexible polymer chains with bonded and nonbonded interactions A coarse-graining procedure for flexible polymer chains with bonded and nonbonded interactions. *Journal of Chemical Physics*, 8183(2002):8183–8190, 2014.

[46] A. Srivastava and S. Ghosh. Reduced-order molecular-dynamics model for polystyrene by equivalent-structure coarse graining. *Physical Review E - Statistical, Nonlinear, and Soft Matter Physics*, 85(2):26702, 2012.

[47] S..J. Marrink, A.H. de Vries, and A.E. Mark. Coarse Grained Model for Semiquantitative Lipid Simulations. *The Journal of Physical Chemistry B*, 108(2): 750–760, 2004.

[48] D.C. Rapaport. *The Art of Molecular Dynamics Simulation*. Cambridge University Press, 1998.

[49] D. Sholl and J.A. Steckel. *Density Functional Theory: A Practical Introduction*. Wiley, 2009.

[50] P. Hohenberg and W. Kohn. The Inhomogeneous Electron Gas. *Physical Review*, 136(3B):B864, 1964.

[51] F.E. Adams and B. James. Interatomic potentials from first-principles calculations. *Materials Research Society*, 291:31–36, 1993.

[52] L.S. Loo. Chain Mobility in the Amorphous Region of Nylon 6 Observed under Active Uniaxial Deformation. *Science*, 288(5463):116–119, 2000.

[53] S. Loo, E. Cohen, and K. Gleason. Deuterium Nuclear Magnetic Resonance of Phenol- d 5 in Nylon 6 under Active Uniaxial Deformation. *Macromolecules*, 32(13):4359–4364, 1999.

[54] J.M. Koelman and P.J. Hoogerbrugge. Dynamic Simulations of Hard-Sphere Suspensions Under Steady Shear. *Europhysics Letters*, 21(3):363–368, 1993.

[55] F. Müller-Plathe. Coarse-graining in polymer simulation: From the atomistic to the mesoscopic scale and back. *ChemPhysChem*, 3(9):754–769, 2002.

[56] C.D. Lorenz, M.J. Stevens, and R.P. Wool. Fracture behavior of triglyceride-based adhesives. *Journal of Polymer Science, Part B: Polymer Physics*, 42(18): 3333–3343, 2004.

[57] S.W. Chiu, S.A. Pandit, H.L. Scott, and E. Jakobsson. An improved united atom force field for simulation of mixed lipid bilayers. *Journal of Physical Chemistry B*, 113(9):2748–2763, 2009.

[58] M.D. Macedonia and .J. Maginn. A biased grand canonical Monte Carlo method for simulating adsorption using all-atom and branched united atom models. *Molecular Physics*, 96(9):1375–1390, 1999.

[59] W. Paul, D.Y. Yoon, and G.D. Smith. An optimized united atom model for simulations of polymethylene melts. *The Journal of Chemical Physics*, 103(4): 1702–1709, 1995.

[60] A. Liwo, M. Khalili, and H.A. Scheraga. Ab initio simulations of protein-folding pathways by molecular dynamics with the united-residue model of polypeptide chains. *Proceedings of the National Academy of Sciences of the United States of America*, 102(7):2362–7, 2005.

[61] T. Vettorel and H. Meyer. Coarse graining of short polythylene chains for studying polymer crystallization. *Journal of Chemical Theory and Computation*, 2 (3):616–629, 2006.

[62] Y. Li, S. Tang, and B.C. Abberton. A predictive multiscale computational framework for viscoelastic properties of linear polymers. *Polymer*, 53(25):5935–5952, 2012.

[63] T. Murtola, E. Falck, M. Patra, M. Karttunen, and I. Vattulainen. Coarse-grained model for phospholipid/cholesterol bilayer. *The Journal of Chemical Physics*, 121(18):9156–9165, 2004.

[64] J.Z. Zhang. *Theory and Application of Quantum Molecular Dynamics*. WORLD SCIENTIFIC, 1999. ISBN 9810233884. doi: 10.1142/3713.

[65] O. Ridge. *Nonequilibrium Molecular Dynamics of Liquid Crystals*. Springer Netherlands, Dordrecht, 1994. ISBN 978-94-010-4509-4. doi: 10.1007/978-94-011-1168-3.

[66] P. Balbuena and J.M. Seminario. *Molecular Dynamics: From Classical to Quantum Methods*. Elsevier, 1999.

[67] J.E. Jones. On the Determination of Molecular Fields. II. From the Equation of State of a Gas. *Proceedings of the Royal Society A: Mathematical, Physical and Engineering Sciences*, 106(738):463–477, 1924.

[68] C.Y. Peng, P.Y. Ayala, H.B. Schlegel, and Michael J. Frisch. Using redundant internal coordinates to optimize equilibrium geometries and transition states. *Journal of Computational Chemistry*, 17(1):49–56, 1996.

[69] R. Malek and N. Mousseau. Dynamics of lennard-jones clusters: A characterization of the activation-relaxation technique. *Physical review. E, Statistical physics, plasmas, fluids, and related interdisciplinary topics*, 62(6 Pt A):7723–8, 2000.

[70] R. Fletcher and C.M. Reeves. Function minimization by conjugate gradients. *The Computer Journal*, 7(2):149–154, 1964.

[71] M.C. Payne, M.P. Teter, D.C. Allan, T.A. Arias, and J.D. Joannopoulos. Iterative minimization techniques for ab initio total-energy calculations: Molecular dynamics and conjugate gradients. *Reviews of Modern Physics*, 64(4):1045–1097, 1992.

[72] C.J. Casewit, K.S. Colwell, and A.K. Rappe. Application of a universal force field to organic molecules. *Journal of the American Chemical Society*, 114(25): 10035–10046, 1992. doi: 10.1021/ja00051a041.

[73] A.K. Rappe, C.J. Casewit, K.S. Colwell, W.A. Goddard, and W.M. Skiff. UFF, a full periodic table force field for molecular mechanics and molecular dynamics simulations. *Journal of the American Chemical Society*, 114(25):10024–10035, 1992. doi: 10.1021/ja00051a040.

[74] M.J. Frisch and G.W. Trucks. Gaussian09 Revision E01.

[75] W. K. Hastings. Monte Carlo sampling methods using Markov chains and their applications. *Biometrika*, 57(1):97–109, 1970.

[76] W.L. Jorgensen, D.S. Maxwell, and J. Tirado-Rives. Development and testing of the OPLS all-atom force field on conformational energetics and properties of organic liquids. *Journal of the American Chemical Society*, 118(45):11225–11236, 1996.

[77] M. Schulz and H.L. Frisch. Mean field theory of interpenetrating polymer network gels. *The Journal of Chemical Physics*, 107(7):2673, 1997.

[78] B.E. Eichinger. Shape distributions of Gaussian molecules. *Macromolecules*, 18 (2):211–216, 1985.

[79] K. Cheng and W. Chiu. Monte Carlo Simulation of Polymer Network Formation with Complex Chemical Reaction Mechanism: Kinetic Approach on Curing Epoxides with Amines. *Macromolecules*, 27(12):3406–3414, 1994.

[80] D.R. Heine, G.S. Grest, C.D. Lorenz, M. Tsige, and M.J. Stevens. Atomistic simulations of end-linked poly(dimethylsiloxane) networks: Structure and relaxation. *Macromolecules*, 37(10):3857–3864, 2004.

[81] D.C. Doherty, B.N. Holmes, P. Leung, and R.B. Ross. Polymerization molecular dynamics simulations. I. Cross-linked atomistic models for poly(methacrylate) networks. *Computational and Theoretical Polymer Science*, 8(1-2):169–178, 1998.

[82] I. Yarovsky and E. Evans. Computer simulation of structure and properties of crosslinked polymers: application to epoxy resins. *Polymer*, 43(3):963–969, 2002.

[83] V. Varshney, S.S. Patnaik, A.K. Roy, and B.L. Farmer. A molecular dynamics study of epoxy-based networks: Cross-linking procedure and prediction of molecular and material properties. *Macromolecules*, 41(18):6837–6842, 2008.

[84] C. Wu and We. Xu. Atomistic simulation study of absorbed water influence on structure and properties of crosslinked epoxy resin. *Polymer*, 48(18):5440–5448, 2007.

[85] Y. Chen and W.Y. Chiu. Polymer chain buildup and network formation of imidazole-cured epoxy/phenol resins. *Macromolecules*, 33(18):6672–6684, 2000.

[86] H.B. Fan and M.F. Yuen. Material properties of the cross-linked epoxy resin compound predicted by molecular dynamics simulation. *Polymer*, 48(7):2174–2178, 2007.

[87] J. Gou, B. Minaie, B. Wang, Z. Liang, and C. Zhang. Computational and experimental study of interfacial bonding of single-walled nanotube reinforced composites. *Computational Materials Science*, 31(3-4):225–236, 2004.

[88] A. Prasad, T. Grover, and S. Basu. Coarse grained molecular dynamics simulation of cross linking of DGEBA epoxy resin and estimation of the adhesive strength. *Science And Technology*, 2(4):17–30, 2010.

[89] S. Plimpton. Fast Parallel Algorithms for Short-Range Molecular Dynamics, 1995.

[90] P.V. Komarov, C. Yu-tsung, C. Shih-ming, and P.G. Khalatur. Highly Cross-Linked Epoxy Resins : An Atomistic Molecular Dynamics Simulation Combined with a Mapping / Reverse Mapping Procedure. *Society*, 40(22):8104–8113, 2007.

[91] J. Flory. Molecular Size Distribution in Three Dimensional Polymers. I. Gelation. *Journal of the American Chemical Society*, 63(11):3083–3090, 1941.

[92] P.J. Flory. *Principles of Polymer Chemistry*. Cornell Univ. Press, 1953.

[93] J. Buchholz, W. Paul, F. Varnik, and K. Binder. Cooling rate dependence of the glass transition temperature of polymer melts: Molecular dynamics study. *The Journal of Chemical Physics*, 117(15):7364, 2002.

[94] K.S. Liao, H. Chen, S. Awad, J.P. Yuan, W.S. Hung, K.R. Lee, J.Y. Lai, C. Hu, and Y. C. Jean. Determination of free-volume properties in polymers without orthopositronium components in positron annihilation lifetime spectroscopy. *Macromolecules*, 44(17):6818–6826, 2011.

[95] Y.C. Jean and Q. Deng. Direct measurement of free-volume hole distributions in polymers by using a positronium probe. *Journal of Polymer Science, Part B: Polymer Physics*, 30(12):1359–1364, 1992.

[96] A.S. Argon. Plastic deformation in glassy polymers by atomistic and mesoscopic simulations. *Journal of Rheology*, 39(2):377, 1995.

[97] M.L. Williams, R.F. Landel, and D.J. Ferry. The Temperature Dependence of Relaxation Mechanisms in Amorphous Polymers and Other Glass-forming Liquids. *Journal American Chemical Society*, 679(14):3701–3707, 1955.

[98] D. Hofmann, L. Fritz, J. Ulbrich, C. Schepers, and M. Bhning. Detailed-atomistic molecular modeling of small molecule diffusion and solution processes in polymeric membrane materials. *Macromolecular Theory and Simulations*, 9 (6):293–327, 2000.

[99] D. Rigby and R. Roe. Molecular dynamics simulation of polymer liquid and glass. I. Glass transition. *The Journal of Chemical Physics*, 87(12):7285, 1987.

[100] D. Hofmann, M. Heuchel, Y. Yampolskii, V. Khotimskii, and V. Shantarovich. Free volume distributions in ultrahigh and lower free volume polymers: Comparison between molecular modeling and positron lifetime studies. *Macromolecules*, 35(6):2129–2140, 2002.

[101] D. Hofmann, M. Entrialgo-Castano, A. Lerbret, M. Heuchel, and Y. Yampolskii. Molecular modeling investigation of free volume distributions in stiff chain polymers with conventional and ultrahigh free volume: Comparison between molecular modeling and positron lifetime studies. *Macromolecules*, 36(22):8528–8538, 2003.

[102] C. Nagel, E. Schmidtke, K. Günther-Schade, D. Hofmann, D. Fritsch, T. Strunskus, and F. Faupel. Free volume distributions in glassy polymer membranes: comparison between molecular modeling and experiments. *Macromolecules*, 33 (6):2242–2248, 2000.

[103] M. Heuchel, D. Hofmann, and P. Pullumbi. Molecular modeling of small-molecule permeation in polyimides and its correlation to free-volume distributions. *Macromolecules*, 37(1):201–214, 2004.

[104] M. Heuchel, D. Fritsch, P.M. Budd, N.B. McKeown, and D. Hofmann. Atomistic packing model and free volume distribution of a polymer with intrinsic microporosity (PIM-1). *Journal of Membrane Science*, 318(1-2):84–99, 2008.

[105] D. Rako, S. Capponi, F. Alvarez, and J. Colmenero. The free volume of poly(vinyl methylether) as computed in a wide temperature range and at length scales up to the nanoregion. *Journal of Chemical Physics*, 134(4):044512, 2011.

[106] Y.U.S. Lipatov and V.P. Privalko. Dependence of the free volume fraction at the glass transition temperature on the molecular parameters of linear polymers. *Journal of Macromolecular Science, Part B*, 7(3):431–444, 1973. doi: 10.1080/00222347308207877.

[107] https://bitbucket.org/aaramoon/utilities.

[108] M. de Berg, O. Cheong, M. van Kreveld, and M. Overmars. *Computational Geometry: Algorithms and Applications*. Springer-Verlag Berlin Heidelberg, 2008.

[109] S. Misra and W.L. Mattice. Atomistic models of amorphous polybutadienes. 3. Static free volume. *Macromolecules*, 26(26):7274–7281, 1993. doi: 10.1021/ma00078a024.

[110] G.P. Johari and M. Goldstein. Viscous Liquids and the Glass Transition. II. Secondary Relaxations in Glasses of Rigid Molecules. *The Journal of Chemical Physics*, 53(6):2372–2388, 1970.

[111] G. Adam and J.H. Gibbs. On the Temperature Dependence of Cooperative Relaxation Properties in GlassForming Liquids. *The Journal of Chemical Physics*, 43(1):139–146, 1965.

[112] A. Patkowski, M. Paluch, and H. Kriegs. Dynamic light scattering studies of supercooled phenylphthalein–dimethylether dynamics under high pressure. *The Journal of Chemical Physics*, 117(5):2192–2198, 2002.

[113] T.G. Fox and S. Loshaek. Influence of molecular weight and degree of crosslinking on the specific volume and glass temperature of polymers. *Journal of Polymer Science*, 15(80):371–390, 1955.

[114] T.G. Fox and P. Flory. Second-order transition temperatures and related properties of polystyrene. I. Influence of molecular weight. *Journal of Applied Physics*, 21(6):581–591, 1950.

[115] T. Ogawa. Effects of molecular weight on mechanical properties of polypropylene. *Journal of Applied Polymer Science*, 44(10):1869–1871, 1992.

[116] J. Ramos, J.F. Vega, and J. Martínez-Salazar. Molecular Dynamics Simulations for the Description of Experimental Molecular Conformation, Melt Dynamics, and Phase Transitions in Polyethylene. *Macromolecules*, 48(14):5016–5027, 2015.

[117] Z. Wang, Q. Lv, S. Chen, C. Li, S.g Sun, and S. Hu. Glass transition investigations on highly crosslinked epoxy resins by molecular dynamics simulations. *Molecular Simulation*, 41(18):1515–1527, 2015.

[118] H. Nakanishi, Y.C. Jean, and D.M. Schrader. *Positron and Positronium Chemistry*. Elsevier Science Ltd (October 1988), 1988.

[119] A.E. Feinerman and Y.S. Lipatov. Free volume distribution in crosslinked polyurethanes. *Journal of Polymer Science Part B: Polymer Physics*, 38 (6):899–905, 2000. doi: 10.1002/(SICI)1099-0488(20000315)38:6¡899::AID-POLB10¿3.0.CO;2-1.

[120] R. Simha and Phillip S. W. Thermal Expansion of Amorphous Polymers at Atmospheric Pressure. II. Theoretical Considerations. *Macromolecules*, 6(6): 908–914, 1973.

[121] L.A. Pruitt. Deformation, yielding, fracture and fatigue behavior of conventional and highly cross-linked ultra high molecular weight polyethylene. *Biomaterials*, 26(8):905–915, 2005.

[122] A.S. Argon. A theory for the low-temperature plastic deformation of glassy polymers. *Philosophical Magazine*, 28(4):839–865, 1973.

[123] J.J. Kim, Y. Choi, S. Suresh, and A.S. Argon. Nanocrystallization During Nanoindentation of a Bulk Amorphous Metal Alloy at Room Temperature. *Science*, 295(5555):654–657, 2002.

[124] J. Jordan, K. Jacob, R. Tannenbaum, M.A. Sharaf, and I. Jasiuk. Experimental trends in polymer nanocomposites - A review. *Materials Science and Engineering A*, 393(1-2):1–11, 2005.

[125] Q.H. Zeng, A.B. Yu, and G.Q. Lu. Multiscale modeling and simulation of polymer nanocomposites. *Progress in Polymer Science*, 33(2):191–269, 2008.

[126] G. Vogiatzis, E. Voyiatzis, and D.N. Theodorou. Monte Carlo simulations of a coarse grained model for an athermal all-polystyrene nanocomposite system. *European Polymer Journal*, 47(4):699–712, 2011.

[127] R. Ruggerone, V. Geiser, S. Dalle Vacche, Y. Leterrier, and J.E. Månson. Immobilized polymer fraction in hyperbranched polymer/silica nanocomposite suspensions. *Macromolecules*, 43(24):10490–10497, 2010.

[128] S. Merabia, P. Sotta, and D.R. Long. A microscopic model for the reinforcement and the nonlinear behavior of filled elastomers and thermoplastic elastomers (Payne and Mullins Effects). *Macromolecules*, 41(21):8252–8266, 2008.

[129] H. Montes, F. Lequeux, and J. Berriot. Influence of the Glass Transition Tem-

perature Gradient on the Nonlinear Viscoelastic Behavior in Reinforced Elastomers. *Macromolecules*, 36(21):8107–8118, 2003.

[130] T. Ndoro, E. Voyiatzis, A. Ghanbari, D.N. Theodorou, M.C. Böhm, and F. Müller-Plathe. Interface of grafted and ungrafted silica nanoparticles with a polystyrene matrix: Atomistic molecular dynamics simulations. *Macromolecules*, 44(7):2316–2327, 2011.

[131] M. Roy, J.K. Nelson, R.K. MacCrone, L.S. Schadler, and C. Reed. Polymer nanocomposite dielectrics - The role of the interface. *IEEE Transactions on Dielectrics and Electrical Insulation*, 12(4):629–642, 2005.

[132] M.E. Mackay, T.T. Dao, A. Tuteja, D.L. Ho, B. van Horn, and H. Kim. Nanoscale effects leading to non-Einstein-like decrease in viscosity. *Nature materials*, 2(11):762–766, 2003.

[133] G.M. Odegard, T.C. Clancy, and T.S. Gates. Modeling of the mechanical properties of nanoparticle/polymer composites. *Polymer*, 46(2):553–562, 2005.

[134] A. Ghanbari, T.V. Ndoro, F. Leroy, M. Rahimi, M.C. Böhm, and F. Müller-Plathe. Interphase structure in silica-polystyrene nanocomposites: A coarse-grained molecular dynamics study. *Macromolecules*, 45(1):572–584, 2012.

[135] G. Bai and A. Suzuki. Effects of continuous water flow on the swelling properties of polyelectrolyte hydrogels. *European Physical Journal E*, 14(2):107–113, 2004.

[136] P.G. de Gennes. Conformations of Polymers Attached to an Interface. *Macromolecules*, 13(19):1069–1075, 1980.

[137] A.P. Gast and L. Leibler. Effect of polymer solutions on sterically stabilized suspensions. *The Journal of Physical Chemistry*, 89(19):3947–3949, 1985.

[138] C. Chevigny, J. Jestin, D. Gigmes, R. Schweins, E. Di-Cola, F. Dalmas, D. Bertin, and F. Boué. "Wet-To-Dry" Conformational Transition of Polymer Layers Grafted To Nanoparticles in Nanocomposite. *Macromolecules*, 43 (11):4833–4837, 2010.

[139] A.P. Gast and L. Leibler. Interactions of sterically stabilized particles suspended in a polymer solution. *Macromolecules*, 19(3):686–691, 1986.

[140] I. Borukhov and L. Leibler. Enthalpic stabilization of brush-coated particles in a polymer melt. *Macromolecules*, 35(13):5171–5182, 2002.

[141] J.B. Hooper and K.S. Schweizer. Theory of phase separation in polymer nanocomposites. *Macromolecules*, 39(15):5133–5142, 2006.

[142] M. Rahimi, I. Iriarte-Carretero, A. Ghanbari, M.C. Böhm, and F. Müller-Plathe. Mechanical behavior and interphase structure in a silicapolystyrene nanocomposite under uniaxial deformation. *Nanotechnology*, 23(30):305702, 2012.

[143] E. Riccardi, M. C. Böhm, and F. Müller-Plathe. Molecular dynamics approach to locally resolve elastic constants in nanocomposites and thin films: Mechanical description of solid-soft matter interphases via Young's modulus, Poisson's ratio and shear modulus. *European Physical Journal E*, 37(10):103, 2014.

[144] R.J. Morgan. The effect of thermal history and strain rate on the mechanical properties of diethylenetriamine cured bisphenol A diglycidyl ether epoxies. *Journal of Applied Polymer Science*, 23(9):2711–2717, 1979.

[145] A.E. Mayr, W.D. Cook, and G.H. Edward. Yielding behaviour in model epoxy thermosets I. Effect of strain rate and composition. *Polymer*, 39(16):3719–3724, 1998.

[146] R.S. Kody and J. Lesser. Deformation and yield of epoxy networks in constrained states of stress. *Journal of Materials Science*, 32:5637–5643, 1997.

[147] W.D. Cook, M. Mehrabi, and G.H. Edward. Ageing and yielding in model epoxy thermosets. *Polymer*, 40(5):1209–1218, 1999.

[148] A. Abazari, S. Safavi, G. Rezazadeh, and L. Villanueva. Modelling the size effects on the mechanical properties of micro/nano structures. *Sensors (Switzerland)*, 15(11):28543–28562, 2015.

[149] Abaqus 6.13 analysis users manual, SIMULIA, Providence, IR, 2013.

Vita

Amin Aramoon was born in Tehran, Iran in 1987. In 2004, he graduated high school from high school in Hatef, Tehran. He started his undergraduate studies in the Sharif university of technology. He graduated in 2009 with first class honors from the department of Civil Engineering. He started his Master degree studies immediately after graduation and obtained his M.Sc. in Civil Engineering in 2011. Between Jun 2011 and February 2012, he held the position of a research scientist in Giti Pasanad Corp where he developed mathematical libraries to be used in engineering analysis software. He also had a secondary appointment as a teaching assistant in the department of Civil engineering in Sharif university between Sep 2008 and Jun 2012. In Sept 2012, he joined the Computational and Experimental Materials Engineering Laboratory at Johns Hopkins University as a research assistant working on the characterization of properties of epoxy systems from coarse-grained MD simulations.

List of Publications

- Aramoon et. al. "Coarse-Grained Molecular Dynamics Study of the Curing and Properties of Highly Cross-Linked Epoxy Polymers", J. Phys. Chem. B. 2016, 120 (35), pp 94959505

- Amin Aramoon, Timothy D. Breitzman, Christopher Woodward, and Jaafar A. El-Awady, "Correlating Free-Volume Hole Distribution to the Glass Transition Temperature of Epoxy Polymers", Submitted

- Amin Aramoon, Timothy D. Breitzman, Christopher Woodward, and Jaafar A. El-Awady "Correlating Free-Volume Hole Distribution of Matrix to the Strength, and Damage Evolution of PMCs", In preparation